NOTE TO USERS

PERFORMANCE ASSESSMENT OF ISLANDING DETECTION METHODS USING THE CONCEPT OF NON-DETECTION ZONES

Sun Huili

A Thesis

in

The Department

of

Electrical and Computer Engineering

Presented in Partial Fulfillment of the Requirements

for the Degree of Master of Applied Science at

Concordia University

Montréal, Québec, Canada

February 2005

Your file Votre référence
ISBN: 0-494-04401-2
Our file Notre référence
ISBN: 0-494-04401-2

ABSTRACT

PERFOMNCE ASSESSMENT OF ISLANDING DECTECTION METHODS USING A NEW LOAD PARAMETER SPACE

Sun Huili

Concerns for the rising cost of electricity, environmental impact, and the difficulty in obtaining new right-of-ways results in the use of smaller environmentally-friendly power sources such as photovoltaic (PV), wind-driven or gas-fired micro-turbines located closer to the end consumers, which are connected directly to the distribution system in what is commonly referred to as distributed generation (DG). The protection schemes of the distribution systems were designed under the assumption that power flows from the substations to the end users. If a fault takes place and a breaker opens all circuits downstream would be de-energized. However this is not the case when DG is used. Under fault condition, an island condition with power generation and consumption threatens both equipment and personnel safety. Thus, islanding detection methods (IDMs) must be developed and tested. A number of IDMs has been developed to prevent this situation.

The goal of this thesis is to investigate a means for comparing the effectiveness of active type IDMs used in an inverter based DG. Unlike standard passive IDMs, the use of non-detection zones (NDZ) in a power imbalance plane is not adequate. This thesis proposes a new load parameter space based on the load quality factor Q_f and resonant frequency f_0. Equations that describe the NDZs of three of the most used active IDMS, namely active frequency drift (AFD), slip-mode phase shift (SMS) and Sandia frequency shift (SFS) have been derived. Simulation and experimental results are presented to corroborate the theoretical analysis.

ACKNOWLEDGMENTS

The author would like to express her sincere gratitude to her supervisor, Dr. Luiz A. C. Lopes for his invaluable guidance, advice, friendship and financial support throughout the course of this study.

Special thanks to Mr. Joseph Woods for his technical support, friendship, kindness, and unconditional help.

The author would also like to thank her colleagues in the P. D. Ziogas Power Electronics Laboratory. Smart suggestions from and helpful discussions with Zhixiang Luo, Xuejun Liu and Su Chen are unforgettable.

Last but not least, the author is very grateful towards her family whose constant support made it possible to finish the project.

To my parents

LIST OF CONTENT

LIST OF FIGURE

LIST OF TABLE

LIST OF ACRONYMS

A/D	Analog to Digital
AFD	Active Frequency Drift
AFDPF	Active Frequency Drift with Positive Feedback
D/A	Digital to Analog
DER	Distributed Energy Resource
DG	Distributed Generation
DSP	Digital Signal Processor
I/O	Input and Output
IDM	Islanding Detection Method
MPPT	Maximum Power Point Tracking
NDZ	Non Detection Zone
PC	Power circuit
PCC	Point of Common Coupling
PPC	PowerPC Processor
PV	Photovoltaic
RMS	Root-Mean-Square value
SFS	Sandia Frequency Shift
SMS	Slip-Mode phase Shift
THD	Total Harmonic Distortion
UFP/OFP	Under Frequency Protection and Over Frequency Protection
UVP/OVP	Under Voltage Protection and Over Voltage Protection

LIST OF PRINCIPAL SYMBOLS

ω	Angular frequency
ω_0	Load resonant angular frequency
ω_g	Angular grid frequency
ω_i	Current angular frequency
ϕ_{load}	Load phase angle
ΔP	Real power mismatch
ΔQ	Reactive power mismatch
C	Load Capacitance
cf	Chopping factor
cf_0	Initial value of chopping factor
C_{norm}	Capacitance that normalized with C_{res}
C_{res}	Capacitance that resonates with load inductance
f	Frequency
f_0	Load resonant frequency
f_{0cal}	Calculated result of load resonant frequency
f_{0exp}	Experimental result of load resonant frequency
f_{0max}	Maximum value of load resonant frequency that will result in islanding operation
f_{0max_cal}	Calculation result of f_{0max}
f_{0max_sim}	Simulation result of f_{0max}
f_{0min}	Minimum value of load resonant frequency that will result in islanding operation

$f_{0\min\_cal}$	Calculation result of $f_{0\min}$
$f_{0\min\_sim}$	Simulation result of $f_{0\min}$
f_{0sim}	Simulated result of load resonant frequency
f_g	Gird frequency
f_i	Current frequency
f_m	Frequency at which θ_m occurs for SMS
f_{PCC}	PCC voltage frequency
f_v	Voltage frequency
h	Bandwidth of hysteresis control
I_{ac}	Grid ac current
i_{ac}	Instantaneous grid ac current
i_{load}	Instantaneous load current
I_{load}	Load current
i_{PV}	Instantaneous PV inverter output current
I_{PV}	PV inverter output current
$I_{PV\max}$	Maximum value of PV inverter output current
i_{PVref}	Instantaneous PV inverter reference current
k_{sfs}	Accelerating gain for SFS
L	Load inductance
L_{line}	Line equivalent inductance
P_{load}	Load real power
P_{PV}	PV inverter output real power
Q_f	Quality factor

Q_{fcal}	Calculated quality factor
Q_{load}	Load reactive power
Q_{PV}	PV inverter output reactive power
R	Load resistance
S	Switching state
t	Time
T_s	Simulation sampling time
T_i	Period of sinusoidal part of the current
T_{PCC}	Period of PCC voltage
t_z	Dead time of PV inverter current
V_{dc}	DC side voltage of simulation
V_g	Grid voltage
v_{PCC}	Instantaneous PCC voltage
V_{PCC}	PCC voltage
δf	Frequency drift
θ_{AFD}	Equivalent phase angle of current and voltage of inverter with AFD
θ_{inv}	Equivalent phase angle of inverter current and voltage
θ_{load}	Phase angle of load current and voltage ($\theta_{load} = -\phi_{load}$)
θ_m	Maximum phase shift of SMS (°)
θ_{SFS}	Equivalent phase angle of current and voltage of inverter with SFS
θ_{SMS}	Phase angle of current and voltage of inverter with SMS

CHAPTER 1
INTRODUCTION

1.1 INTRODUCTION

Renewable energy resources will be an increasingly important part of the power generation mixes in the new millennium. Besides assisting in the reduction of the emission of greenhouse gases, they add the much-needed flexibility to the energy resource mix by decreasing the dependence on fossil fuels. Photovoltaic (PV) electricity, although currently costing 3-5 times the price of fossil fuel-based electricity, is particularly attractive for remote areas not served by the power grid. Still, due to its modular characteristics and because it can be located closer to the user and is easier to install than central power plants and transmission networks, PV has great potential as a distributed energy resource (DER) to the utilities [1].

A number of issues need to be resolved before DER technology can reach its full potential [30-33]. Four of these are: the development of reliable and efficient power electronic interfaces, the protection of the network with power sources connected at the distribution level, the interaction between neighboring DER facilities and the application of decentralized control techniques for the distributed resources. This Thesis deals with protection aspects of DER, in particular with the study of islanding detection methods.

1.2 ISSUE OF ISLANDING DETECTION

According to the IEEE Std. 929-2000 [2], islanding is defined as "a condition in which a portion of the utility system that contains both load and distributed resources

remains energized while isolated from the remainder on the utility system". Islanding can cause both operational and maintenance problems. Operational problems include a lack of synchronism between the grid and the PV system island which then causes higher than normal voltages to appear across the open isolation device. Maintenance problems can occur if support personnel have to manually isolate all PV system connected to the section requiring work in order to bring the voltage on that section down to a safe level. The maximum time interval that a PV system-supported island can be tolerated before operational or maintenance problems arise will depend on the grid and the PV system [3]. Thus, islanding should be prevented when using photovoltaic or any other distributed energy system [30-33].

The techniques for islanding detection may be classified as remote and local [4]. Most remote techniques are based on communication between the utility and the PV inverter [34-35]. Local techniques are based on the information and data available at the PV inverter side. Remote techniques promise to be extremely effective in islanding detection but they are relatively expensive to implement in small PV systems. Local techniques are usually easy to implement and use sensors and components which are already available in the PV system so there are no additional costs.

Local techniques can be further divided into passive and active methods. Passive methods rely on the detection of an abnormality in the voltage at the point of common coupling (PCC) between the PV inverter and the utility [5, 23-29]. Active methods use a variety of methods in an attempt to cause an abnormal condition in the PCC voltage magnitude and frequency thus allowing the detection of an islanding condition [5-11], [17-22].

Most of the recent active islanding detection methods (IDMs) proceed by initiating a variation in the frequency of the PCC voltage. These include, active frequency drift (AFD) [1, 6], slip mode phase shift (SMS) [5, 7], Sandia frequency shift (SFS) [8-9], and automatic phase shift (APS) [10] algorithms, and method by injecting asymmetric PV inverter current [11].

This chapter is organized in six sections. In Sections 1.3-1.6, the passive islanding detection method based on under/over voltage relaying and under/over voltage frequency protection (UVP/OVP & UFP/OFP) devices [5] and three active islanding detection methods including AFD, SMS and SFS are discussed. The thesis outline is stated in Section 1.7.

1.3 PASSIVE ISLANDING DETECTION METHOD

Passive techniques rely on the detection of an abnormality in the voltage at the point of common coupling (PCC) between the PV inverter and the utility. Traditional under/over voltage relaying and under/over voltage frequency protection (UVP/OVP & UFP/OFP) are commonly used. The voltage and frequency protection devices are used to avoid damage to the PV inverter and the utility system as well as to ensure the safety of the utility maintenance personnel and the general public. PV system should sense utility conditions and cease to energize the utility line when the sensed voltage or frequency lies outside a desired threshold, a situation that usually takes place under islanding conditions. However, a problem that occurs in this passive islanding detection method is the proper selection of the tripping threshold.

In reality, the magnitude and the frequency during normal conditions can be expected to deviate slightly from a nominal value. Therefore, the thresholds for the over/under

voltage/frequency protection devices cannot be set arbitrarily to low or else the PV inverter will be subject to nuisance trips. The UVP/OVP and UFP/OFP trip threshold are usually set according to the IEEE Std. 929-2000 shown in Table 1 [12]. The length of the allowed time delay is set to ride through short-term disturbances avoiding excessive nuisance tripping.

Table 1-Response to abnormal voltages and frequencies [12]

Voltage (at PCC) (V)	Voltage (at PCC) of the nominal value	Frequency (Hz)	Maximum Trip Time
$V < 60$	($V < 50\%$)	f_{nom}	6 cycles
$60 \leq V < 106$	($50\% \leq V < 88\%$)	f_{nom}	120 cycles
$106 \leq V \leq 132$	($88\% \leq V \leq 110\%$)	f_{nom}	Normal Operation
$132 < V < 165$	($110\% < V < 137\%$)	f_{nom}	120 cycles
$165 \leq V$	($137\% \leq V$)	f_{nom}	2 cycles
V_{nom}		$f < 59.3$	6 cycles
V_{nom}		$59.3 \leq f \leq 60.5$	Normal Operation
V_{nom}		$f > 60.5$	6 cycles

The circuit recommended in the IEEE Std. 929-2000 for assessing the islanding detection features of a given inverter is shown in Fig. 1-1 [5]. Node **a** is at the PCC, between the utility, the PV inverter and the local load. When the grid is connected, the inverter supplies active and reactive power, $P_{PV} + jQ_{PV}$, and the local load consumes active and reactive power, $P_{load} + jQ_{load}$. The utility grid supplies or absorbs the deficit or surplus of active power $\Delta P = P_{load} - P_{PV}$ and the reactive power $\Delta Q = Q_{load} - Q_{PV}$ of the local inverter-load set. The utility grid also provides a reference ac-bus where voltage and frequency are considered to be constant.

The behaviour of the system after utility disconnection depends on the real and reactive mismatch between the PV inverter and local load prior to utility disconnection. If there are real and reactive power mismatches, the magnitude and frequency of the voltage at node "**a**" (PCC) will vary until the power supplied by PV system equals to the power

consumed by the local load. It will be shown in Chapter 2 that the deviation of the magnitude and frequency of the voltage at the island depends on the magnitude of the active and reactive power mismatches respectively. Small power mismatches between the inverter and the local load would result in small variations in the magnitude and frequency of the voltage at the PCC. In this case, the PCC would not reach the set points of the UFP/OFP and UVP/OVP devices, and an islanding condition would occur. A quantitative analysis of this problem is presented in Chapter 2.

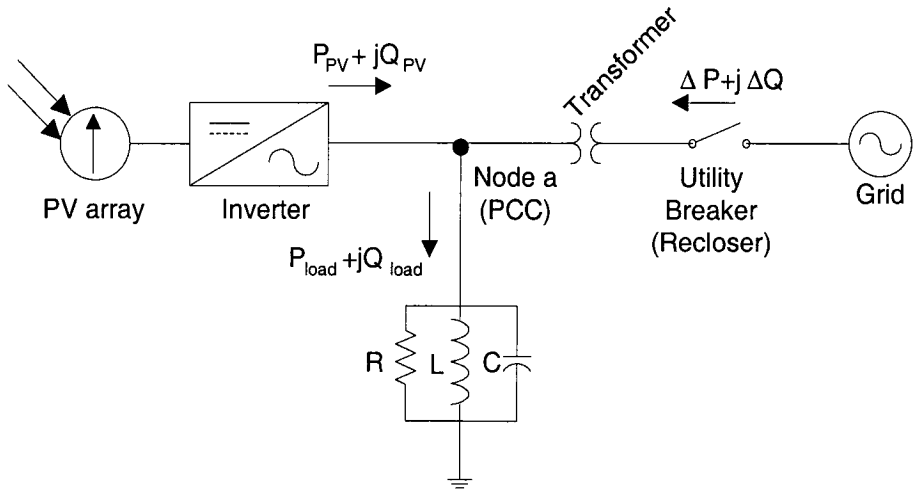

Fig. 1-1 The circuit for assessing anti-islanding features of grid-connected inverters [5].

Strengths and Weaknesses

The grid interface distributed generation system, including the PV system, is required to install the OVP/UVP and OFP/UFP for protecting loads and equipments other than islanding prevention. Also, active islanding detection methods, including AFD, SMS and SFS, rely on the OFP/UFP or OVP/UVP devices to actually deactivate the inverter. Hence, UVP/OVP & UFP/OFP does not need the extra cost for the PV system. However, the biggest problem with this method is that its effectiveness to detect islanding is low compared to AFD, SMS and SFS, shown in Chapter 2.

1.4 ACTIVE FREQUENCY DRIFT (AFD) IDM

In the active frequency drift (AFD) IDM, the waveform of the inverter current is slightly distorted as shown in Fig. 1-2 for a drift-up operation. AFD can be implemented either by including a constant zero current segment $t_z < 833\mu s$ [6], shown in Section 1.6, or by forcing the current frequency to be higher than the voltage frequency in the previous cycle by a frequency drift, $\delta f < 1.5\ Hz$ ($f_{ik} = f_{vk-1} + \delta f$). The values of the zero current segment t_z or the frequency δf are limited to make the current total harmonic distortion, $THD_i < 5\%$. When the grid is present, it maintains the PCC voltage frequency. However, when the PV system is disconnected from the grid, the frequency of the voltage at the PCC tends to drift upward, reaching values superior to the resonant frequency f_0 of the parallel resistive-inductive-capacitive (RLC) load. This increases the odds of tripping the OFP for net inductive loads at rated grid frequency. In both cases, the fundamental component of the current leads the voltage by a small angle θ_{AFD}.

The waveform of the distorted current that implements upward active frequency drift is shown in the Fig. 1-2. Fig. 1-2 shows the PCC voltage, the inverter output current waveform, and the fundamental component of the inverter current. The control equation is

$$\begin{aligned} i_{PV} &= I\sin\left(2\pi f_i t\right) \\ &= I\sin[2\pi(f+\delta f)]t, \end{aligned} \tag{1-1}$$

where $f = f_v$ is the frequency of the PCC voltage in the previous cycle.

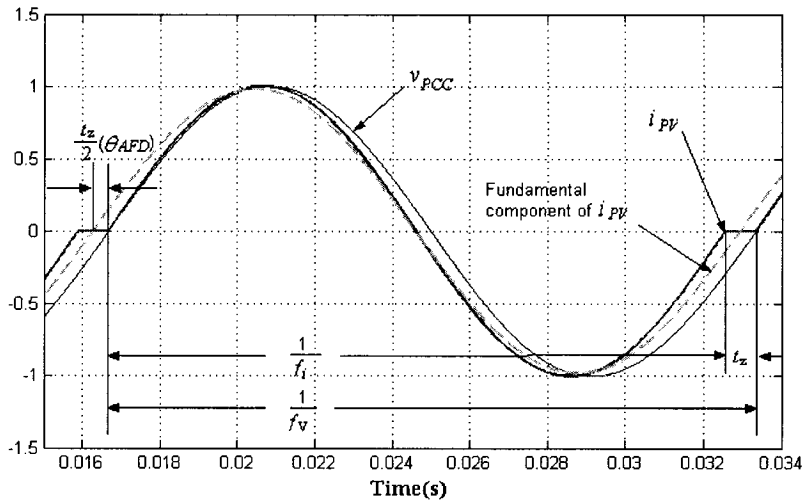

Fig. 1-2 Current and voltage waveforms of upward AFD IDM.

From Fig. 1-2, one can see that although the PV inverter output current is in phase with the PCC voltage, the current waveform is neither odd nor even. In order to simplify the calculation of the phase angle between of the fundamental components of the voltage and the current, the start of the fundamental current have been moved by $-t_z/2$. Thus, the fundamental component of the inverter output current i_{pv} leads the PCC voltage by an angle proportional to $-t_z/2$. This angle can be calculated by

$$\frac{t_z/2}{T_v} = \frac{\theta_{AFD}}{2\pi}, \tag{1-2}$$

where $t_z = \frac{1}{f_v} - \frac{1}{f_i} = \frac{1}{f} - \frac{1}{f+\delta f}$ and is commonly called dead time, T_v is the time period of the voltage of previous cycle.

Thus, the phase angle between the inverter fundamental current and the PCC voltage is given by

$$\begin{aligned}\theta_{AFD} &= \pi f t_z \\ &= \pi f\left(\frac{1}{f}-\frac{1}{f+\delta f}\right) \\ &= \frac{\pi \delta f}{f+\delta f}.\end{aligned} \tag{1-3}$$

This phase angle plays an important role in mapping the non detection zone (NDZ), which will be discussed in Chapter 2.

In principle, AFD IDM can be implemented with either speed-up or speed-down characteristics. Their effectiveness however depends significantly on the reactive type of the load. As an example an analysis is given for a net capacitive parallel *RLC* load at line frequency f_g, i.e. $f_0 < f_g$, being fed by an inverter with AFD operating in the frequency speed-up mode. Prior to the grid disconnection, the load voltage or the PCC voltage, is fixed by the grid voltage, and the inverter current is forced to be in phase with the PCC voltage. The preset speed-up rate only causes the current distortion. After the grid is disconnected, the load voltage loses its reference, and is no longer fixed by the grid. The preset speed-up rate would increase the frequency of the next cycle inverter current and the frequency of the load voltage will also increase with the same rate if the load is a pure resistance. However, since the load is capacitive, the voltage waveform will lag the inverter current and the effective speed-up rate will be less than the set value. Thus, the resulting speed-up increments are less than the pre-defined value and get increasingly smaller as the frequency increases. They may reach zero before the trip limits are reached, and islanding will occur. However, for net inductive loads, the effective frequency will be increased, aiding the speed-up process and improving islanding protection. Since most loads are inductive, speed-up is the preferred operating mode for AFD IDM.

Strengths and Weaknesses

The AFD is easily implemented in a PV inverter with a microprocessor-based controller. However, AFD with large frequency drift δf degrades the inverter output power quality to a small degree by injecting reactive power and current distortion, resulting in lower PV system power factor than unity. Besides, AFD with a small frequency drift δf is not particularly effective in islanding prevention. AFD does not offer much improvement when compared to OFP/UFP. A detailed discussion will be presented in Chapter 2.

1.5 SLIP MODE PHASE SHIFT (SMS) IDM

In the slip-mode phase shift (SMS) method, the phase angle of the current is controlled as a function of the deviation of the PCC voltage frequency of the last cycle from the nominal operating frequency of the utility. A phase advance follows an increase in frequency and a phase delay is created when there is a reduction in frequency.

The reference of the inverter current is,

$$i_{PV} = I\sin(2\pi f t + \theta_{SMS}). \tag{1-4}$$

The phase shift is set to be a sinusoidal function of the deviation of the frequency from the grid frequency f_g, then

$$\theta_{SMS} = \frac{2\pi}{360}\theta_m \sin\left(\frac{\pi}{2}\frac{f - f_g}{f_m - f_g}\right), \tag{1-5}$$

where f_m is the frequency at which the maximum phase shift θ_m occurs, and θ_m is the maximum phase shift in degrees $(^\circ)$. As in AFD, this phase angle plays an important role in mapping the NDZ, which will be discussed in Chapter 2.

When the utility is connected, it provides a solid phase and frequency, which are considered to be a constant voltage waveform reference at the PCC. However, for an

islanded system, the frequency at the PCC varies as the result of the current injected by the inverter, and will reach a value in the steady-state that can be calculated as a function of the load and the inverter's SMS characteristics. This steady-state frequency can be calculated as the frequency at which the angle of the inverter and the load present the same value. This frequency can also be identified graphically as the point at which the curve of the load angle θ_{load} vs. frequency, intersect the curve of the angle of the SMS θ_{SMS} vs. frequency according to Equation (1-5), shown in Fig. 1-3. This curve will be discussed in detail in Chapter 2. Fig. 1-3 shows the SMS frequency response and the load phase response as the frequency changes. The figure shows the phase response of two loads with the same resonant frequency, where $f_0 = 60Hz$ and the quality factors are $Q_f = 5$ and $Q_f = 1.5$. The intersections of the SMS curve and the load phase response are indicated as point **A**, **B** and **C**.

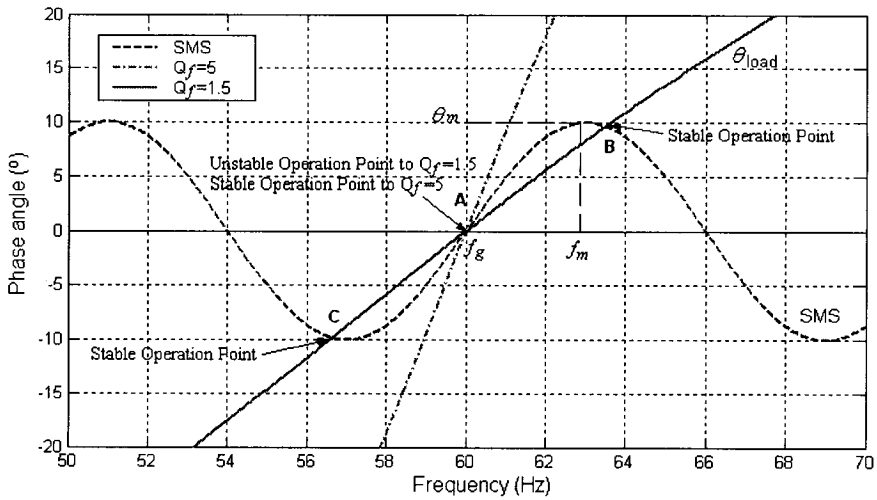

Fig. 1-3 SMS phase response curve and parallel *RLC* load phase response curve.

However, the intersection of the load line and the inverter phase response curve can be either a stable or an unstable operation point. Operation points where $\frac{d\theta_{SMS}}{df} > \frac{d\theta_{load}}{df}$

are unstable, at point **A** with a load quality factor $Q_f = 1.5$, while operation points where $\frac{d\theta_{SMS}}{df} < \frac{d\theta_{load}}{df}$ are stable, at point **A** when the load quality factor $Q_f = 5$. Point **B** and **C** are stable with respect to the load $Q_f = 1.5$. The stable operation point indicates the steady-state frequency of the islanded system. The parameters of the SMS IDM must be chosen in such a way that there will be no stable operation points inside the allowed range of the grid frequency between the settings of the UFP and OFP devices.

Strengths and Weaknesses

SMS is also easy to implement, because it is only a slight modification of an existing component. Also, it is very efficient in detecting islanding, compared to other active methods (detailed analysis is shown in Chapter 2). Moreover, it provides a good compromise between islanding detection effectiveness, output power quality, and impact on the transient response of the overall power system [5]. Like other active islanding detection methods, although to a small degree, SMS degrades the power quality of the PV system by injecting reactive power when the grid frequency is away from the nominal value but within the normal operation range, resulting in lower PV system power factor than unity.

1.6 SANDIA FREQUENCY SHIFT (SFS) IDM

Sandia frequency shift (SFS), also called active frequency drift with positive feedback (AFDPF), is an extension of the active frequency drift method, which utilizes the PCC voltage frequency as positive feedback to prevent islanding. When connected to the utility grid, the stability of the grid prevents any change although the PV inverter control tries to vary the frequency. When the utility is disconnected, the frequency error increases

and the frequency of PCC changes. The SFS accelerates the frequency error when the frequency deviates from nominal value and tries to force the frequency beyond the frequency limits.

SFS is a method to improve the weakness of AFD. The widely used scheme is the improvement of AFD with zero current segments, mentioned in Section 1.4 and shown in Fig. 1-4. The bold curve is the example of the PV system inverter with AFD along with an undistorted sinusoidal waveform shown for comparison. During the first half cycle, the PV system output current is a sinusoidal waveform with a higher frequency than the PCC voltage frequency. When the PV inverter output current reaches zero, it remains at zero for time t_z before the beginning of the second half cycle. The higher frequency also applies to the second half current cycle. The dead time of the second cycle is not fixed by the PV inverter.

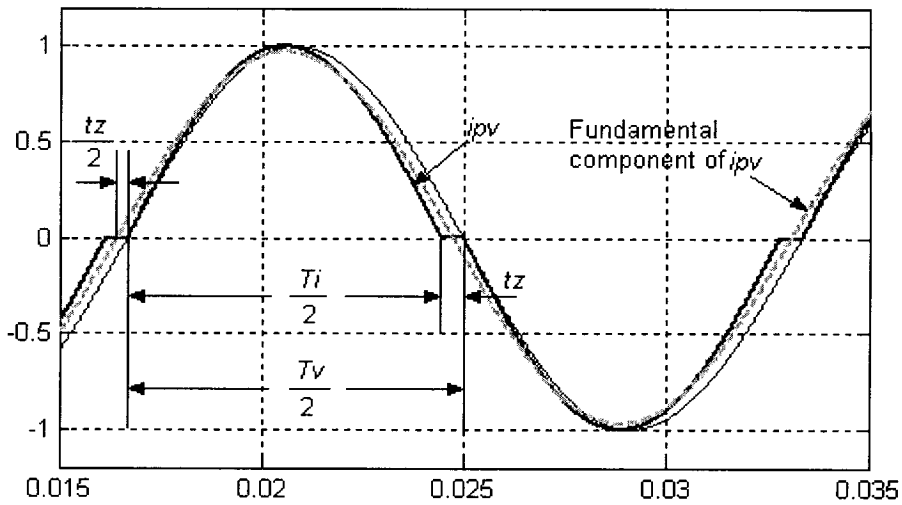

Fig. 1-4 AFD method with zero current segment [6].

A positive feedback is used to increase the chopping factor, cf, which is mathematically defined as the ratio of the zero time t_z to half of the period of the PCC voltage waveform, $T_v/2$. Thus,

$$cf = \frac{2t_z}{T_v}, \tag{1-6}$$

with increasing deviation of the frequency away from nominal value. The increasing error is usually selected to be a linear function of the frequency of PCC voltage,

$$\begin{aligned} cf &= cf_0 + F(\Delta f) \\ &= cf_0 + k_{sfs}(f - f_g), \end{aligned} \tag{1-7}$$

where cf_0 is the chopping factor when there is no frequency error, and k_{sfs} is an accelerating gain. The SFS waveform has neither odd or even symmetry, therefore, there will be a phase shift in the fundamental component of this waveform equal to $0.5\omega t_z$. If the zero current segment is small, the higher harmonic components of the current are also small, the SFS current can be approximated by its phase shifted fundamental component. Thus, the angle of the fundamental component of the inverter current varies with the frequency of the PCC and the chopping factor cf,

$$\begin{aligned} \theta_{SFS}(f) &= \frac{\omega t_z}{2} \\ &= \pi f t_z \\ &= \frac{\pi cf(f)}{2}. \end{aligned} \tag{1-8}$$

Strengths and Weaknesses

The SFS IDM, like AFD and SMS, is easy to implement, and also appears to provide a good compromise between islanding detection effectiveness, output power quality, and impact on the transient response [5]. SFS reduces output power quality of the PV inverter by injecting reactive power and current distortion, resulting in lower PV system power factor than unity, when it is connected to the grid because the positive feedback amplifies changes occurred on the grid.

1.7 THESIS SCOPE AND CONTRIBUTIONS

All the above active islanding detection methods claimed to have better performance that the passive method [5-11]. Thus, it is necessary to define performance indexes to evaluate the active methods. Non-detection zone (NDZ) is one of the most important indexes to assess the performance of the active methods. The NDZ can be mapped in different spaces. There are two spaces reported in the previous literatures, active power mismatch ΔP vs. reactive power ΔQ space and normalized capacitance C_{norm} vs. inductance L load parameter space [6, 8, 14]. These two spaces both have disadvantage to map the NDZ, detailed in Chapter 2. The goal of this thesis is to investigate a better means for comparing the effectiveness of active type IDMs used in an inverter based DG. The major contributions of this thesis are:

(1) Analyzed the effectiveness of passive islanding detection methods in the ΔP vs. ΔQ space separately for the inverter under different control scheme.

(2) Proposed a new load parameter space (quality factor Q_f vs. resonant frequency f_0) for representing non detection zones of active frequency drifting islanding detection methods.

(3) A laboratory prototype was built and experimental results verified the theoretical analysis and computer simulation.

This Thesis derived equations that represent the non-detection zones (NDZ) in ΔP vs. ΔQ power mismatch space of unity power factor current controlled inverters with constant current and constant power, and identified that the NDZ is smaller for the inverter with constant current control. Unlike the C_{norm} vs. L load parameter space, the proposed Q_f vs. f_0 load parameter space allows the easy assessment of the IDMs

for different values of load resistance with a single curve. Besides, it clearly shows how the size and shape of the NDZ vary for each active islanding method when the control parameters of the IDMs vary. A prototype of the grid connected inverter with all the control blocks has been implemented with a digital signal processing (DSP). A number of tests that verified the theoretical analysis and the computer simulation of the NDZ mapped in the proposed space have been presented.

1.8 THESIS OUTLINE

The contents of this thesis are organized in 5 chapters. The first chapter introduces the topic of anti-islanding and describes the common used anti-islanding methods, including passive and active methods. Chapter 2 focuses on the analysis of methods required to assess the effectiveness of passive and active islanding detection methods (IDMs) by the use non detection zones defined in three different spaces, including the proposed Q_f vs. f_0 space. The validation of the theoretical analysis and equations that describe the NDZ of three common active IDMs in the proposed Q_f vs. f_0 space with simulation and experiment is presented separately in Chapter 3 and Chapter 4. Chapter 5 summarizes the work carried out in this thesis and conclusions are made. Suggestions for future work on this topic are presented.

CHAPTER 2

ASSESSMENT OF ISLANDING DETECTION METHODS USING THE CONCEPT OF NON-DETECTION ZONES

2.1 INTRODUCTION

Non detection zone (NDZ) is one of the most important indexes to assess the performance of islanding detection methods (IDMs). This is defined as the range of local loads (that is, loads inside the potential island) for which the islanding detection methods (IDMs) under consideration can be made to fail to detect islanding. The effectiveness of the islanding detection methods listed in Chapter 1 is analyzed in this chapter using the NDZ criteria.

Islanding detection methods (IDMs) are usually tested with the circuit shown in Fig. 1.1 [5]. An inverter is connected at the point of common coupling (PCC) to the utility grid, and a local load, represented by a parallel *RLC* circuit. The inverter is assumed to operate in the current control mode at unity power factor with either constant power or constant current control. The utility grid provides a reference ac bus where voltage and frequency are considered to be constant. It supplies all the reactive power demanded by the load and supplies or absorbs the deficit or surplus of active power of the inverter.

Upon grid disconnection (the utility breaker opens), if there are active power imbalance ΔP and reactive power imbalance ΔQ in the islanded system, the voltage magnitude and frequency at the PCC drift to a point where the active and reactive power of the local load match those of the inverter. For large enough power imbalances, either the under/over frequency protection (UFP/OFP) or the under/over voltage protection

(UVP/OVP) devices, frequently employed in grid-connected inverters, trip, preventing the inverter from operating under islanding conditions. Therefore, by using the load power characteristics, the active power of the inverter and the trip points of the UFP/OFP and UVP/OVP devices, one can identify a non-detection zone (NDZ) in a power mismatch space (ΔP vs. ΔQ) as shown in Fig. 2-1 [5, 36-37].

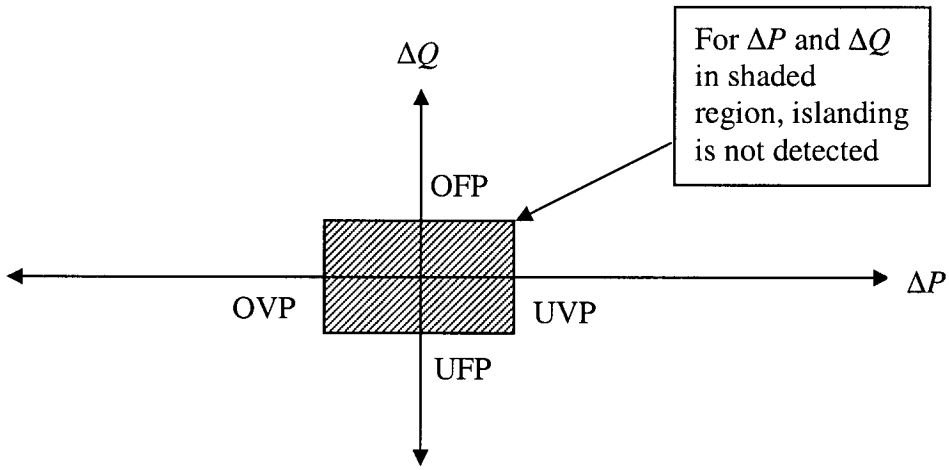

Fig. 2-1 Mapping of the NDZ in ΔP vs. ΔQ space for UVP/OVP & UFP/OFP [5].

There one clearly sees that passive islanding detection fails for small power imbalances, i.e. when the power of the local load closely matches the inverter's output power. Reducing the NDZ by reducing the normal operating range of the UFP/OFP and UVP/OVP devices is not an option since it leads to nuisance trips.

A number of active methods discussed in Chapter 1 have shown to provide superior performance [4-11]. However, the NDZs criteria in the ΔP vs. ΔQ power mismatch space are not useful in comparing their effectiveness. A load parameter space based on the actual values of the *RLC* elements of the local load has been proposed in [8] where the NDZ is represented in a normalized capacitor C_{norm} vs. inductor L load parameter space. Its main disadvantage is that one needs to plot one curve for each value of R

considered. This chapter proposes an alternative space based on the quality factor Q_f and resonant frequency f_0 of the *RLC* load. Using this space, it is easy to see the impact of the variation of the load resistor R on the shape and size of a single curve that represents the NDZ of the active IDMs.

This chapter is organized in 6 sections. Section 2.2 presents the relevant equations of parallel *RLC* loads that will be used throughout the thesis. Section 2.3 derives the equations that describe the accurate NDZ in the ΔP vs. ΔQ power mismatch space for the passive method when the inverter operates with constant current and constant power. Section 2.4 discusses the principles behind the normalized capacitance C_{norm} vs. inductance L load parameter space. Section 2.5 presents the equations that represent the NDZs in the proposed quality factor Q_f vs. resonant frequency f_0 space for the IDMs discussed in Chapter 1 as a function of the settable parameters of each of them. Conclusions about the IDMs and their NDZs in different spaces are presented in Section 2.6.

2.2 LOCAL LOAD EQUIVALENT MODEL

For the evaluation of the performance of IDMs, the local load (the load inside the potential island) is usually modeled as a parallel *RLC* circuit. This is done because for most IDMs it is some type of *RLC* load that causes the most difficulty in detection. In general, nonlinear loads such as harmonic-producing loads or constant-power loads do not present as much difficulty in islanding prevention [5].

The following sections derive expressions that represent how the phase angle and the magnitude of the load impedance vary with frequency. These relations are also shown as plots that can be used for better understanding the operating principles of the IDMs.

2.2.1 Quality Factor Q_f

According to IEEE Std. 929-2000, if the real-generation-to-load match is within 50% and the islanded-load power factor is >0.95, then a nonislanding inverter will cease to energize the utility line within 2s whenever the connected line has a quality factor of 2.5 or less.

The definition of the quality factor according to the IEEE Std. 929-2000 is: Two pi times the ratio of the maximum stored energy to the energy dissipated per cycle at a given frequency.

$$Q_f = 2\pi \frac{\max imum\ energy\ stored}{total\ energy\ lost\ in\ a\ period} \tag{2-1}$$

Values of Q_f from 0 to 2.5 are associated with uncorrected utility lines, modeled by *RL* loads with power factors that vary from unity to 0.37, respectively. Recall that as the power factor decreases, Q_f increases. Therefore, loads with Q_f from 0 to 2.5 represent all reasonable distribution line and local load configurations [2].

2.2.2 PARALLEL *RLC* CIRCUIT

As previously mentioned, a parallel *RLC* load as shown in Fig. 2-2 is commonly used as the equivalent practical local load for the performance assessment of IDMs.

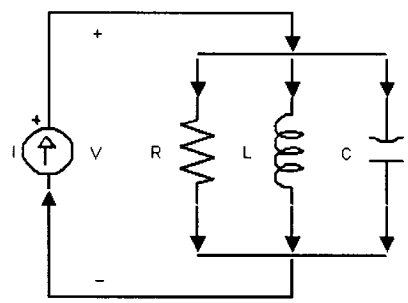

Fig. 2-2 Current source and parallel *RLC* load.

Suppose the current source is given by

$$i_s(t) = I_m \cos \omega_0 t\,, \tag{2-2}$$

where $\omega_0 = \dfrac{1}{\sqrt{LC}}$ is the angular resonant frequency of the load. Then the *RLC* load operates at the resonance. The quality factor of the *RLC* circuit is calculated as

$$Q_f = \frac{2\pi \left| P_{QC}(t) + P_{QL}(t) \right|_{\max}}{P_R T}, \tag{2-3}$$

where P_R is the active power of the load, and P_{QL} is the energy stored in the inductor, and P_{QC} is the energy stored in the capacitor.

At the resonance, the energy stored in the capacitor is

$$\begin{aligned} P_{QC}(t) &= \frac{1}{2} C v(t)^2 \\ &= \frac{1}{2} C R^2 I_m{}^2 \cos^2 \omega_0 t\,. \end{aligned} \tag{2-4}$$

At the resonance, the energy stored in the inductor is

$$\begin{aligned} P_{QL}(t) = \frac{1}{2} L i_L(t)^2 = \frac{1}{2} L[-i_c(t)]^2 = \frac{1}{2} L\left[C \frac{dv(t)}{dt} \right]^2 \\ = \frac{1}{2} C R^2 I_m{}^2 \sin^2 \omega_0 t\,. \end{aligned} \tag{2-5}$$

The total energy stored is

$$\begin{aligned} P_{QC}(t) + P_{QL}(t) &= \frac{1}{2} C R^2 I_m{}^2 \left[(\cos \omega_0 t)^2 + (\sin \omega_0 t)^2 \right] \\ &= \frac{1}{2} C R^2 I_m{}^2\,. \end{aligned} \tag{2-6}$$

Note that the total energy stored at the resonance is frequency independent.

The energy lost or consumed per time period is

$$\begin{aligned} P_R T &= \frac{1}{2} R I_m{}^2 T \\ &= \frac{\pi R I_m{}^2}{\omega_0}\,. \end{aligned} \tag{2-7}$$

Thus, the quality factor for the parallel *RLC* circuit is then given by

$$Q_f = \frac{2\pi\left(\frac{1}{2}CR^2 I_m{}^2\right)}{\pi R I_m{}^2 / \omega_0} = \omega_0 RC = \frac{R}{\omega_0 L} = R\sqrt{\frac{C}{L}}. \tag{2-8}$$

Note that the quality factor of the parallel *RLC* load is frequency independent. It is worth mentioning that the frequency of the current source was considered to be equal to the resonant frequency of the load so that the voltage across the load is in phase with the current and its magnitude depends only on the value of the resistance of the load.

2.2.3 IMPEDANCE OF PARALLEL *RLC* LOAD

The impedance of a parallel *RLC* load at an arbitrary angular frequency ω is given by:

$$Z_{load} = \frac{1}{\frac{1}{R} + \frac{1}{j\omega L} + j\omega C} = \frac{1}{\frac{1}{R} - j\left(\frac{1}{\omega L} - \omega C\right)}. \tag{2-9}$$

2.2.3.1 Phase Characteristics

The phase angle of the load is

$$\phi_{load} = \tan^{-1}\left[R\left(\frac{1}{\omega L} - \omega C\right)\right]. \tag{2-10}$$

From the definition of the quality factor Q_f and the load resonant angular frequency ω_0, one can get

$$\frac{R}{L} = Q_f\,\omega_0, \qquad RC = \frac{Q_f}{\omega_0}. \tag{2-11}$$

Substitute Equation (2-11) into (2-10), gives

$$\begin{aligned}\phi_{load} &= \tan^{-1}\left[Q_f\left(\frac{\omega_0}{\omega}-\frac{\omega}{\omega_0}\right)\right] \\ &= \tan^{-1}\left[Q_f\left(\frac{f_0}{f}-\frac{f}{f_0}\right)\right].\end{aligned} \tag{2-12}$$

The load current voltage (C-V) phase angle (θ_{load}), that represents the angle by which the current leads the voltage, is given by

$$\theta_{load} = -\phi_{load} = \tan^{-1}\left[Q_f\left(\frac{f}{f_0}-\frac{f_0}{f}\right)\right]. \tag{2-13}$$

The load C-V phase angle $(^\circ)$ vs. frequency characteristic curves with different quality factors and different resonant frequencies are as shown in Fig. 2-3. From Fig. 2-3 (a), one sees that the larger the quality factor, the larger is the variation of the C-V angle for a certain variation of the system frequency around the resonant frequency. Fig. 2-3 (b) shows that the intersection of the load C-V phase angle vs. frequency curves and the zero phase angles always takes place at the resonant frequency. Further, one can see that a load whose resonant frequency is $f_0 < f_g$, is a net capacitive load at grid frequency since the C-V angle is bigger than zero. Conversely, a load whose resonant frequency is $f_0 > f_g$, is a net inductive load at grid frequency.

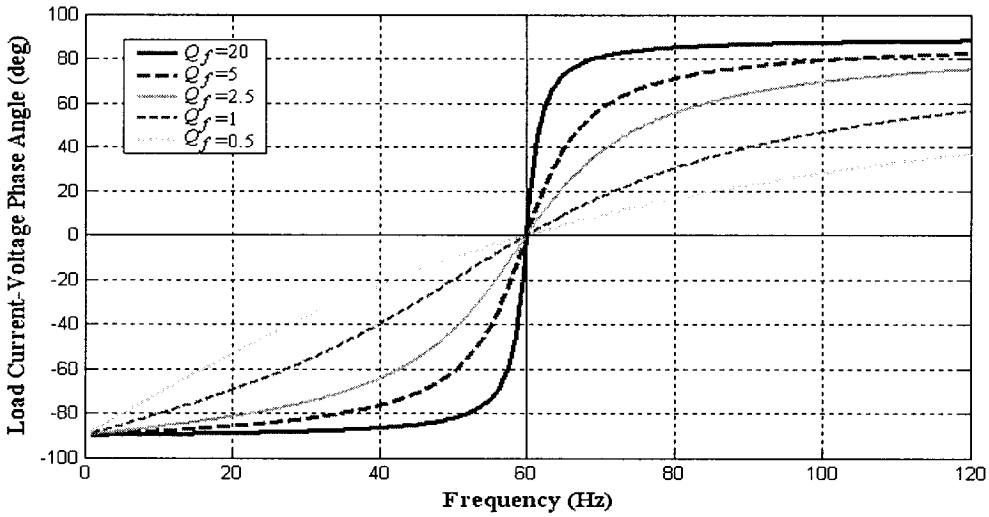

(a) Load with $f_0 = 60Hz$ and different Q_f;

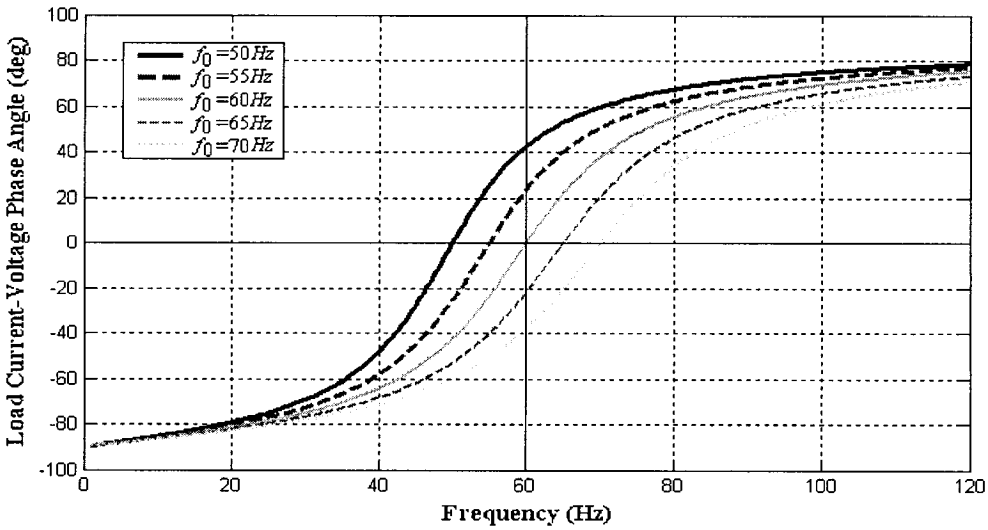

(b) Load with $Q_f = 2.5$ and different f_0.

Fig. 2-3 *RLC* loads C-V phase angle vs. frequency characteristic.

2.2.3.2 Magnitude Characteristics

Substituting (2-11) into (2-9), one obtains an expression for the magnitude of the load as a function of the quality factor and resonant frequency,

$$|Z_{load}| = \frac{1}{\sqrt{\frac{1}{R^2} + \left(\frac{1}{\omega L} - \omega C\right)^2}} = \frac{R}{\sqrt{1 + Q_f{}^2 \left(\frac{f_0}{f} - \frac{f}{f_0}\right)^2}}. \quad (2\text{-}14)$$

Equation is plotted for various values of Q_f in Fig. 2-4, showing the clear relationship between the sharpness of the resonant peak and the Q_f quality factor of the curves.

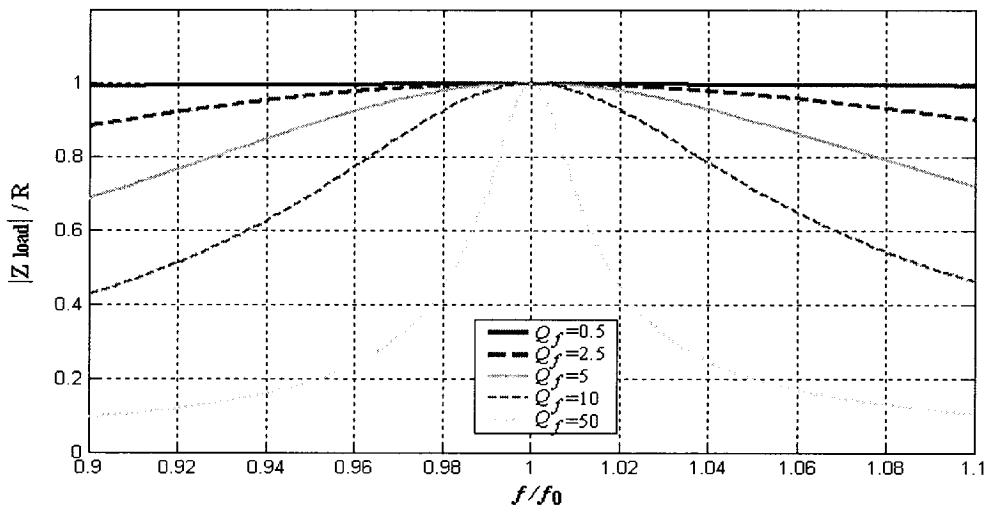

Fig. 2-4 Magnitude response curves as a function of the quality factor Q_f.

There one sees that the larger the quality factor Q_f, the larger is the variation of the magnitude of the load impedance for a given variation in the system frequency. However, for loads with $Q_f < 2.5$, the magnitude of the load impedance changes only 10% for a 10% frequency variation. As a result, when the system frequency varies within the allowed range of the UFP/OFP devices (~ $f_g \pm 1\%$), the variation of the voltage magnitude across the load tends to be negligible. That is why the UFP/OFP devices are more effective than the UVP/OVP devices in detecting islanding for small power imbalances.

2.3 NDZ FOR PASSIVE IDM IN THE ΔP VS. ΔQ SPACE

Usually the PV inverter operates with a unity power factor, i.e. the PV inverter output current I_{PV} is in phase with the PCC voltage V_{PCC}. The reactive power and the real power supplied by the PV system are

$$Q_{PV} = 0, \tag{2-15}$$

$$P_{PV} = I_{PV} V_{PCC}. \tag{2-16}$$

The reactive power and the active power consumed by the load are

$$\begin{aligned} Q_{load} &= \frac{{V_{PCC}}^2}{\omega_{PCC} L} - {V_{PCC}}^2 \omega_{PCC} C \\ &= Q_f P_{load} \left(\frac{f_0}{f_{PCC}} - \frac{f_{PCC}}{f_0} \right), \end{aligned} \tag{2-17}$$

$$P_{load} = \frac{{V_{PCC}}^2}{R}. \tag{2-18}$$

Where $f_{PCC} = f_g$ is the grid frequency and $V_{PCC} = V_g$ is the grid voltage before the grid disconnects.

The behaviour of the system in the steady-state, i.e. the values of the voltage and frequency at the PCC, after the utility disconnects depends on the power mismatches (ΔP and ΔQ) prior to the opening of the utility breaker. The islanding behaviour of grid-connected PV inverter is different when operating under different control schemes [13]. Two different control types of inverter are discussed here. The inverters controlled with constant current and with constant power are analyzed separately.

If after disconnection the steady-state values of the voltage magnitude or of the frequency at the PCC lie outside the limits set for the UVP/OVP and UFP/OFP, islanding is detected, otherwise, islanding occurs.

2.3.1 OBTAINING THE EQUATIONS IN THE ΔP VS. ΔQ SPACE

2.3.1.1 NDZ due to active power mismatch

a) Inverter operating with constant current control

In this case, after grid disconnection, $V_{is} = I_{PV} R$. Thus,

$$\begin{aligned} \frac{\Delta P}{P_{PV}} &= \frac{P_{load} - P_{PV}}{P_{PV}} \\ &= \frac{V_g^{\,2} / R - V_g I_{PV}}{V_g I_{PV}} \\ &= \frac{V_g}{V_{is}} - 1. \end{aligned} \tag{2-19}$$

Considering that the magnitude of the PCC voltage has to be within the UVP/OVP trip threshold in order to keep run-on in islanding condition, the real power mismatch has to be within the range:

$$\frac{V_g}{V_{\max}} - 1 \le \frac{\Delta P}{P_{PV}} \le \frac{V_g}{V_{\min}} - 1. \tag{2-20}$$

An inverter with UVP/OVP trip at $88\% \le V \le 110\%$ its nominal value will have a NDZ for a corresponding load $\frac{P_{load}}{P_{PV}} \propto \frac{V_g}{V_a}$, ranging of up to 113.63% down to 90.9% inverter active power. The active power mismatch ranges:

$$-9.09\% \le \frac{\Delta P}{P_{PV}} \le 13.63\%. \tag{2-21}$$

b) Inverter operating with constant power control

In this case, after grid disconnection, $V_{is} = \sqrt{P_{PV} R}$. Thus,

$$\frac{\Delta P}{P_{PV}} = \frac{P_{load} - P_{PV}}{P_{PV}} = \frac{V_g^2/R - V_{is}^2/R}{V_{is}^2/R} = \frac{V_g^2}{V_{is}^2} - 1. \quad (2\text{-}22)$$

Hence, the active power mismatch for run-on islanding has to be within:

$$\frac{V_g^2}{V_{\max}^2} - 1 \le \frac{\Delta P}{P_{PV}} \le \frac{V_g^2}{V_{\min}^2} - 1. \quad (2\text{-}23)$$

An inverter with UVP/OVP trip values set at $88\% \le V \le 110\%$ its nominal value will have a NDZ for a corresponding load $\frac{P_{load}}{P_{PV}} \propto \frac{V_g^2}{V_{is}^2}$, ranging of up to 129.13% down to 82.64% inverter active power. The active power mismatch ranges:

$$-17.36\% \le \frac{\Delta P}{P_{PV}} \le 29.13\%. \quad (2\text{-}24)$$

2.3.1.2 NDZ due to reactive power mismatch

Unlike the NDZ in [5], i.e. in Fig. 2-1, we do consider that there is active power mismatch, $P_{load} \neq P_{PV}$ for deriving equations related to the reactive power mismatch and its influence on the system frequency.

a) Inverter operating with constant current control

The reactive power mismatch can be represented by

$$\begin{aligned}\frac{\Delta Q}{P_{PV}} &= \frac{Q_{load}}{P_{PV}} \\ &= \frac{Q_f P_{load}\left(\frac{f_0}{f_g} - \frac{f_g}{f_0}\right)}{P_{PV}} \\ &= Q_f\left(\frac{f_0}{f_g} - \frac{f_g}{f_0}\right)\frac{V_g}{V_{is}}.\end{aligned} \tag{2-25}$$

Hence, the boundaries of NDZ due to the reactive power mismatch can be represented by

$$Q_f\left(\frac{f_{\max}}{f_g} - \frac{f_g}{f_{\max}}\right)\frac{V_g}{V_{\max}} \le \frac{\Delta Q}{P_{PV}} \le Q_f\left(\frac{f_{\max}}{f_g} - \frac{f_g}{f_{\max}}\right)\frac{V_g}{V_{\min}}, \text{ when } f_0 = f_{\max}; \tag{2-26a}$$

$$Q_f\left(\frac{f_{\min}}{f_g} - \frac{f_g}{f_{\min}}\right)\frac{V_g}{V_{\max}} \le \frac{\Delta Q}{P_{PV}} \le Q_f\left(\frac{f_{\min}}{f_g} - \frac{f_g}{f_{\min}}\right)\frac{V_g}{V_{\min}}, \text{ when } f_0 = f_{\min}. \tag{2-26b}$$

b) Inverter operating with constant power control

The reactive power mismatch can be expressed as

$$\begin{aligned}\frac{\Delta Q}{P_{PV}} &= \frac{Q_{load}}{P_{PV}} \\ &= \frac{Q_f P_{load}\left(\frac{f_0}{f_g} - \frac{f_g}{f_0}\right)}{P_{PV}} \\ &= Q_f\left(\frac{f_0}{f_g} - \frac{f_g}{f_0}\right)\frac{V_g^{\,2}}{V_{is}^{\,2}}.\end{aligned} \tag{2-27}$$

Hence, the boundaries of NDZ due to the= reactive power mismatch are

$$Q_f\left(\frac{f_{\max}}{f_g} - \frac{f_g}{f_{\max}}\right)\frac{V_g^{\,2}}{V_{\max}^{\,2}} \le \frac{\Delta Q}{P_{PV}} \le Q_f\left(\frac{f_{\max}}{f_g} - \frac{f_g}{f_{\max}}\right)\frac{V_g^{\,2}}{V_{\min}^{\,2}}, \textit{when } f_0 = f_{\max}; \tag{2-28a}$$

$$Q_f\left(\frac{f_{\min}}{f_g} - \frac{f_g}{f_{\min}}\right)\frac{V_g^{\,2}}{V_{\max}^{\,2}} \le \frac{\Delta Q}{P_{PV}} \le Q_f\left(\frac{f_{\min}}{f_g} - \frac{f_g}{f_{\min}}\right)\frac{V_g^{\,2}}{V_{\min}^{\,2}}, \textit{when } f_0 = f_{\min}. \tag{2-28b}$$

2.3.2 OBTAINING THE NDZ IN THE ΔP VS. ΔQ SPACE

The NDZs of a unity power factor inverter equipped with passive UFP/OFP and

UVP/OVP protection devices in the ΔP vs. ΔQ space are shown in Fig. 2-5 for different types of control schemes and values of Q_f. In Fig. 2-5, CP represents the constant power controlled inverter and CC represents the constant current controlled inverter. It is assumed that the inverter is connected to a 120V-60Hz grid and that the limits for the UFP/OFP and UVP/OVP devices in this case are $106\,V \le V_{is} \le 132\,V$ and $59.3\,Hz \le f_0 \le 60.5\,Hz$, respectively.

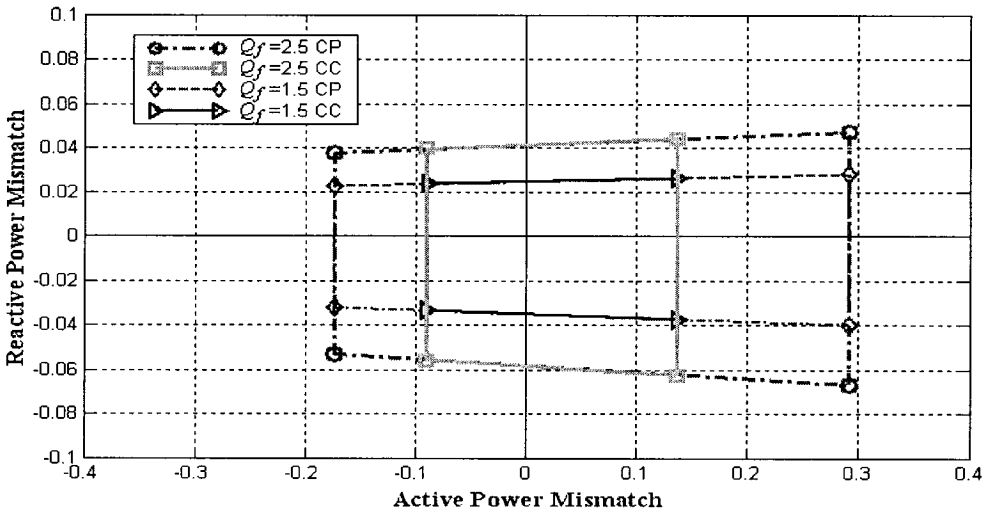

Fig. 2-5 NDZ of a unity power factor inverter in the ΔP vs. ΔQ space.

One sees in Fig. 2-5 that the boundaries for the NDZ on the top and bottom, due to the reactive power mismatch, are imposed by the OFP and UFP, respectively and that they vary with Q_f but not with the type of control of the inverter. The larger Q_f, the larger is the NDZ. The boundaries for the NDZ on the left and right sides of the curves, due to the active power mismatch, are imposed by the OVP and UVP, respectively. Note that they vary with the type of control of the inverter but not with Q_f. The NDZ of the inverter with constant current control is smaller than that of the inverter with constant power control. Overall, the passive IDM is more sensitive to reactive power mismatches than to active mismatches, since lower percentage values of ΔQ can trigger the UFP/OFP devices.

The NDZ shown in Fig. 2-5 is based on steady-state values assuming that neither the voltage nor the frequency limits have reached for 6 consecutive line cycles the following outer boundary values, shown in Table 1. It is evident that to cause a larger drift in the frequency and voltage values larger power mismatches are required, meaning a larger NDZ, but the tripping of the UFP/OFP and UVP/OVP devices would happen in 6 line cycles instead of 120 line cycles. However, since what matters the most is the prevention of run-on islanding conditions and not if it will be detected in 6 or 120 line cycles, the NDZ shown in Fig. 2-5 is the one used for the performance assessment of the IDM.

The NDZ in ΔP vs. ΔQ space is the traditional index to describe the performance of the Passive IDM. However, one can see from the Fig. 2-5, the NDZ is different when Q_f is different. To compare the effectiveness of the different IDMs, the load quality factor Q_f has to be indicated. As will be shown in Section 2.5, for some load quality factors Q_f, the effectiveness of the different IDMs are the same. Thus, in order to assess the effectiveness of the IDMs by the NDZ in ΔP vs. ΔQ space, several NDZs of the different IDMs have to be mapped for a certain range of the load quality factors Q_f. Thus, NDZ in a space defined as a load normalized capacitance C_{norm} vs. the load inductance L has been reported in [8] to overcome the inconvenience of the NDZ in the ΔP vs. ΔQ space.

2.4 C_{NORM} VS. L LOAD PARAMETER SPACE

The concept of non-detection zones (NDZ) has also been applied to a load parameter space [8] based on the actual values of the *RLC* elements of the local load. The NDZs of the islanding prevention methods are mapped into a space defined by the load normalized capacitance C_{norm} vs. the load inductance L. The normalized capacitance, C_{norm} is

defined as the load capacitance, C, divided by the capacitance C_{res} that resonates with the load inductance L at the grid utility frequency $\omega_g = 2\pi f_g$,

$$C_{norm} = \frac{C}{C_{res}} = C L \omega_g^{\,2}. \tag{2-29}$$

The principle behind the load parameter space is called the phase criteria and reflects the fact that reactive power consumed by the load has to be equal to that supplied by the inverter in the steady-state. It says that the frequency of an islanded system in the steady-state condition is that where the phase angle of the local load (θ_{load}) is equal to that of the inverter (θ_{inv}). The phase angle of an *RLC* load varies with the system frequency as described in Section 2.2.3.1. The phase angle of an inverter with active IDM varies with the system frequency and a particular given control parameter of the method. These are described in the next section for three types of active IDMs.

The derivation of the non-detection zones for the C_{norm} vs. L load parameter space was described in [6] for an inverter with active frequency drift (AFD) IDM. Employing the phase criteria, one gets

$$\arg\left\{R^{-1} + (j\omega L)^{-1} + j\omega C\right\}^{-1} = 0.5\pi cf. \tag{2-30}$$

where cf is the chopping factor, the control parameter of AFD IDM.

The procedure proposed in [8] for mapping the NDZ of the IDM into the C_{norm} vs. L plane is the following: First select the value of resistance R and inductance L, and then choose a value of capacitance C over a range near the value which resonates with the chosen L. For this capacitance C, calculate the frequency ω that satisfies (2-30). If this frequency ω is inside the frequency trip limit of the PV system, this *RLC* load lies inside the NDZ of AFD. If this frequency ω is outside the frequency trip limit, this load lies outside the NDZ of AFD. Repeat the calculation until the boundary value of

capacitance C, at which the frequency ω satisfies (2-30) coincides with frequency threshold is found. Then choose another value of inductance L and repeat the process again until enough points have been obtained to plot the NDZ curve. In [5], MATLAB was used to carry out this time consuming calculation.

In addition to the time consuming calculation required, the NDZ in C_{norm} vs. L space has another disadvantage that for different resistance R, the above procedure has to be repeated to map a new set of NDZ curve. Fig. 2-6 shows the AFD NDZ with $cf = 5\%$ for different resistance values (R). There one sees that the size and the shape of the NDZs are different for different values of R. Note that the values of the resistance have to be specified in order to compare the effectiveness of different islanding detection methods.

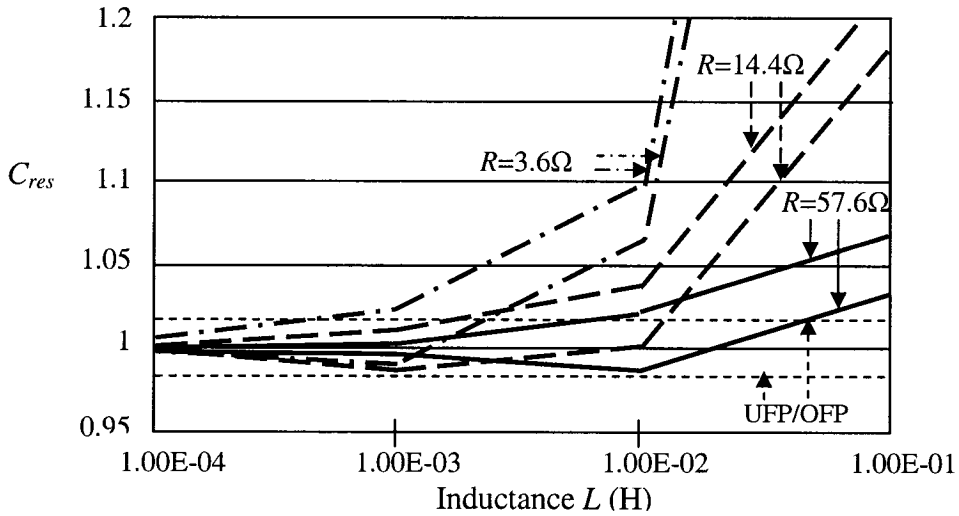

Fig. 2-6 Mapping of the NDZ of the AFD IDM in the C_{norm} vs. L space [6].

Therefore, the NDZ in the C_{norm} vs. L space is capable but not very convenient to compare the performance of different IDMs due to the fact that NDZ in C_{norm} vs. L space is a result of a long sequence of calculation. Moreover, the NDZ in this space is not generic enough to cover different load values since it requires different curves for different values of load resistance R. A new Q_f vs. f_0 load parameter is proposed in the next

section, which can maintain the advantage of the C_{norm} vs. L space and also overcome the shortage of the C_{norm} vs. L space.

2.5 PROPOSED Q_f VS. f_0 LOAD PARAMETER SPACE

Most active IDMs employ a strategy to drift the frequency of the islanded system and trip the UFP/OFP since a significant active power mismatch is required to trip the UVP/OVP devices. The frequency of an islanded system with a unity power factor inverter is primarily affected by the resonant frequency f_0 of the *RLC* load. If the inverter operates with unity power factor and no disturbances are introduced, the frequency of the islanded system f_{is} will be the same as the resonant frequency f_0 since the resonant frequency f_0 is the only frequency that satisfies $Q_{load} = Q_{PV} = 0$. Alternatively, one can also say that the load angle has to be equal to the phase angle between the inverter current and the load voltage. One sees from Equation (2-13) that the load angle is also affected by the load quality factor Q_f that reflects the resistive element of the load. Therefore, a Q_f vs. f_0 load-parameter space is a good choice for showing the NDZs and for comparing the performance of active IDMs. For a given set of *L* and *C*, an increase in *R* is reflected by an increase in Q_f. There is no need to plot a new set of curves as for the C_{norm} vs. L load parameter space proposed in [8] and shown in Fig. 2-6.

The following sections present the derivation of the NDZ boundaries for some IDMs in the Q_f vs. f_0 space. The first step is the derivation of an equation that shows how the phase angle of the inverter for that IDM varies with the frequency at the PCC. Then one uses the phase criteria, which is the fact that the load angle $\theta_{load}(f)$ and inverter angle $\theta_{inv}(f)$ are the same at the steady-state frequency,

$$\theta_{load}(f) = \theta_{inv}(f), \tag{2-31}$$

to calculate the boundaries of the NDZ in the Q_f vs. f_0 space.

Unlike the analysis in the ΔP vs. ΔQ space, there is no need to derive equations separately for constant current and constant power controlled inverters since these factors have no influence on the NDZ boundaries of the UFP/OFP devices as shown in Section 2.3.2.

In order to calculate the boundaries for islanding detection one needs to obtain an equation that represents the steady-state frequency of the voltage across the PCC as a function of the load parameters (Q_f and f_0) and also as a function of the main parameters of the active IDM methods. Therefore, from (2-13) and (2-31),

$$\tan^{-1}\left[Q_f\left(\frac{f}{f_0}-\frac{f_0}{f}\right)\right]=\theta_{inv}(f). \tag{2-32}$$

Thus, one can get

$$f_0^{\,2}+\frac{\tan\theta_{inv}(f)f}{Q_f}f_0-f^2=0. \tag{2-33}$$

Then the resonant frequency f_0 which will cause the islanding operation can be solved as the function of the islanding frequency f_{is} and the inverter equivalent angle, and the negative value can be neglected:

$$f_0=\frac{f_{is}}{2Q_f}\left(-\tan\theta_{inv}(f_{is})+\sqrt{\tan^2\theta_{inv}(f_{is})+4Q_f^{\,2}}\right). \tag{2-34}$$

In order to calculate the NDZ, one imposes the islanding frequency to be a threshold frequency ($f_{\max}$ and $f_{\min}$), varies the value of Q_f and then calculates the resonant frequency of the load at the threshold of the NDZ. Thus, the NDZ can be plotted by applying Equation (2-34). The key problem now is to find the equivalent inverter angle.

2.5.1 NDZ OF UFP/OFP

According to Equation (2-13), whenever the load is supplied by a stand-alone inverter operating with current control and unity power factor, the frequency of the inverter- local load system will be the resonant frequency f_0 of the load. Also, the same result can be obtained from Equation (2-34) by applying the

$$\theta_{UFP/OFP} = 0, \tag{2-35}$$

since the UFP/OFP does not apply any disturbance to the current, to Equation (2-34). One can get

$$f_0 = f_{is}. \tag{2-36}$$

If $f_{\min} \le f_0 \le f_{\max}$, UFP/OFP devices will not trip and islanding will occur regardless of the value of Q_f. NDZ of UFP/OFP is shown in Fig. 2-7, Fig. 2-8, and Fig. 2-9.

2.5.2 NDZ OF AFD IDM

The operating principles of this method were discussed in Section 1.4. There, it was shown that the angle between the fundamental component of the inverter current and the voltage at the PCC is,

$$\theta_{AFD}(f) = \frac{\pi \delta f}{f + \delta f}. \tag{2-37}$$

By substituting Equation (2-37) into (2-34) and replacing the islanding frequency f_{is} by the frequency threshold $f_{\max}$ and $f_{\min}$, the boundary of the NDZ of AFD will be obtained by

$$f_{0\max} = \frac{f_{\max}}{2Q_f}\left(-\tan\theta_{AFD}(f_{\max}) + \sqrt{\tan^2\theta_{AFD}(f_{\max}) + 4Q_f^{\,2}}\right), \tag{2-38a}$$

$$f_{0\min} = \frac{f_{\min}}{2Q_f}\left(-\tan\theta_{AFD}(f_{\min}) + \sqrt{\tan^2\theta_{AFD}(f_{\min}) + 4Q_f^{\,2}}\right). \tag{2-38b}$$

According to Equation (2-38), the NDZ of the AFD will be mapped as shown in Fig. 2-7. Fig. 2-7 shows the NDZ for speed-up mode AFD IDM for different values of δf and for a normal frequency range of $59.3\,Hz \le f \le 60.5\,Hz$. There one sees that the main effect of the AFD is to shift the NDZ to lower values of f_0 as δf increases. For $Q_f = 2.5$ and $\delta f = 0.5\,Hz$ the method will fail to detect islanding for loads with $58.99\,Hz \le f_0 \le 60.19\,Hz$. If δf is increased to $1\,Hz$, islanding will occur for loads with $58.69\,Hz \le f_0 \le 59.89\,Hz$ for $Q_f = 2.5$ case. Recall that most practical loads are inductive at line frequency, presenting a resonant frequency larger than the line frequency. Thus according to Fig. 2-7, no islanding would occur for inductive loads with $Q_f < 3$ if speed-up AFD IDM with $\delta f = 1\,Hz$ is used. Loads that are slightly capacitive at rated line frequency, which presents a resonant frequency slightly lower than the line frequency, can be protected from islanding by increasing δf. It is worth mentioning that the size of the range of resonant frequencies $\Delta f_0 = f_{0\max} - f_{0\min}$ for which islanding occurs is the same as of the UFP/OFP: 1.2 Hz. That is, capacitive loads that would not yield islanding with passive IDM ($\delta f = 0$), do with speed-up AFD IDM as explained before.

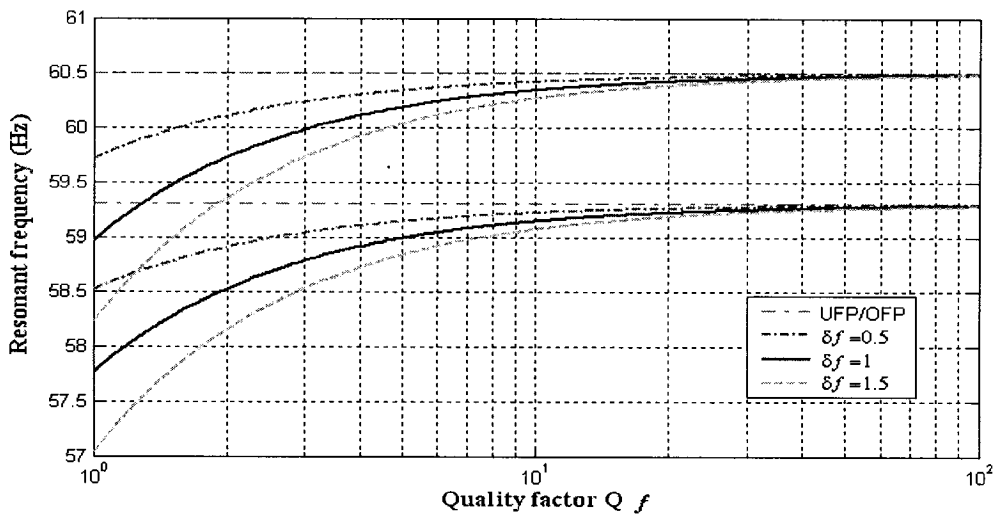

Fig. 2-7 NDZs of AFD IDM for different values of δf.

2.5.3 NDZ OF SMS IDM

The operating principles of the slip mode phase shift (SMS) method were discussed in Section 1.5. The phase angle of the inverter was shown to be

$$\theta_{SMS} = \frac{2\pi}{360}\theta_m \sin\left(\frac{\pi}{2}\frac{f - f_g}{f_m - f_g}\right). \tag{2-39}$$

The parameters of the SMS should be designed so that no stable operation point will be reached inside the frequency threshold. As discussed in Chapter 1, the phase of the inverter should increase faster than the phase of the *RLC* load with resonant frequency in the region near the grid frequency, in order to make sure that SMS could work at the worst case, referred to Fig. 1-3, $f = f_0 = f_g$,

$$\left.\frac{d\,\theta_{load}}{d\,f}\right|_{f=f_0} \le \left.\frac{d\,\theta_{SMS}}{d\,f}\right|_{f=f_g}. \tag{2-40}$$

From Equation (2-13), the gradient of the load phase is

$$\begin{aligned}\left.\frac{d\,\theta_{load}}{d\,f}\right|_{f=f_0} &= \left.\frac{d\left\{\tan^{-1}\left[Q_f\left(\frac{f}{f_0}-\frac{f_0}{f}\right)\right]\right\}}{d\,f}\right|_{f=f_0} \\ &= \left.\frac{Q_f\left(\frac{f_0}{f^2}+\frac{1}{f_0}\right)}{1+\left[Q_f\left(\frac{f_0}{f}-\frac{f}{f_0}\right)\right]^2}\right|_{f=f_0} \\ &= \frac{2Q_f}{f_0}.\end{aligned} \tag{2-41}$$

In degree $(^\circ)$,

$$\left.\frac{d\,\theta_{load}(^\circ)}{d\,f}\right|_{f=f_0} = \frac{360}{\pi}\frac{Q_f}{f_0}. \tag{2-42}$$

From Equation (2-39), the gradient of the inverter phase is

$$\left.\frac{d\,\theta_{SMS}(^\circ)}{d\,f}\right|_{f=f_0} = \left.\frac{d\left[\theta_m \sin\left(\frac{\pi}{2}\frac{f-f_g}{f_m-f_g}\right)\right]}{d\,f}\right|_{f=f_g}$$

$$= \left.\frac{\pi}{2}\frac{\theta_m}{f_m-f_g}\cos\left(\frac{\pi}{2}\frac{f-f_g}{f_m-f_g}\right)\right|_{f=f_g} \tag{2-43}$$

$$= \frac{\pi}{2}\frac{\theta_m}{f_m-f_g}.$$

Substituting Equation (2-42) and (2-43) into (2-40), gives

$$\theta_m \geq \frac{12Q_f}{\pi^2}\left(f_m - f_g\right), \tag{2-44}$$

which is a function of the load quality factor Q_f and one sees that as it increases, for a given value of $f_m - f_g$, usually taken as $3Hz$ [10], θ_m has to increase. This also increases the reactive power absorbed by the inverter under normal conditions ($PF = \cos\theta_{SMS}$). Therefore, from Equation (2-44), θ_m can be chosen according to the load quality factor below which the islanding is expected to be detected by SMS. From IEEE Std. 929-2000 [2], the worst case happens when load $Q_f = 2.5$, and the load resonant frequency nears the grid frequency $f_0 = f_g = 60Hz$. Thus, the SMS system is designed for a worst case load condition $Q_f = 2.5$ above which it fails to detect islanding. For detecting load with $Q_f < 2.5$ case, when $f_m - f_g = 3\ Hz$, one calculates $\theta_m = 10^\circ$.

As that of AFD, the NDZ of SMS can be obtained by substituting Equation (2-39) into (2-34). Thus, the boundary of the NDZ of AFD will be obtained as

$$f_{0\max} = \frac{f_{\max}}{2Q_f}\left(-\tan\theta_{SMS}(f_{\max}) + \sqrt{\tan^2\theta_{SMS}(f_{\max}) + 4Q_f{}^2}\right), \textit{ when } f_{0\max} > f_g\ ; \tag{2-45a}$$

$$f_{0\min} = \frac{f_{\min}}{2Q_f}\left(-\tan\theta_{SMS}(f_{\min}) + \sqrt{\tan^2\theta_{SMS}(f_{\min}) + 4Q_f{}^2}\right), \textit{ when } f_{0\min} < f_g\ ; \tag{2-45b}$$

$$f_{0\max} = f_{0\min} = f_g . \tag{2-45c}$$

One thing needed to be mentioned is that from Equation (2-45), the value of the upper boundary $f_{0\max}$ may be less than f_g and the value of the lower boundary $f_{0\min}$ may be larger than f_g. However, actually, this is not going to happen. For a PV inverter with SMS, if the load resonant frequency $f_0 > f_g$, the PCC voltage frequency tends to increase when islanded, and positive θ_{SMS} is regarded as higher frequency, further increasing the frequency until it reaches the steady-state; if the load resonant frequency $f_0 < f_g$, the PCC voltage frequency tends to decrease when islanded, and negative θ_{SMS} is regarded as lower frequency, further decreasing the frequency until it reaches the steady-state. Thus, for the calculated values of upper boundary $f_{0\max} < f_g$ and the calculated values of lower boundary $f_{0\min} > f_g$ case, the boundary of the SMS is $f_{0\max} = f_{0\min} = f_g$, as Equation (2-45c), at which the undetectable islanding would occur for the load resonant frequency $f_0 = f_g$ of the perfect no disturbance system, shown in the Fig. 2-8. However, technically, the system with no disturbance does not exist. In this case, the operation point is unstable, whenever there is disturbance in the system, and the system frequency will either increase or decrease until the UFP/OFP device detects the islanding.

The resulting NDZ for SMS IDM in the Q_f vs. f_0 space is shown in Fig. 2-8 for different values of θ_m from Equation (2-45). There one sees that the NDZ is null for $Q_f < 2.7$ when $\theta_m = 10°$ and $f_m - f_g = 3\,Hz$, that are typical values for SMS IDM, as analyzed above. Besides, as θ_m decreases, the load quality factor for which islanding occurs also decreases. Finally, one sees that the performance of this active IDM is equivalent to that of passive UFP/OFP ($\theta_m = 0°$) for loads with high Q_f, where

islanding occurs for loads with a resonant frequency between $f_{\max} = 60.5\,Hz$ and $f_{\min} = 59.3\,Hz$. Fortunately these loads are seldom found in practice.

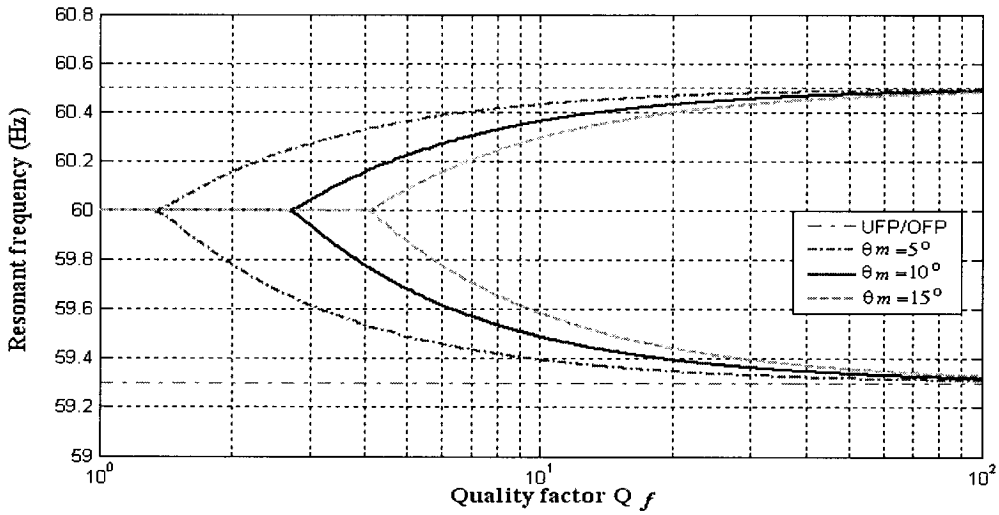

Fig. 2-8 NDZs of SMS for different values of θ_m and with $f_m - f_g = 3\ Hz$.

2.5.4 NDZ OF SFS IDM

The operating principles of the Sandia frequency shift (SFS) method were discussed in Section 1.6. The phase angle of the inverter has shown in Equation (1-8) to be

$$\theta_{SFS}(f) = \frac{\pi c f(f)}{2}. \tag{2-46}$$

As the analysis of the NDZ of AFD, in order to obtain the boundary of the NDZ of SFS, substituting Equation (2-46) into (2-34), gives the boundary of the NDZ of AFD will be obtained as

$$f_{0\max} = \frac{f_{\max}}{2Q_f}\left(-\tan\theta_{SFS}(f_{\max}) + \sqrt{\tan^2\theta_{SFS}(f_{\max}) + 4Q_f{}^2}\right),\ when\ f_{0\max} < f_{0\min}\ ; \text{(2-47a)}$$

$$f_{0\min} = \frac{f_{\min}}{2Q_f}\left(-\tan\theta_{SFS}(f_{\min}) + \sqrt{\tan^2\theta_{SFS}(f_{\min}) + 4Q_f{}^2}\right),\ when\ f_{0\max} < f_{0\min}\ ; \text{(2-47b)}$$

$$f_{0\max} = f_{0\min} = \frac{f_g}{2Q_f}\left(-\tan\theta_{SFS}(f_g) + \sqrt{\tan^2\theta_{SFS}(f_g) + 4Q_f{}^2}\right),\ when\ f_{0\max} = f_{0\min}\ . \text{(2-47c)}$$

One thing that needs to be mentioned is that from Equation (2-47), the value of the upper boundary $f_{0\max}$ may be less than $f_{0\min}$. However, theoretically, $f_{0\max} \geq f_{0\min}$. Boundary $f_{0\max} = f_{0\min}$ is the load case at which the system island frequency is $f_{is} = f_g$ when islanded, so that from Equation (1-7) no extra deviation will be applied. The islanding frequency will stay at grid frequency if there is no disturbance. The NDZ of the SFS is in Fig. 2-9.

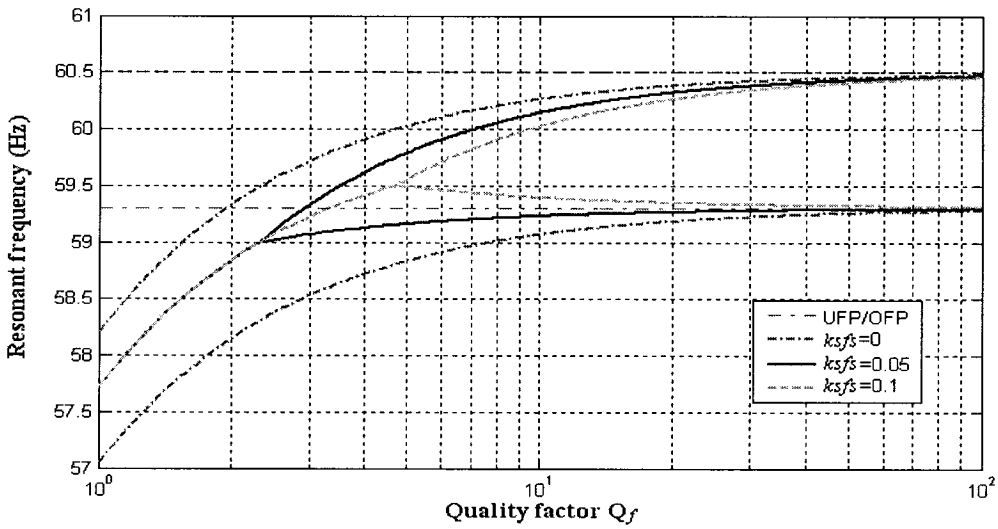

Fig. 2-9 NDZs of SFS for different k_{sfs}.

Fig. 2-9 shows the calculation results of the NDZ of SFS. There one sees that the NDZ is null for loads with $Q_f < 4.8$ when $k_{sfs} = 0.1$. Besides, as k_{sfs} decreases, the load quality factor for which islanding occurs also decreases. Actually, for $k_{sfs} = 0$ this method becomes the AFD, where for all values of Q_f there will be loads (capacitive mostly) that will lead to islanding. Finally, one sees that the performance of this active IDM is equivalent to that of passive UFP/OFP for loads with high Q_f, where islanding occurs for loads with a resonant frequency between $f_{\max} = 60.5\,Hz$ and $f_{\min} = 59.3\,Hz$.

2.6 CONCLUSION

This chapter focused on the analysis of methods required to assess the effectiveness of passive and active islanding detection methods (IDMs). It started with the analysis of the effectiveness of passive islanding detection methods in the ΔP vs. ΔQ space. Equations that represent the non-detection zones (NDZ) of unity power factor current controlled inverters with constant current and constant power were derived. They match very well the NDZ curves that have been obtained by simulation in the literature. Then, it proposed a new load parameter space, based on the quality factor and resonant frequency of the load: A Q_f vs. f_0 space. The main advantage of this space is that the influence of the variation of the resistive element of the load on the effectiveness of the IDM can be carried out with a single curve. Examples of the derivation of equations that describe the NDZs of three active IDMs were presented and their validity will be verified with simulation results in Chapter 3.

CHAPTER 3
SIMULATION RESULTS

3.1 INTRODUCTION

In this chapter, the validation of the theoretical analysis and equations that describe the NDZ of three common active IDMs, AFD, SMS, and SFS, in the proposed Q_f vs. f_0 space was performed with simulation by use of Matlab Simulink. Section 3.2 describes the detail of the simulation schematics, and the circuit of four main blocks, Hysteresis Control, Frequency and RMS, UVP/OVP & UFP/OFP, and Reference Current with IDMs. Section 3.3 presents the simulation results for three active IDMs and compares the simulation results with the theoretical result. Conclusions are stated in Section 3.4.

3.2 SIMULATION SCHEMATICS

The system described in Fig. 1-1 was modeled with MATLAB Simulink as shown in Fig. 3-1. A PV array, represented by a DC voltage source, is connected to the PCC by a current controlled voltage source inverter with hysteresis control. The local load is represented by a parallel *RLC* block with variable resonant frequency and quality factor. The grid breaker, that connects the grid (ac voltage source) to the PCC, is preset to open at a prescribed time. The reference current with IDMs block is used to generate the inverter reference current with the islanding detection methods that match the local load's active power. The frequency and RMS block measures the frequency and the RMS value of the PCC voltage, and UVP/OVP & UFP/OFP block would generate a fault signal to shut down the inverter if its frequency or voltage exceed the IEEE Std. 929-2000 limits, shown in Table 1. The manual switch is used to deactivate the frequency and the voltage

protection thus allowing the measurement of the steady-state values of frequency and voltage across the load under islanding condition.

The universal bridge block implements a bridge of selected power electronic devices. The ideal current measurement blocks are connected in series with the main circuit to measure the current; and the ideal voltage measurement blocks are connected in parallel with the main circuit to measure the voltage. The Scopes block is applied to show the desired curves, including PCC voltage V_{PCC}, grid voltage V_g, reference current I_{ref}, inverter output current I_{PV}, grid ac current I_{ac}, load current I_{load}, magnitude of the PCC voltage RMS, and frequency of PCC voltage f_{PCC}, and the fault signal. Terminators are used to terminate the output signals to prevent the warning about unconnected output ports when the simulation is running. The Matlab Simulink model of the grid-connected PV system is discrete system sampled at simulation sampling rate of 3240 samples per cycle of $60\ Hz$, i.e. $T_s = 5.144 \times 10^{-6}\ s$.

In the model, the value of the grid voltage is preset as $V_g = 120\ V$, $f_g = 60\ Hz$. The value of DC power supply generated by the PV array is preset as $V_{dc} = 250\ V$. The value of the line equivalent inductance is set as $L_{line} = 5\ mH$. The bandwidth of the hysteresis control is preset as $h = 0.5\ A$.

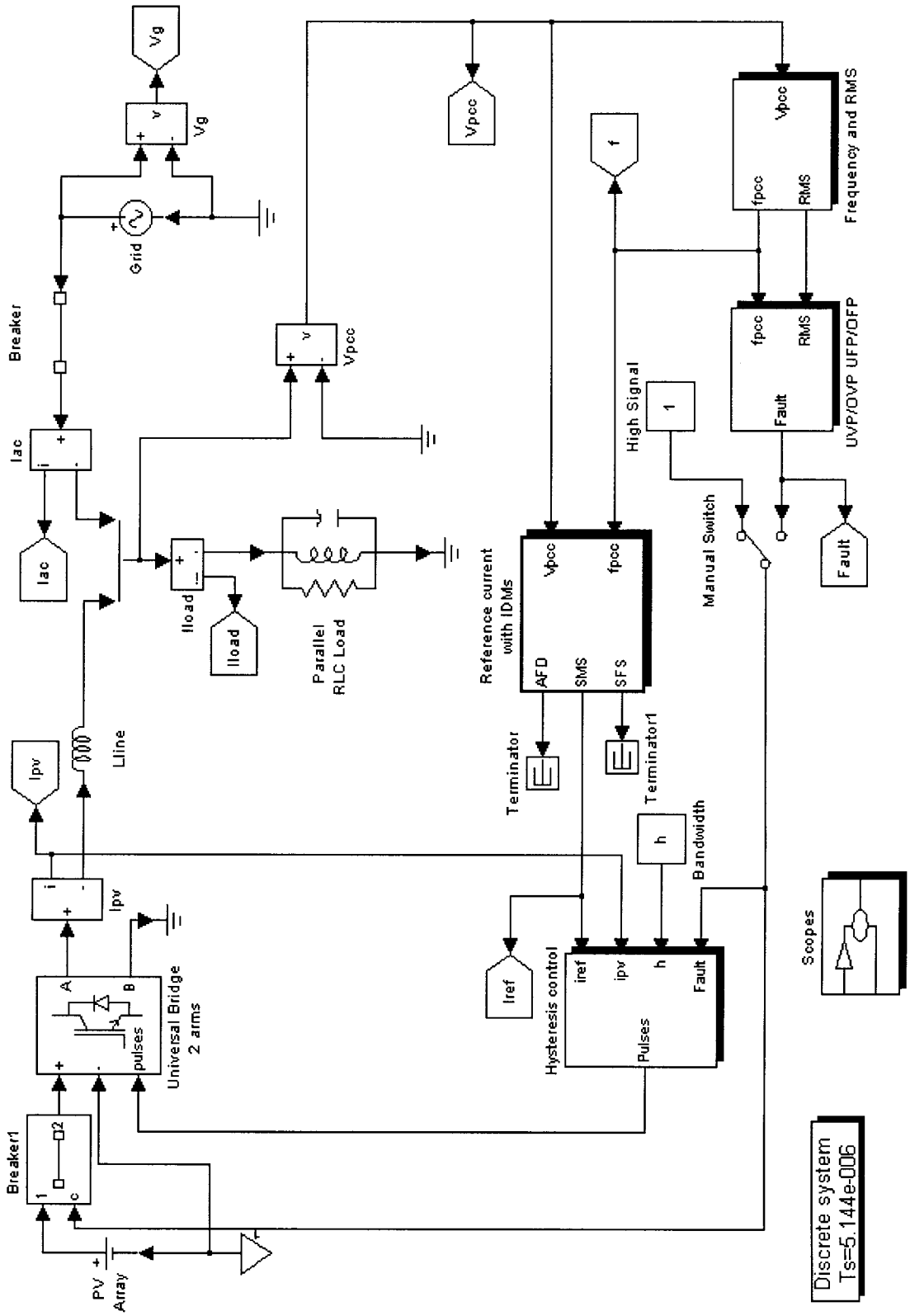

Fig. 3-1 MATLAB Simulink model of the grid-connected PV system.

3.2.1 Hysteresis Control Block

Three major classes of regulators have been developed over the last few decades: hysteresis regulators, linear PI regulators and predictive dead-beat regulators [15]. A short review of the available current control schemes is presented in [16]. The hysteresis band current control is used very often because of its simplicity of implementation. Besides, it has been proven to be the most suitable solution for all the applications of current controlled voltage source inverters where performance requirements are more demanding, such as high-performance ac power conditioners. As it is well known, the hysteresis control is characterized by unconditioned stability, very fast response, and good accuracy and the method does not need any knowledge of load parameters.

The basic implementation of hysteresis current control is based on deriving the switching signals from the comparison of the current error with a fixed tolerance band. This control is based on the comparison of the actual phase current with the tolerance band around the reference current. The single-phase full-bridge inverter represented by Universal Bridge 2 arms in Fig. 3-1, is redrawn in Fig. 3-2. The output current i_o is the inverter output current i_{PV}.

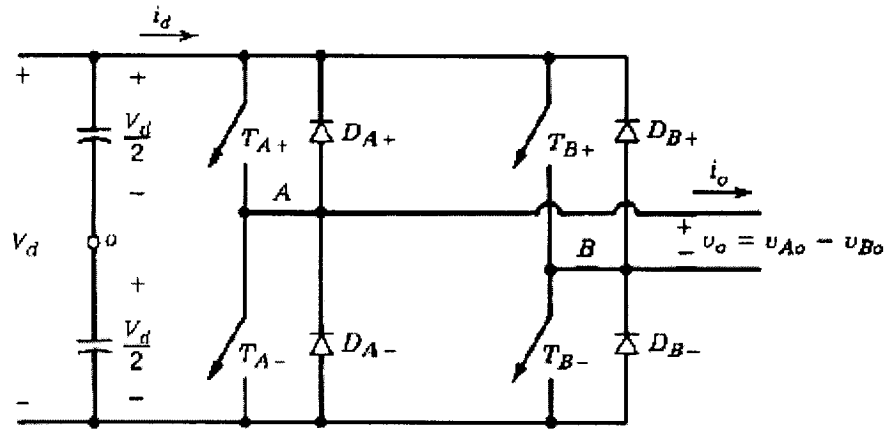

Fig. 3-2 Single-phase full-bridge inverter.

3.2.1.1 Switching Function

In the simulation, the inverter is controlled with two-level hysteresis control. The concept of switching states S is introduced to describe the state the inverter of switches.

At switching state $S=1$, switches T_{A+} and T_{B-} are ON, and T_{A-} and T_{B+} are OFF, and the current increases. When the current exceeds the upper bound defined as $i_{ref}+h$, the switching state is changed to $S=-1$. Then, switches T_{A+} and T_{B-} are OFF, and T_{A-} and T_{B+} are ON, and the current decreases until it reaches the lower bound defined as $i_{ref}-h$. Again, the switching state is changed to $S=1$ and again the ascending trajectory is followed. Thus, by alternately switching states between $S=1$ and $S=-1$, the current is kept within the upper and lower bounds. The current $i_o(t)$ tracks the reference current i_{ref} within the tolerance band.

The waveform of the inverter current can be obtained as follows. From the Kirchhoff's Voltage Law, one obtains an equation for current i_o as a function of the switching state of the inverters.

$$L_{line}\frac{di_o}{dt}=SV_d-v_g. \tag{3-1}$$

Solving for the current,

$$i_o(t)=i_o(t_0)+\int_0^t\frac{SV_d-v_g(\tau)}{L_{line}}d\tau, \tag{3-2}$$

where $i_o(t_0)$ is the value of the current at time t_0.

3.2.1.2 Simulation Model

The Hysteresis Control block is shown in Fig. 3-3. This block has four inputs and one output. The inputs are reference current i_{ref}, PV inverter current i_{PV}, the tolerance band h, and the fault signal generated by the UFP/OFP &UVP/OVP block. The output is

the switching pulses for the inverter switches. The measured real current i_{PV} is compared with the reference current high tolerance boundary $i_{ref}+h$ and the low reference boundary $i_{ref}-h$. The outputs of the Relational Operator blocks are connected to J-K Flip-Flop block. The Q terminal of the JKFF block generates the switching signal of the switches T_{A+} and T_{B-}. The switching signal of the switches T_{A-} and T_{B+} is obtained by adding a NOT Logical Operator block after Q terminal. The Data Type Conversion block is applied to convert signal type of the NOT gate output from boolean to double, required data type of the pulses for the inverter in Matlab Simulink. The Mux block multiplexes the matrix signals into a bus. An AND Logical Operator with the input fault single are added to the circuit to allow the shut-down of the inverter. If there is a fault signal, 0, the switching pulses will all be 0 and all the switches will be turned OFF, and the PV inverter will stop energizing the utility.

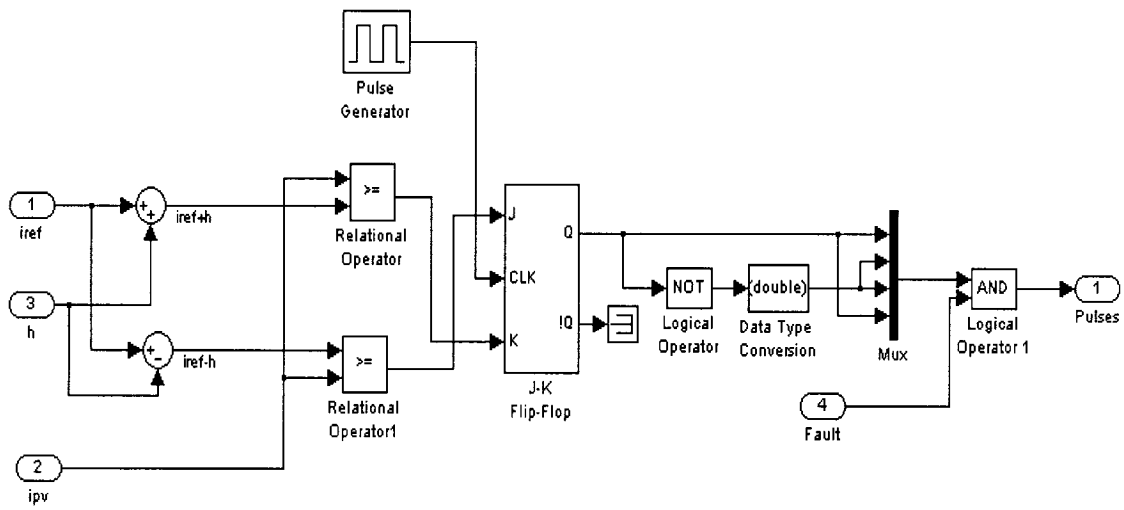

Fig. 3-3 Hysteresis Control block.

3.2.2 Frequency and RMS Block

The Frequency and RMS block measures the frequency and the RMS value of the PCC voltage, shown in Fig. 3-4. The Unit Delay block is used here to prevent the error of the ambiguous execution order due to use of subsystem in a loop during the simulation.

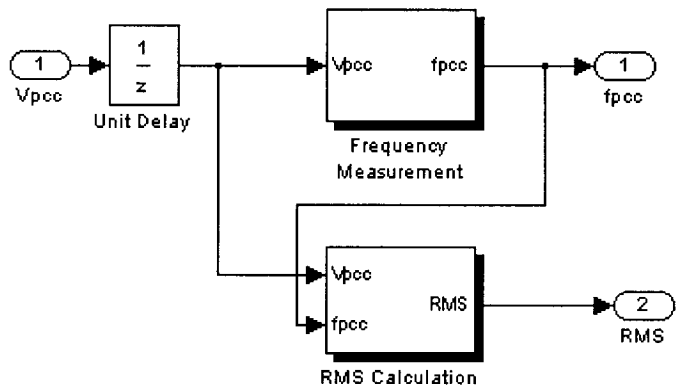

Fig. 3-4 Frequency and RMS block.

3.2.2.1 Frequency measurement

The operational frequency of a power system can be measured using the technique based upon the concept of zero crossings. One complete cycle is considered because this gives lower estimation errors. The measurement method is based upon counting the number of samples in one complete cycle (i.e. in an interval containing three adjacent zero crossings). The duration of one cycle of the power system waveform does not necessarily divide evenly (i.e. without remainder) over the sampling interval. The difference between the measured number of samples in one cycle and the exact figure could lead to errors in one cycle and in the estimated value of the frequency, unless this matter is handled properly. This problem can be overcome by applying a method to compute the effect of this difference on the estimate value of the frequency, thus enable us to obtain a very close estimate of the frequency in spite of this matter.

Consider the following sinusoidal waveform for the purpose of the measurement:

$$v(t) = V_m \sin \omega t, \tag{3-3}$$

where $\omega = 2\pi f$ is the angular frequency.

When working with sinusoidal signals, a convenient and useful parameter to be used is the number of samples per cycle of the waveform. Let this be denoted by N samples/cycle, and then it is related to the frequency f by

$$f = \frac{1}{NT_s}. \tag{3-4}$$

where T_s is the sampling interval.

The measurement method described is based on one complete cycle of the power signal sinusoidal waveform. Assume that the samples $y_{-1}, y_0, \ldots, y_k, y_{k+1}$ are the values of the sinusoidal waveform at the sampling time $t_{-1}, t_0, \cdots, t_k, t_{k+1}$ respectively as shown in Fig. 3-5. It is hereby assumed that the samples $y_0, \cdots, y_k$ are within interval of one complete cycle of the waveform, and that the two samples y_{-1}, y_{k+1} are outside this cycle.

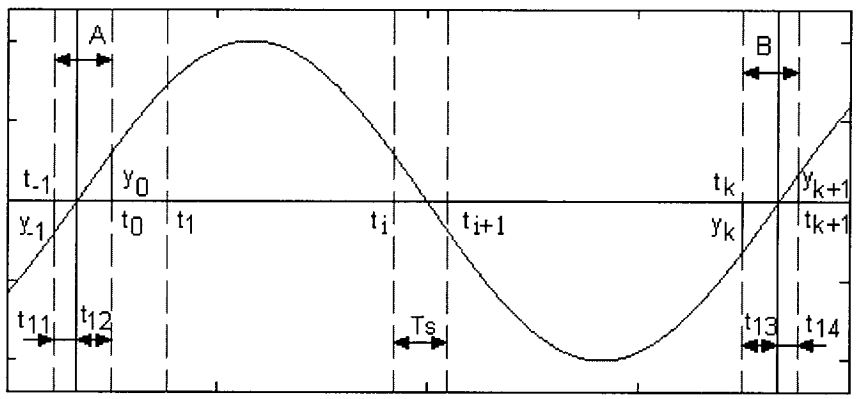

Fig. 3-5 Sine wave considered for measurement.

The frequency of the power signal will be estimated from Equation (3-4) mentioned above. In order to do that, value of N must be estimated, i.e., the number of samples in

one complete cycle of the waveform. The value of N will most likely not be an integer because this depends upon the sampling interval and the frequency to be measured. According to the notation in Fig. 3-5, the value of N is:

$$N = k + \frac{t_{12}}{T_s} + \frac{t_{13}}{T_s}, \tag{3-5}$$

where k is the integer number of sampling periods in one cycle.

Since the values of t_{12} and t_{13} are not available, the computation of the exact value of N is complicated. Notice that the values of the samples y_i are available, the value of N can be estimated as follows. The measurement starts either when a zero is encountered or when the signs of two samples alternate. The measurement is performed over an interval that includes one complete cycle of the waveform, as determined from the zero crossings. Following the notations in Fig. 3-5, and assuming that the sine function in the range of a zero crossing is approximated by a straight line, and using some trigonometric identities, the number of the stripes in one cycle can be approximately by:

$$N \cong k + k' = k + \frac{|y_0|}{|y_0| + |y_{-1}|} + \frac{|y_k|}{|y_k| + |y_{k+1}|}. \tag{3-6}$$

It should be noted that the same formula could be applied if $y_0 = 0$ (i.e. the measurement starts at a zero) $y_k = 0$ (i.e. the measurement ends at a zero). The value of the frequency is thus estimated by first computing N form Equation (3-6), and then using Equation (3-4) to estimate the value of the power frequency. It should be noted that the value of the frequency depends on the values of the two samples surrounding the first zero-crossing, the values of the two samples surrounding the last zero-crossing, the number of samples between these zero crossings (and not the values of the samples themselves), and the sampling interval.

3.2.2.2 Frequency measurement block

The Frequency Measurement block is shown in Fig. 3-6. Fig. 3-6(a) shows the main circuit to measure the frequency of PCC voltage, and Fig. 3-6(b), (c) and (d) shows the detail of the 3 subsystems of the main circuit. This block has one input PCC voltage v_{PCC} and one output frequency of the PCC voltage f_{PCC}. The Hit Crossing block compares the input signal to the hit crossing offset value, which is set as 0 here. If the input signal rises above the offset value, the block outputs 1, and Simulink takes a time step before and after the hit crossing time, which indicates the sampling interval, referred to the interval A or B in Fig. 3-5, when the default sample is larger than or equal to zero and the last sample is less than zero. The output of Hit Crossing activates the subsystem k', where the value $\frac{Y_k}{Y_k + Y_{k+1}}$ and $\frac{Y_{k+1}}{Y_k + Y_{k+1}}$ are calculated, as shown in Fig. 3-6(b). In this subsystem, the default value of the input signal is named Y_{k+1}, and the previous sample's value is named Y_k obtained by applying the Unit Delay block. After this interval, the subsystem Counter, shown in Fig. 3-6(d), starts to count the integer numbers of one cycle. The Enable and the Trigger blocks are placed to make this subsystem a enabled and triggered subsystem, and the Unit Delay used in this subsystem is used here to prevent the error of the ambiguous execution order due to use of subsystem in a loop during the simulation. The total integer number K_1 of one cycle and the value of $\frac{Y_{k+1}}{Y_k + Y_{k+1}}$ will be held in the subsystem Hold, shown in Fig. 3-6(c), and only update when Hold block is triggered by the Hit Crossing block output. Notice that $\frac{y_0}{y_0 + y_{-1}}$ in Equation (3-6), is obtained by applying a Unit Delay block to get the previous value of

$\frac{y_{k+1}}{y_k + y_{k+1}}$, when Hold block is triggered. Thus, the value $N = K_1 + K_2 + K_3$, thus the frequency of the last cycle can be obtained by Equation (3-4). The Switch is used here to set the initial value of the frequency as $60Hz$. It is worth noting that there is a Goto block in this circuit. This block send signal to From blocks that have the specified tag, which is CP here. The same signal will be used in another block, shown in Section 3.2.3.

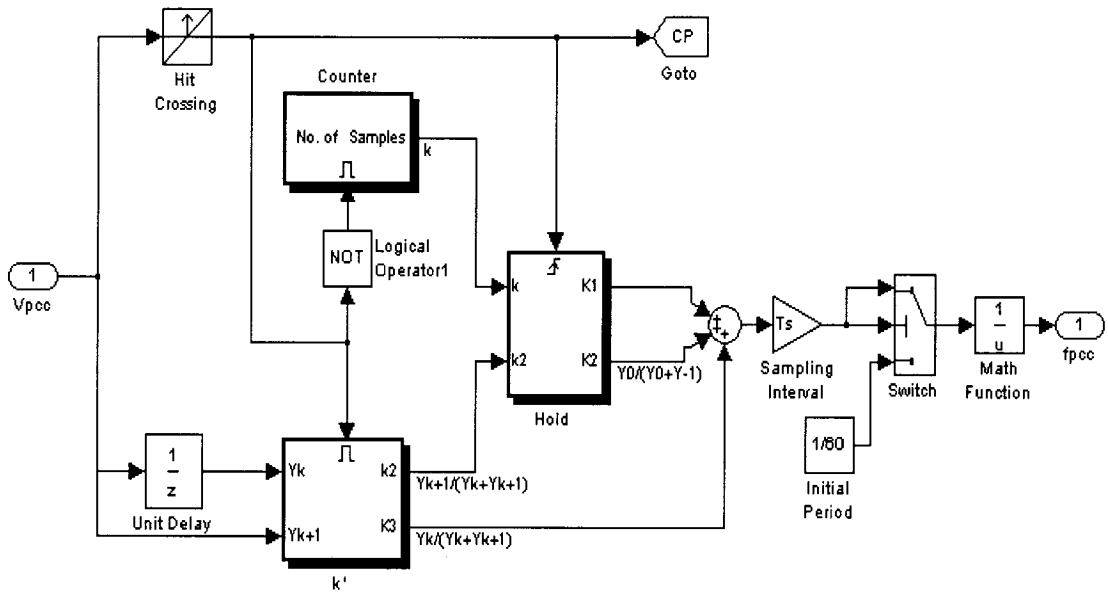

(a) Frequency measurement block main circuit

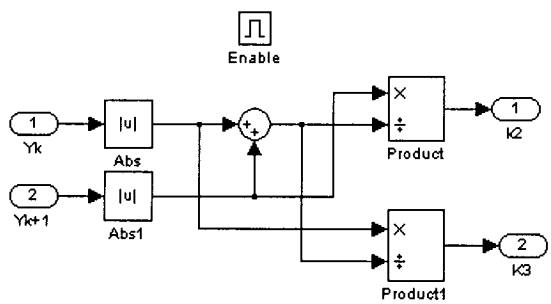

(b) k'

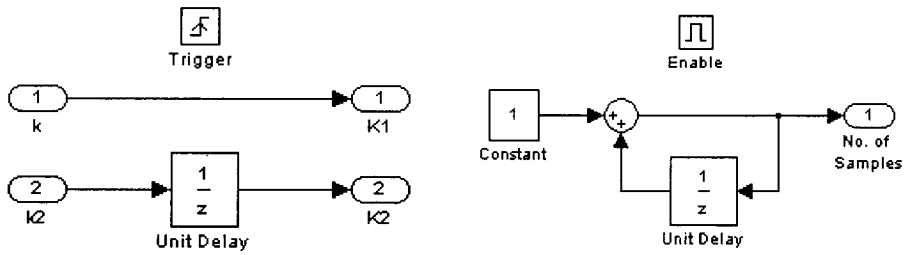

(c) Hold (d)Counter

Fig. 3-6 Frequency measurement block.

3.2.2.3 RMS value calculation block

The RMS Calculation block simply uses the definition of the RMS to calculate the magnitude of the voltage, shown in Fig. 3-7. The block Discrete Variable Frequency Mean Value is an existing block in Matlab Simulink. This discrete block computes the mean value of the input signal over a cycle of a specified frequency.

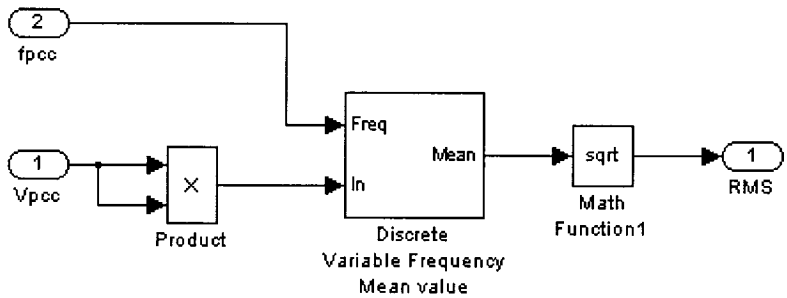

Fig. 3-7 RMS Calculation block.

3.2.3 UVP/OVP & UFP/OFP Block

The UVP/OVP & UFP/OFP block is shown in Fig. 3-8. The RMS value and the frequency of the PCC voltage are sent to the Voltage Thresholds and the Frequency Thresholds, shown in Fig. 3-9(a), (b) and (c). If the RMS value or the frequency exceeds the limits, the Voltage Thresholds or Frequency Thresholds blocks will output 1 to enable the Abnormal Voltage Cycles Counter or Abnormal Frequency Cycles Counter, shown in

Fig. 3-9(d) where the values of the cycles are different according to the Table 1. Then, the counter will be triggered by the raising edge of the output of the From block. The From block receives the signal from the Goto block with the specified tag, CP, which is described in Section 3.2.2.2, and outputs the same signal which represents the start of one cycle. Thus, the counter counts the cycles of the continuous abnormal voltage, and the counter will be reset if the voltage is back to normal. If the abnormal PCC voltage, either the RMS value or the frequency, continues for more cycles than the criteria of IEEE Std. 929-2000, shown in Table 1, the Resettable J-K Flip Flop, will be triggered, a low fault signal will be generated to turn off the inverter switches thereby ceasing the inverter to energize the utility. Since there is no existing block of Resettable J-K Flip Flop, the block is created using the logical operator, shown in Fig. 3-9(e). A Rd terminal is added to reset the JKFF when frequency and RMS value are back to normal again.

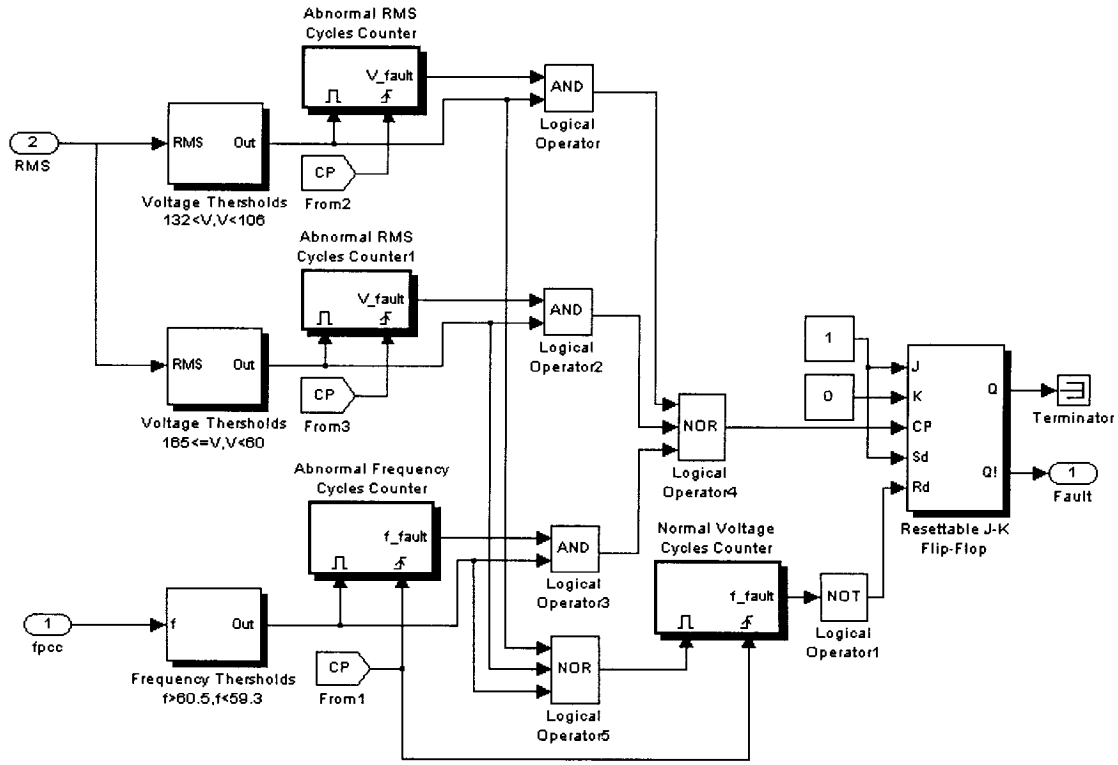

Fig. 3-8 UVP/OVP & UFP/OFP Block.

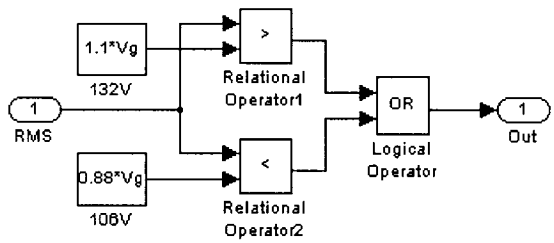

(a) Voltage thresholds $V > 132\,V$ or $V < 106\,V$

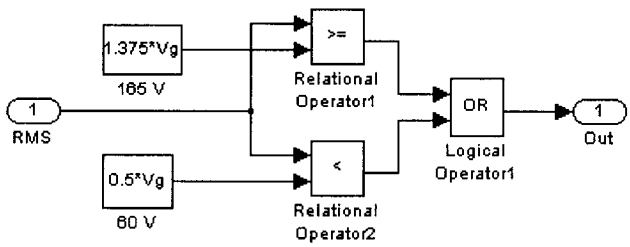

(b) Voltage thresholds $V \geq 165\,V$ or $V < 60\,V$.

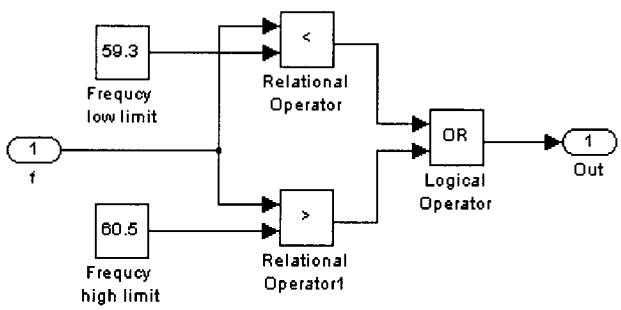

(c) Frequency thresholds $f > 60.5\,Hz$ or $f < 59.3\,Hz$

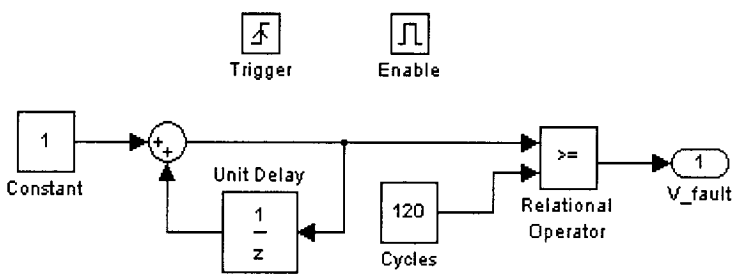

(d) Abnormal voltage/frequency cycles counter

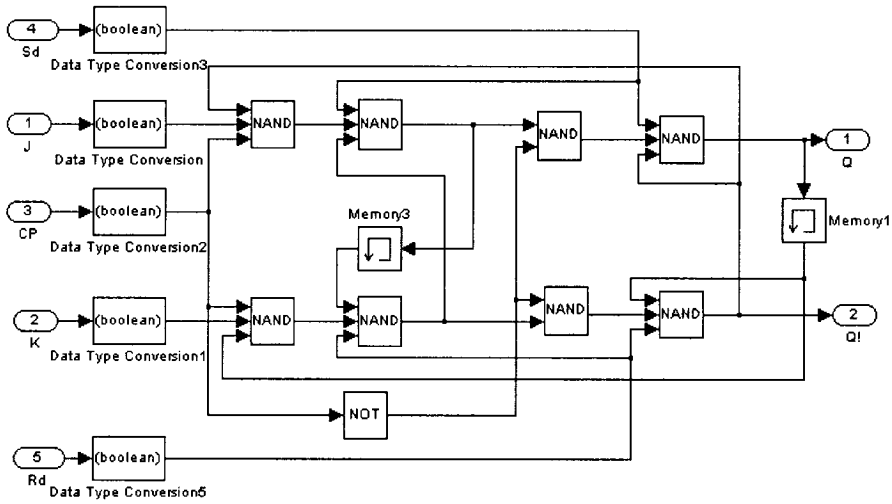

(e) Resettable J-K Flip-Flop

Fig. 3-9 Subsystems of the UVP/OVP &UFP/OFP block.

3.2.4 Reference Current with IDMs Block

Fig. 3-10 shows the Reference Current with IDMs block. The inputs of this block are the PCC voltage v_{PCC} and the frequency f_{PCC}. The outputs are the three reference currents of three active methods mentioned above: AFD, SMS and SFS.

3.2.4.1 AFD and SMS branches

The Hit crossing block generates a pulse lasting a sampling time at the each start of the source voltage waveform obtained from the voltage sensor. The time t, in the AFD and SMS branches is obtained by use of the block Discrete-Time Integrator to integrate the input signal 1 per cycle, but this time t is reset when a new cycle starts, i.e. the raising edge of the output of the Hit crossing block. The frequency of the voltage waveform f_{PCC} is from the output of the block Frequency and RMS.

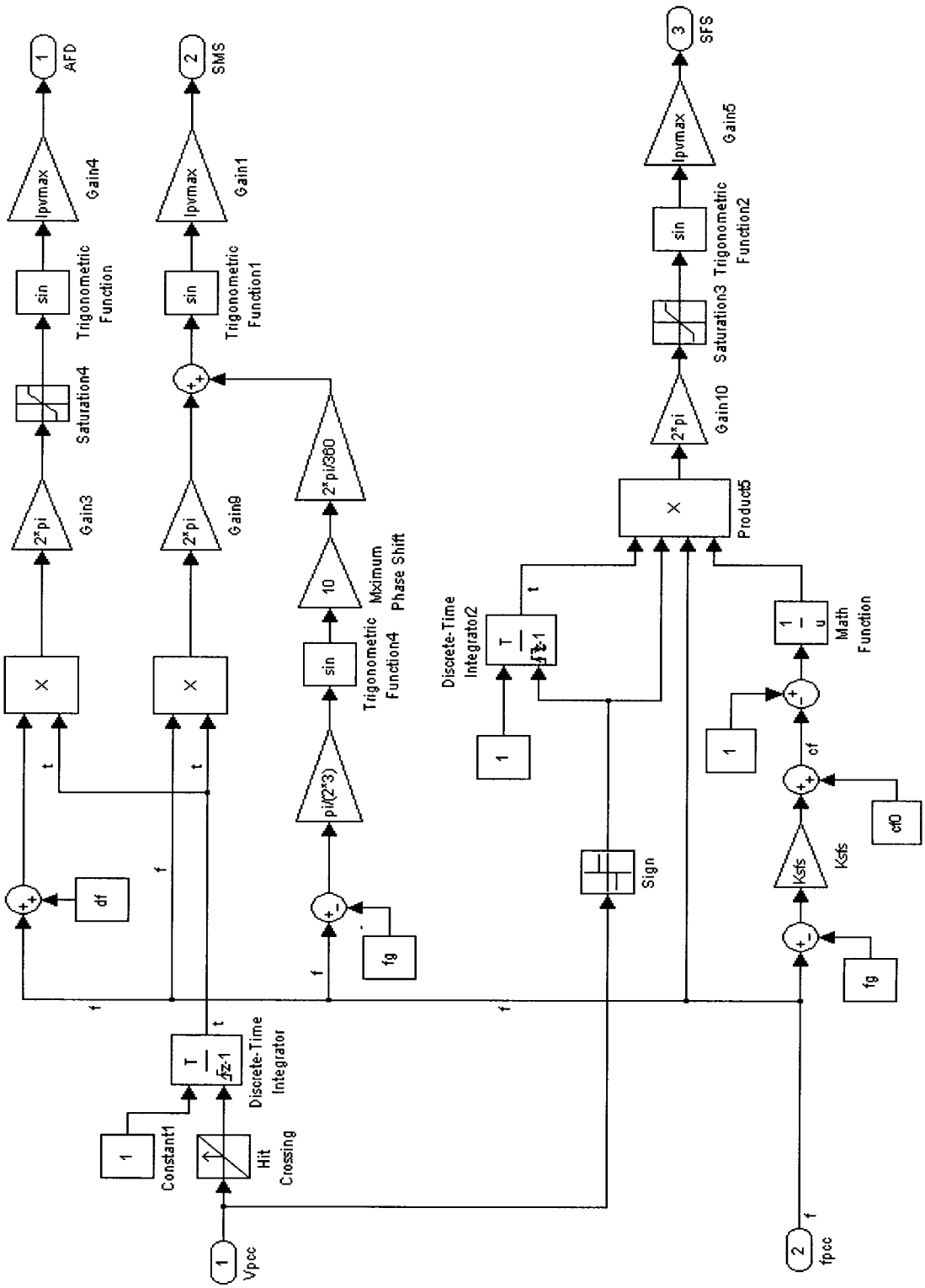

Fig. 3-10 Reference Current with IDMs Block.

For AFD, a fixed frequency drift df is added to the measured frequency of previous cycle of PCC voltage to obtain the current frequency $f_i = f_{PCC} + df$. The Saturation block in this branch is to limit the input signal upper and lower saturation values. In this case, the lower limit is set to be 0, and the upper limit is set to be 2π. If the value of $2\pi(f_{PCC} + df)t$ exceeds the upper limit, the Saturation block outputs the value 2π to create the zero current segment of the distorted AFD waveform, shown in Fig. 1-2. The distorted inverter output current of one cycle is

$$\begin{aligned} i_{AFD} &= I_{PV\max}\sin[2\pi(f_{PCC} + df)t], \quad when \quad 0 \le t \le T_i; \\ i_{AFD} &= 0, \qquad\qquad\qquad\qquad\quad when \quad T_i < t \le T_{PCC}. \end{aligned} \tag{3-7}$$

For SMS, an additional phase shift is added to the current cycle, and the value is $\theta_{SMS} = \frac{\pi}{2}\frac{f_{PCC} - f_g}{3}$. The PV system inverter with SMS output current is

$$i_{SMS} = I_{PV\max}\sin\left(2\pi f_{PCC} + \frac{2\pi}{360}\theta_{SMS}\right). \tag{3-8}$$

3.2.4.2 SFS branch

For SFS, the positive and the negative cycles are generated separately. By use of the block Sign to obtain the sign of the input signal, v_{PCC}. The block outputs signal 1 for $v_{PCC} > 0$, -1 for $v_{PCC} < 0$, and 0 for $v_{PCC} = 0$. A positive signal 1 will be apply to the positive cycle of the SFS current, and a negative signal -1 will be apply to the negative cycle of the SFS current. The time t for each half cycle in this branch is obtained by use of the block Discrete-Time Integrator to integrate the input signal 1 per cycle, but this time t is reset at the start of every half cycle, i.e. either the raising or falling edge of the output of the Sign block. According to Fig. 1-4, the period of the current first half sinusoidal cycle is

$$\begin{aligned}\frac{T_i}{2} &= \frac{T_{PCC}}{2} - t_z \\ &= \frac{T_{PCC}}{2}(1-cf),\end{aligned} \tag{3-9}$$

where $cf = \dfrac{2t_z}{T_{PCC}}$ is the chopping factor, t_z is the zero current time interval of the first half cycle. Thus, the frequency applied to the sinusoidal part of the current is

$$\begin{aligned}f_i &= \frac{1}{T_i} \\ &= \frac{f_{PCC}}{1-cf}.\end{aligned} \tag{3-10}$$

For SFS, the chopping factor $cf = cf_0 + k_{sfs}\left(f_{PCC} - f_g\right)$ is applied to every half current cycle, where k_{sfs} is the accelerate factor. Therefore, the sinusoidal part of the current is

$$\begin{aligned}i_{PV} &= I_{PV\max}\sin\left(2\pi f_i t\right) \\ &= I_{PV\max}\sin\left[2\pi\frac{f_{PCC}}{1-cf}t\right] \\ &= I_{PV\max}\sin\left[2\pi\frac{f_{PCC}}{1-cf_0-k_{sfs}\left(f_{PCC}-f_g\right)}t\right].\end{aligned} \tag{3-11}$$

The Saturation3 block in this branch is to limit the input signal in the range of $-\pi$ and π. If the value of $2\pi\dfrac{f_{PCC}}{1-cf_0-k_{sfs}\left(f_{PCC}-f_g\right)}t$ exceeds the upper limit, the Saturation3 block outputs the value π to create the zero current segment of the positive half cycle; and if the value of $2\pi\dfrac{f_{PCC}}{1-cf_0-k_{sfs}\left(f_{PCC}-f_g\right)}t$ exceeds the lower limit, the Saturation block outputs the value $-\pi$ to create the zero current segment of the negative half cycle. It is important to note that the zero time in the second half cycle is

not fixed and need not equal to t_z. Thus, at the positive half cycle, the inverter output current is

$$\begin{aligned} i_{SFS} &= I_{PV\max}\sin\left[2\pi\frac{f_{PCC}}{1-cf_0-k_{sfs}\left(f_{PCC}-f_g\right)}t\right], \quad when \quad 0\le t\le\frac{T_i}{2}; \\ i_{SFS} &= 0, \qquad\qquad\qquad\qquad\qquad\qquad when \quad \frac{T_i}{2}<t\le\frac{T_{PCC}}{2}. \end{aligned} \tag{3-12}$$

At the negative half cycle, the inverter output current is

$$\begin{aligned} i_{SFS} &= -I_{PV\max}\sin\left[2\pi\frac{f_{PCC}}{1-cf_0-k_{sfs}\left(f_{PCC}-f_g\right)}t\right], \quad when \quad 0\le t\le\frac{T_i}{2}; \\ i_{SFS} &= 0, \qquad\qquad\qquad\qquad\qquad\qquad when \quad \frac{T_i}{2}<t\le\frac{T_{PCC}}{2}. \end{aligned} \tag{3-12}$$

It is worth noting that when $k_{sfs}=0$, the SFS become the other type of AFD, mentioned in Section 1.4.1.

3.3 SIMULATION RESULTS AND ANALYSIS

Simulation was run for different islanding detection methods with different loads in order to verify the theoretical analysis for the NDZ in Q_f vs. f_0 space. It is worth noting that if the islanding is to occur, then the PCC voltage must remain within voltage limits when the utility is disconnected. Thus, the magnitude of the PV inverter reference current is set $I_{PV\max}=\frac{\sqrt{2}V_g}{R}$ for the simulation. The AFD IDM performance simulation is implemented for the frequency drift $\delta f=1Hz$ case, and the SMS IDM is implemented for the $\theta_m=10°$, $f_m-f_g=3Hz$ case, and the SFS IDM is implemented for the $cf_0=0.05$, $k_{sfs}=0.05$.

3.3.1 AFD IDM Simulation Result

3.3.1.1 AFD IDM simulation result

Fig. 3-11 shows the time domain response of the system with AFD IDM, voltage v_{PCC}, current i_{PV}, fault signal and the frequency f_{PCC}, when the grid breaker opens and the local load is $R = 14.4\,\Omega$ (corresponding to the $P_{load} = 1kW$ at $V_g = 120V$), $C = 460.52\,\mu F$ and $L = 15.28\,mH$, which gives the resonant frequency $f_0 = 60\,Hz$ and quality factor $Q_f = 2.5$. The grid breaker is set open, i.e. grid disconnected, at $t = 0.07083\,s$, the positive peak of the fifth cycle of the PCC voltage. From the waveform of the voltage, one can see that with the preset value of reference current $I_{PV\max} = \frac{\sqrt{2}V_g}{R} = 11.79\,A$, the magnitude of the voltage did not have apparent change before and after the grid disconnected. However, the frequency of the voltage f_{PCC} increased and exceeded the frequency upper limit the second cycle after the grid disconnected. It is worth mentioning that f_{PCC} shows the frequency of the last voltage cycle. The PV inverter stopped supplying the local load within 6 cycles after the frequency exceeded the frequency upper limits at $t = 0.1822\,s$ by turning off the inverter switches. One can see the PV current i_{PV} and the PCC voltage V_{PCC} all decreased to zero after the fault signal changed to 1. Thus, a load with $f_0 = 60\,Hz$ and $Q_f = 2.5$ lies outside the AFD NDZ for $\delta f = 1\,Hz$, which verifies the theoretical result.

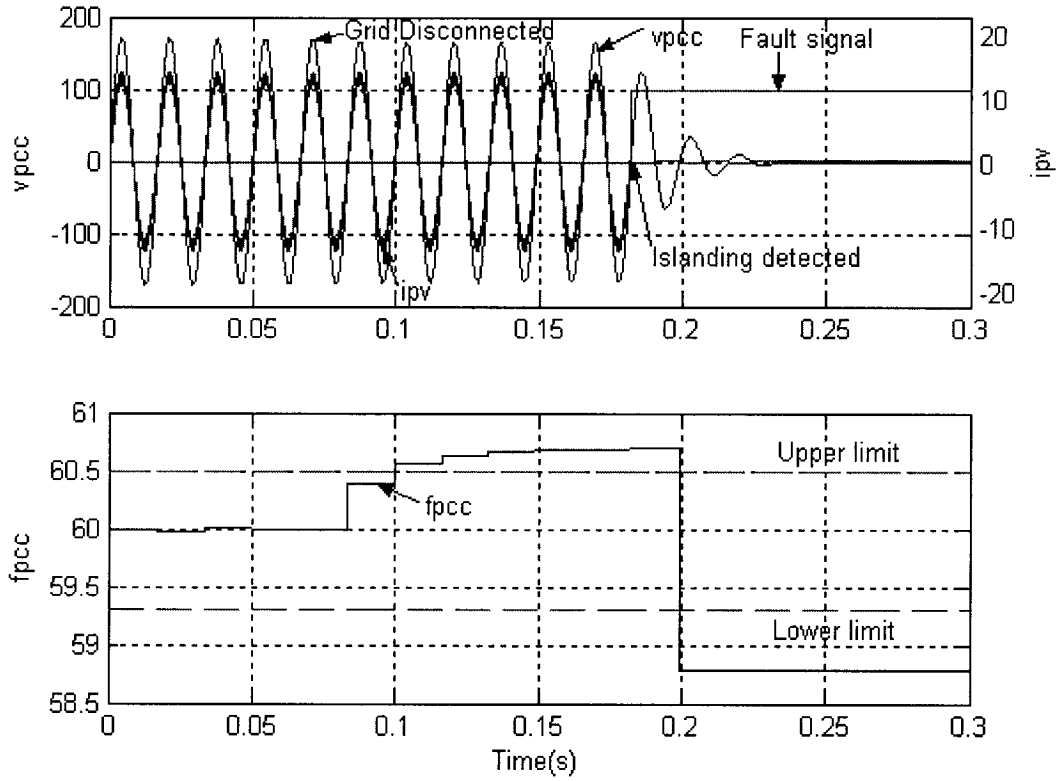

Fig. 3-11 Simulation result of AFD supplying a local load P_{load} = 1 *kW*, with f_0 = 60 *Hz* and Q_f = 2.5.

In order to verify that the NDZ in Q_f vs. f_0 space covers all different resistance values R, another simulation is implemented with the load, $R = 28.8\ \Omega$ (corresponding to the $P_{load} = 0.5kW$ at $V_g = 120V$), $C = 187.33\ \mu F$ and $L = 38.85\ mH$, which gives the resonant frequency $f_0 = 59\ Hz$ and quality factor $Q_f = 2$. Fig. 3-12 shows the time domain response of the system, voltage v_{PCC}, current i_{PV}, fault signal and the frequency f_{PCC}. The grid breaker is set open, i.e. grid disconnected, at $t = 0.07083s$. The magnitude of the reference current is set as $I_{PV\max} = \dfrac{\sqrt{2}V_g}{R} = 5.89A$ to maintain the magnitude of PCC voltage. The frequency of the voltage f_{PCC} decreased, however, reached a steady-state value within the frequency protection threshold. The fault signal remains 0. The undetectable islanding operation occurred, and the inverter continuously

supplies the load, shown in the PV current i_{PV} and the PCC voltage V_{PCC} waveform. Thus, a load with $f_0 = 59\,Hz$ and $Q_f = 2$ lies within the AFD NDZ for $\delta f = 1\,Hz$ as predicted from the theoretical analysis.

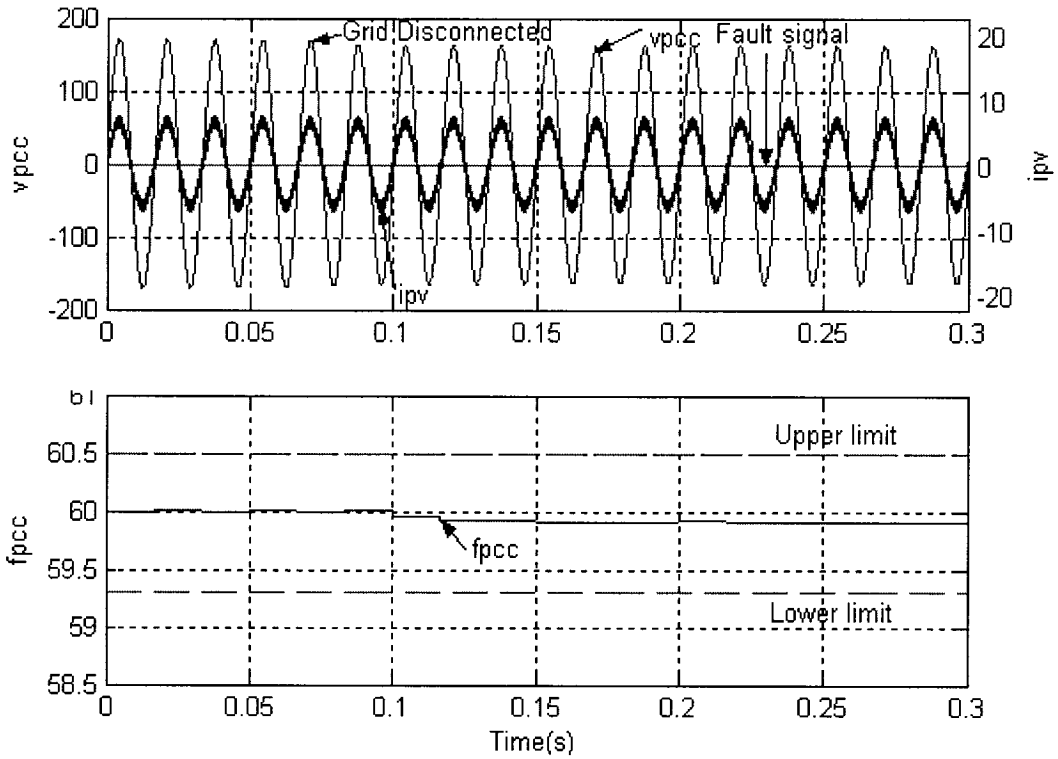

Fig. 3-12 Simulation result of AFD supplying a local load $P_{load} = 0.5\,kW$, with $f_0 = 69\,Hz$ and $Q_f = 2$.

Fig. 3-13 shows a comparison of the theoretical and simulated AFD NDZs under the condition $R = 14.4\,\Omega$. For the selected value of Q_f, the values of L and C were calculated to yield the selected Q_f and the f_0 which is close to the predicted boundary of the theoretical AFD NDZ corresponding to this Q_f. Ran the simulation with the chosen values of L and C, and repeated the simulation until the loads which lead to the critical islanding condition are found. Table 2 shows the data of the simulation results and the corresponding theoretical results.

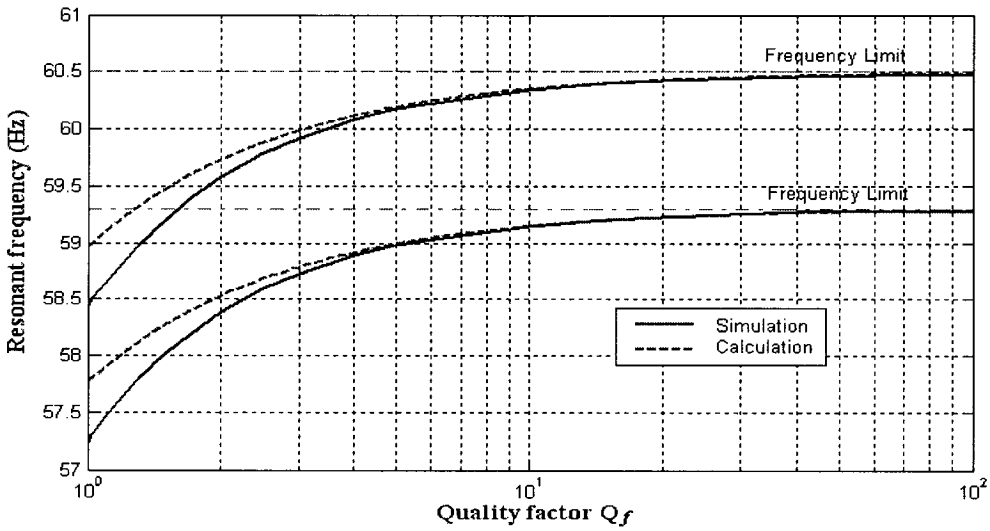

Fig. 3-13 Comparison of AFD NDZ of the simulated and theoretical results.

Table 2-Data of AFD NDZ of the simulated and theoretical results

Q_f	1	1.02	1.1	1.3	1.5	1.7	2	2.5	3	4
f_{0max_sim}	58.45	58.50	58.66	58.98	59.21	59.39	59.58	59.79	59.92	60.08
f_{0min_sim}	57.24	57.30	57.47	57.80	58.02	58.19	58.39	58.60	58.73	58.89
f_{0max_cal}	58.97	59.00	59.11	59.32	59.48	59.60	59.73	59.88	59.99	60.11
f_{0min_cal}	57.77	57.80	57.91	58.12	58.28	58.40	58.53	58.68	58.79	58.91
Q_f	5	10	15	20	40	60	100			
f_{0max_sim}	60.17	60.34	60.40	60.42	60.46	60.47	60.48			
f_{0min_sim}	58.98	59.15	59.20	59.27	59.27	59.28	59.29			
f_{0max_cal}	60.19	60.34	60.40	60.42	60.46	60.47	60.48			
f_{0min_cal}	58.99	59.15	59.20	59.22	59.26	59.27	59.28			

There one can see the agreement between the theoretical and simulation results is not very good for the loads with low quality factor. One possible reason is the formula used to calculate $\theta_{inv}(f)$. Recall that the injected current waveform is asymmetric which might cause distortion in PCC voltage v_{PCC}. This might lead to error when computing boundary f_0 using the phase criteria. To identify the error, we did simulation with loads in Table 2 for low quality factors $Q_f \leq 10$ case, where the error exists. The islanded system frequency f_{is} was measured during the islanding condition by setting the

Manual Switch in Fig. 3-1 to 1, i.e. deactivating the UVP/OVP UFP/OFP block, and then compared the error between the phase angles theoretical $\theta_{AFD}(f_{is})$ and $\theta_{load}(f_{is})$. The error is shown to decrease with Q_f increase in Fig. 3-14.

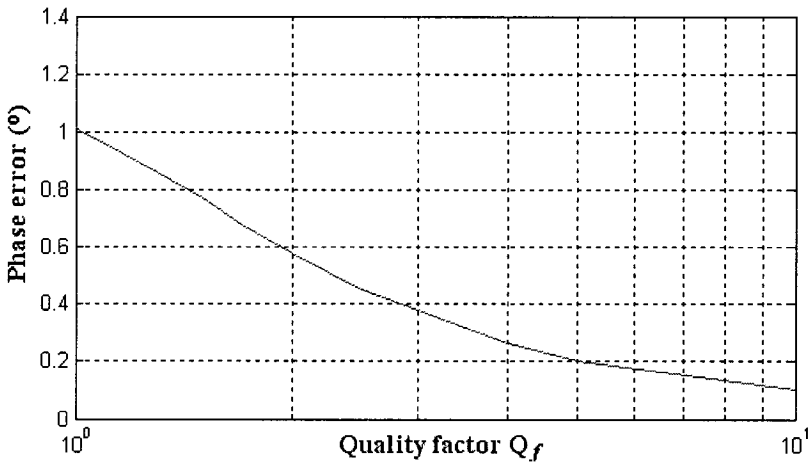

Fig. 3-14 Calculated phase error at low Q_f area.

The load phase angle error will lead to the significant error at the load quality factor Q_f, explained as follow. Fig. 2-3(a), the load frequency response, is enlarged and shown here again in Fig. 3-15. As shown in Fig. 3-15, the phase vs. frequency response curve of low Q_f load has smaller slope than that of the high Q_f load, and the slope of the phase frequency response increases as the load quality factor Q_f increases. For the large quality factor Q_f case, phase error only cause small frequency error. For example, for $Q_f = 5$, if there is $1°$ phase error, the frequency error is about $0.1Hz$. However, for the low quality factor Q_f case, the same phase error will cause much larger frequency error compared to the large quality factor load. Take $Q_f = 1$ case as an example. $1°$ phase error will cause more than $0.5Hz$ frequency error. Thus, the same phase error will cause a more severe error on the frequency of the system at the load quality factor Q_f than the large quality factor case, which results in the large deviation of the theoretical and the simulated result at the lower quality factor Q_f to the same level of phase error.

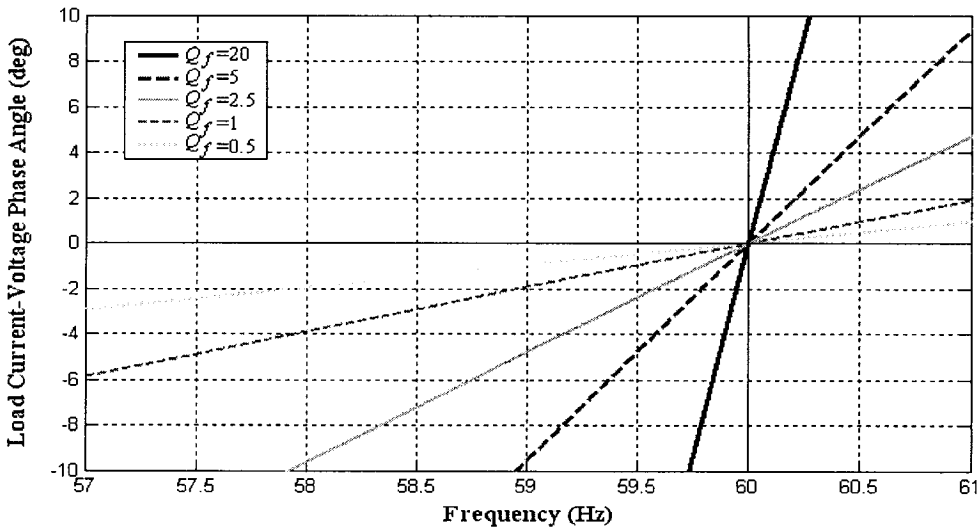

Fig. 3-15 *RLC* loads C-V phase angle vs. frequency characteristic.

3.3.1.2 Map AFD IDM NDZ by use of Laplace transform

The NDZ can be also obtained by the use of Laplace transform. Take the AFD as an example. For PV inverter with AFD IDM, output current waveform also can be expressed as

$$i_1(t) = I_{PV\max}\{\sin(2\pi f_i t) - \sin[2\pi f_i(t-T_i)]u(t-T_i)\}, \tag{3-13}$$

$$i(t) = i_1(t) + i_1(t-T)u(t-T) + i_1(t-2T)u(t-2T) + \cdots, \tag{3-14}$$

where $T_i = \frac{1}{f_i}$, and $T = \frac{1}{f_{PCC}}$.

Applying Laplace transform to Equation (3-13) and (3-14), one can obtain the current in the frequency domain as

$$I_1(s) = I_{PV\max}\left(\frac{\omega_i}{s^2+\omega_i^2} - e^{-T_i s}\frac{\omega_i}{s^2+\omega_i^2}\right) = I_{PV\max}\left(1-e^{-T_i s}\right)\frac{\omega_i}{s^2+\omega_i^2}, \tag{3-15}$$

$$I(s) = I_1(s) + I_1(s)e^{-Ts} + I_1(s)e^{-2Ts} + \cdots = I_1(s)\sum_{n=0}^{\infty} e^{-nTs}. \tag{3-16}$$

According to the series

$$\sum_{n=0}^{\infty} e^{-nTs} = \frac{1}{1-e^{-Ts}}, \tag{3-17}$$

one can get

$$\begin{aligned} I(s) &= \frac{1}{1-e^{-Ts}} I_1(s) \\ &= I_{PV\max} \frac{1-e^{-T_i s}}{1-e^{-Ts}} \frac{\omega_i}{s^2+\omega_i^2}. \end{aligned} \tag{3-18}$$

The parallel *RLC* load in frequency domain is

$$\begin{aligned} Z(s) &= \frac{1}{sC+\frac{1}{R}+\frac{1}{sL}} \\ &= \frac{R\omega_0}{Q_f} \frac{s}{\left(s+\frac{\omega_0}{2Q_f}\right)^2 + \left(\omega_0\sqrt{1-\frac{1}{4Q_f^2}}\right)^2}. \end{aligned} \tag{3-19}$$

Thus, the voltage of the parallel *RLC* load is

$$\begin{aligned} V(s) &= I(s)Z(s) \\ &= \frac{I_{PV\max} R\omega_0}{Q_f} \frac{1-e^{-T_i s}}{1-e^{-Ts}} \frac{\omega_i}{s^2+\omega_i^2} \frac{s}{\left(s+\frac{\omega_0}{2Q_f}\right)^2 + \left(\omega_0\sqrt{1-\frac{1}{4Q_f^2}}\right)^2}. \end{aligned} \tag{3-20}$$

The voltage in the time domain can be obtained by apply inverse Laplace transform, (the details of the calculation are shown in Appendix)

$$\begin{aligned} v(t) = {} & k_1 \sum_{n=0}^{\infty} \{\sin[b(t-nT)+\alpha]u(t-nT) - \sin[b(t-nT-T_i)+\alpha]u(t-nT-T_i)\} \\ & -k_2 \sum_{n=0}^{\infty} \{e^{-(t-nT)c} \sin[a(t-nT)+\beta]u(t-nT) - e^{-(t-nT-T_i)c} \sin[a(t-nT-T_i)+\beta]u(t-nT-T_i)\}, \end{aligned} \tag{3-21}$$

where

$$
\begin{aligned}
a &= \omega_0 \sqrt{1-\frac{1}{4Q_f{}^2}}, \\
b &= \omega_i, \\
c &= \frac{\omega_0}{2Q_f}, \\
\alpha &= \tan^{-1}\left[Q_f\left(\frac{\omega_0}{\omega_i}-\frac{\omega_i}{\omega_0}\right)\right], \\
\beta &= \tan^{-1}\left[\sqrt{4Q^2-1}\,\frac{\omega_0{}^2-\omega_i{}^2}{\omega_0{}^2+\omega_i{}^2}\right], \\
k_1 &= \frac{I_{PV\max}R}{\sqrt{1+Q_f{}^2\left(\frac{\omega_0}{\omega_i}-\frac{\omega_i}{\omega_0}\right)^2}}, \\
k_2 &= I_{PV\max}R\frac{\sqrt{Q_f{}^2\left(\frac{\omega_0}{\omega_i}-\frac{\omega_i}{\omega_0}\right)^2+\frac{Q_f{}^2}{4Q_f{}^2-1}\left(\frac{\omega_0}{\omega_i}+\frac{\omega_i}{\omega_0}\right)^2}}{1+Q_f{}^2\left(\frac{\omega_0}{\omega_i}-\frac{\omega_i}{\omega_0}\right)^2}.
\end{aligned}
\tag{3-22}
$$

The actual voltage waveform can be obtained according to Equation (3-21). The approach for obtaining the upper boundary of the NDZ for AFD in the Q_f vs. f_0 space is as follows. For a selected value of Q_f and $\omega_0 = 2\pi f_0$, computed $\omega_{i\max} = 2\pi(f_{\max} + \delta f)$ and $\omega_{i\min} = 2\pi(f_{\min} + \delta f)$ and calculated (3-21) for $T_{\max} = 1/f_{\max}$ and $T_{\min} = 1/f_{\min}$. The values of Q_f and f_0 are at the upper and lower boundary of the NDZ when $v(T_{\max}) \approx 0$ and $v(T_{\min}) \approx 0$.

Fig. 3-16 shows the AFD NDZ mapped by Laplace transform for $\delta f = 1Hz$ compared with the NDZ mapped with Equation (2-38) and the simulation result. From Fig. 3-16, one can see that the NDZ mapped by the Laplace transform is close to the simulation result, also verified the simulation result. However, the result obtained by applying Laplace transform is much more complicated and time-consuming.

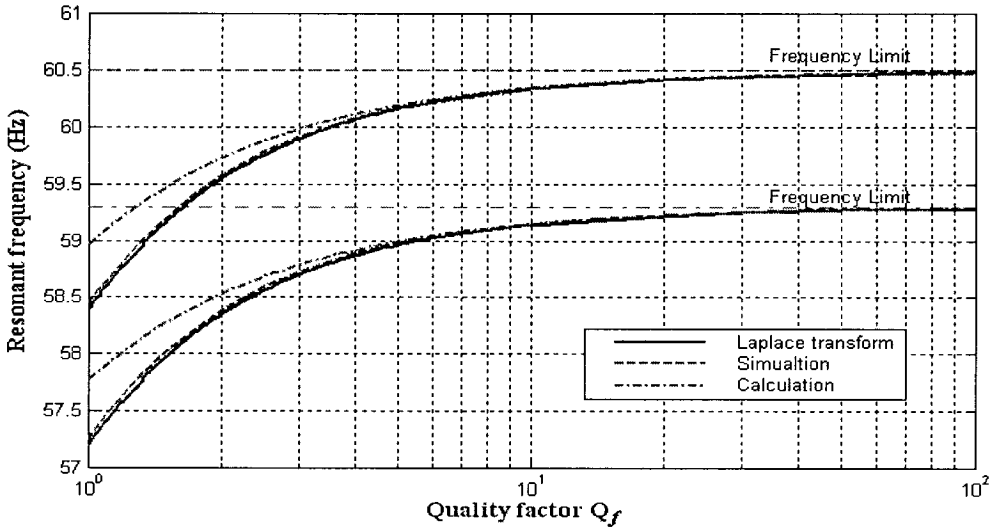

Fig. 3-16 NDZs mapped by Laplace transform compared with simulation and calculation results.

3.3.2 SMS IDM Simulation Result

Similar tests were run for the grid connected inverter using the SMS IDM with $\theta_m = 10°$ and $f_m - f_g = 3\ Hz$. Fig. 3-17 shows the time domain response of the system with SMS IDM , voltage v_{PCC}, current i_{PV}, fault signal and the frequency f_{PCC}, when the grid breaker opens and the local load is $R = 14.4\ \Omega$ (corresponding to the $P_{load} = 1kW$ at $V_g = 120V$), $C = 460.52\ \mu F$ and $L = 15.28\ mH$, which gives the resonant frequency $f_0 = 60\ Hz$ and quality factor $Q_f = 2.5$. The grid breaker is set open, i.e. grid disconnected, at $t = 0.07083 s$, the positive peak of the fifth cycle of the PCC voltage. The frequency of the voltage f_{PCC} decreased and became lower than the UFP set point after the grid disconnected. The PV inverter stopped supplying the local load within 6 cycles after the frequency exceeded the frequency lower limits at $t = 0.4027 s$ by turning off the inverter switches. One can see the PV current i_{PV} and the PCC voltage V_{PCC} all decreased to zero after the fault signal changed to 1. Thus, a

load with $f_0 = 60\,Hz$ and $Q_f = 2.5$ lies outside the SMS NDZ for $\theta_m = 10°$, which verifies the calculation results.

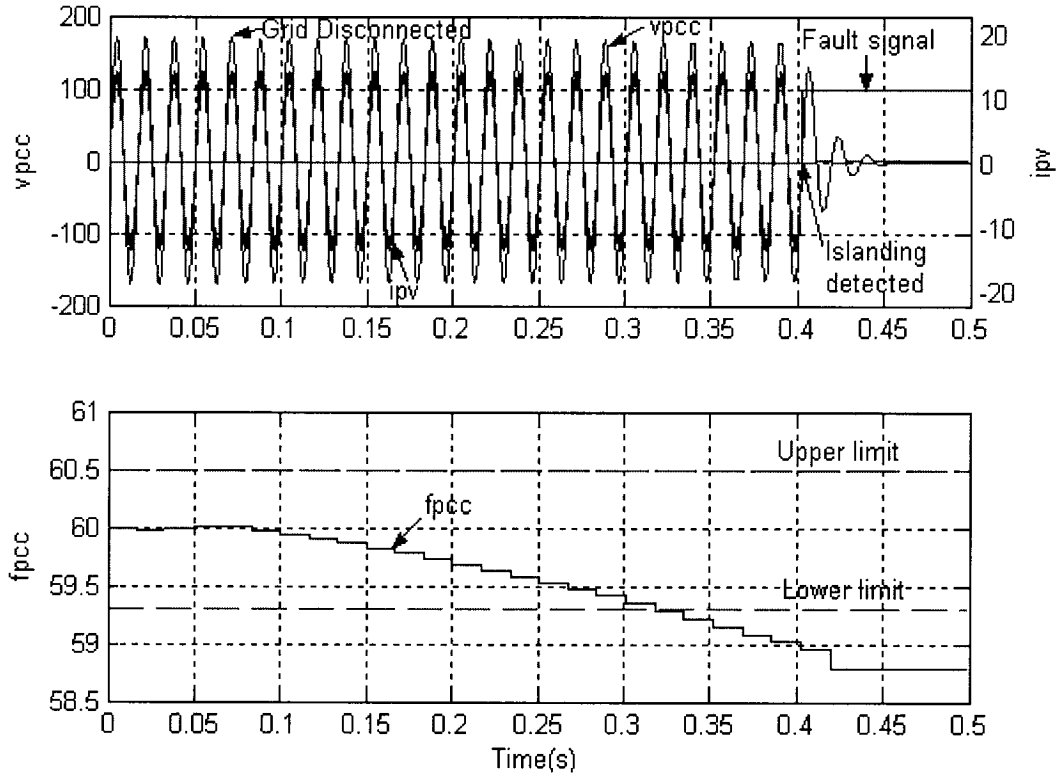

Fig. 3-17 Simulation result of SMS supplying a local load P_{load} = 1 *kW*, with f_0 = 60 Hz and Q_f = 2.5.

Another simulation is implemented with the load, $C = 552.62\,\mu F$ and $L = 12.73\,mH$, which gives the resonant frequency $f_0 = 60\,Hz$ and quality factor $Q_f = 3$. Fig. 3-18 shows the time domain response of the system, voltage v_{PCC}, current i_{PV}, fault signal and the frequency f_{PCC}. The grid breaker is set open, i.e. grid disconnected, at $t = 0.07083\,s$. After grid disconnected, the frequency of the voltage f_{PCC} decreased, however, reached the steady-state within the frequency protection threshold. The fault signal remains 0. The undetectable islanding operation occurred, and the inverter continuously supplies the load, shown in the PV current i_{PV} and the PCC

voltage V_{PCC} waveform. Thus, a load with $f_0 = 60\,Hz$ and $Q_f = 3$ lies within the SMS NDZ for $\theta_m = 10°$ as predicted from the theoretical analysis.

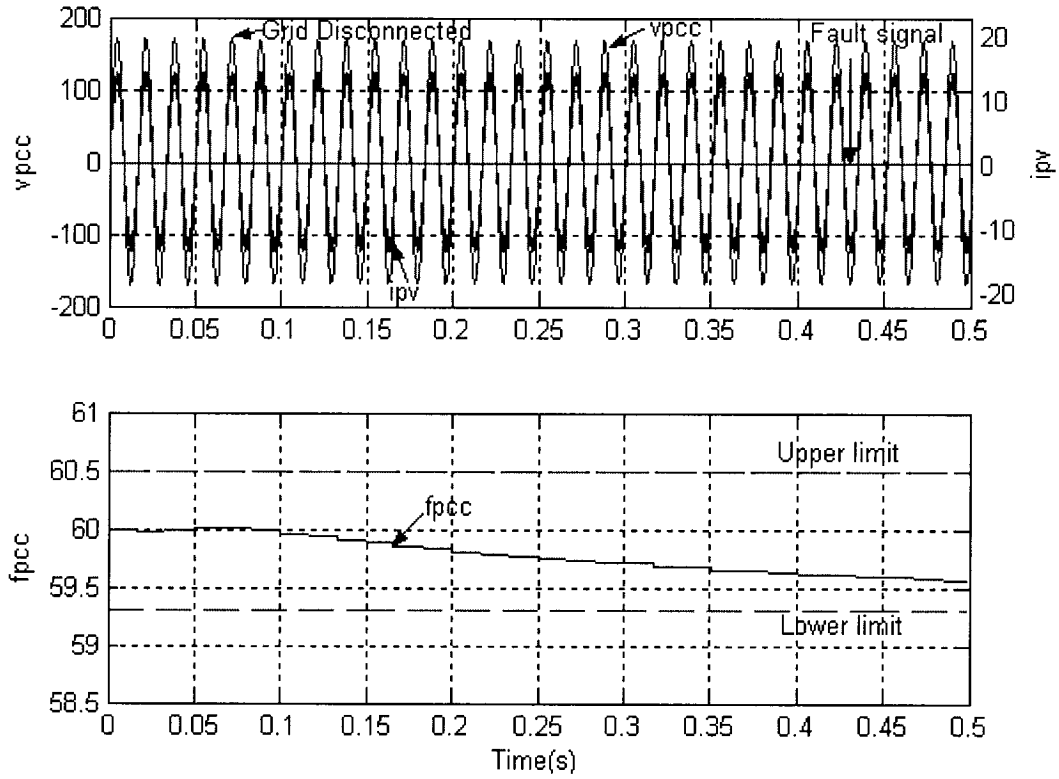

Fig. 3-18 Simulation result of SMS supplying a local load P_{load} = 1 *kW*, with f_0 = 60 Hz and Q_f = 3.

Fig. 3-19 shows a comparison of the theoretical and simulated SMS NDZs. Table 3 shows the data of the simulation results and the corresponding theoretical results. The Fig.3-19 and the Table 3 show that the agreements between the simulation and theoretical results are very good. One can see from the simulation result that there is no NDZ in the area $Q_f < 2.5$ as predicted.

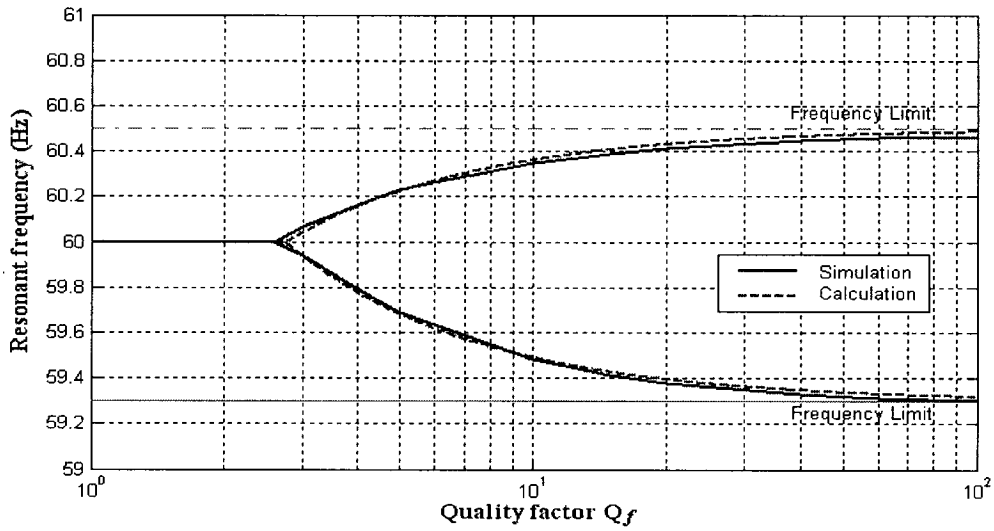

Fig. 3-19 Comparison of SMS NDZ of the simulation and calculation.

Table 3-Data of SMS NDZ of the simulation and calculation result

Q_f	1	2	2.5	2.7	3	4	5	10	15	20
f_{0max_sim}	-	-	-	60.00	60.07	60.16	60.23	60.35	60.39	60.41
f_{0min_sim}	-	-	-	60.00	59.94	59.79	59.69	59.48	59.41	59.38
f_{0max_cal}	60.00	60.00	60.00	60.00	60.04	60.16	60.23	60.36	60.41	60.43
f_{0min_cal}	60.00	60.00	60.00	59.99	59.92	59.77	59.67	59.49	59.42	59.39
Q_f	40	60	100							
f_{0max_sim}	60.45	60.46	60.46							
f_{0min_sim}	59.33	59.31	59.30							
f_{0max_cal}	60.47	60.48	60.49							
f_{0min_cal}	59.33	59.32	59.31							

3.3.3 SFS IDM Simulation Result

Similar tests were run for the grid connected inverter using the SFS IDM with $cf_0 = 0.05$ and $k_{sfs} = 0.05$. Fig. 3-20 shows the time domain response of the system with SFS IDM , voltage v_{PCC}, current i_{PV}, fault signal and the frequency f_{PCC}, when the grid breaker opens and the local load is $R = 14.4\,\Omega$ (corresponding to the $P_{load} = 1kW$ at $V_g = 120V$), $C = 460.52\,\mu F$ and $L = 15.28\,mH$, which gives the resonant frequency $f_0 = 60\,Hz$ and quality factor $Q_f = 2.5$. The grid breaker is set

open, i.e. grid disconnected, at $t = 0.07083s$, the positive peak of the fifth cycle of the PCC voltage. The frequency of the voltage f_{PCC} increased and exceeded the frequency lower limit after the grid disconnected. The PV inverter stopped supplying the local load within 6 cycles after the frequency exceeded the frequency upper limit at $t = 0.1626s$ by turning off the inverter switches. One can see the PV current i_{PV} and the PCC voltage V_{PCC} all decreased to zero after the fault signal changed to 1. Thus, a load with $f_0 = 60\,Hz$ and $Q_f = 2.5$ lies outside the SFS NDZ for $cf_0 = 0.05$ and $k_{sfs} = 0.05$, which verifies the calculation results.

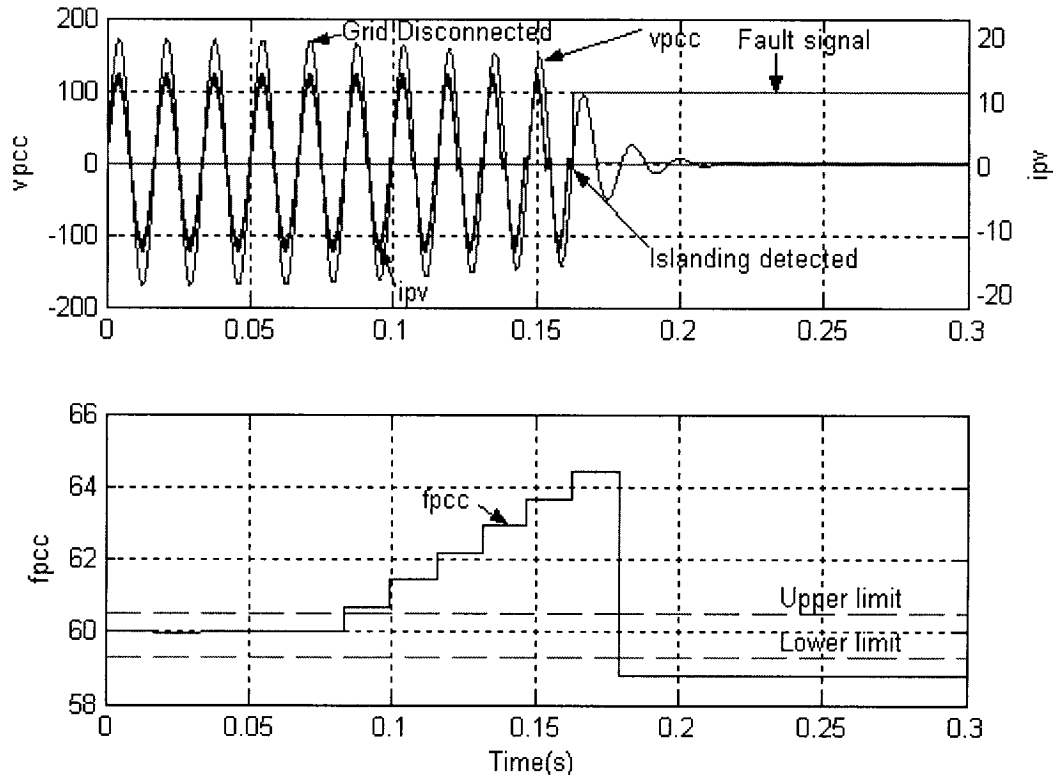

Fig. 3-20 Simulation result of SFS supplying a local load $P_{load} = 1\ kW$, with $f_0 = 60$ Hz and $Q_f = 2.5$.

Another simulation is implemented with the load, $C = 561.04\,\mu F$ and $L = 12.93\,mH$, which gives the resonant frequency $f_0 = 59.1\,Hz$ and quality factor

$Q_f = 3$. Fig. 3-21 shows the time domain response of the system, voltage v_{PCC}, current i_{PV}, fault signal and the frequency f_{PCC}. The grid breaker is set open, i.e. grid disconnected, at $t = 0.07083 s$. After grid disconnection, the frequency of the voltage f_{PCC} decreased, however, reached the steady-state within the frequency protection threshold. The fault signal remains 0. The undetectable islanding operation occurred, and the inverter continuously supplies the load, shown in the PV current i_{PV} and the PCC voltage V_{PCC} waveform. Thus, a load with $f_0 = 59.1\,Hz$ and $Q_f = 3$ lies within the SFS NDZ for $cf_0 = 0.05$ and $k_{sfs} = 0.05$ as predicted from the theoretical analysis.

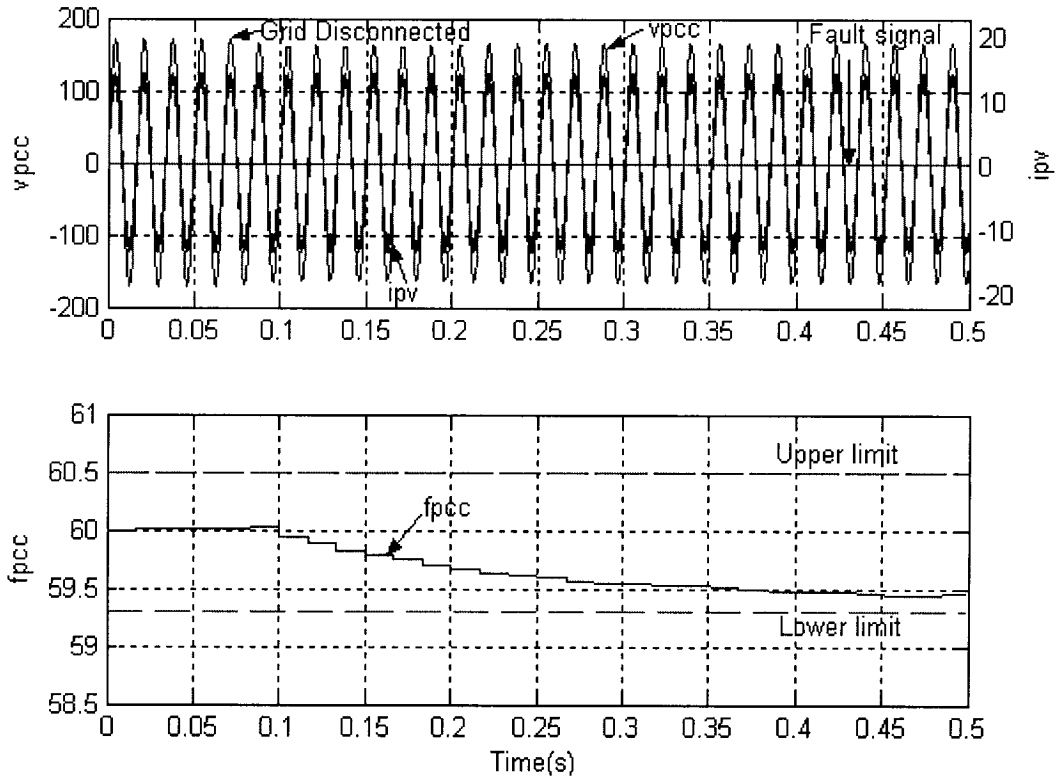

Fig. 3-21 Simulation result of SFS supplying a local load $P_{load} = 1\ kW$, with $f_0 = 59.1$ Hz and $Q_f = 3$.

Fig. 3-22 shows a comparison of the theoretical and simulated SFS NDZs. Table 4 shows the data of the simulation results and the corresponding theoretical results. The

Fig.3-22 and the Table 4 show that the agreements between the simulation and theoretical results are very good. In simulation, the low quality factor area, $Q_f < 2.5$, does not have NDZ.

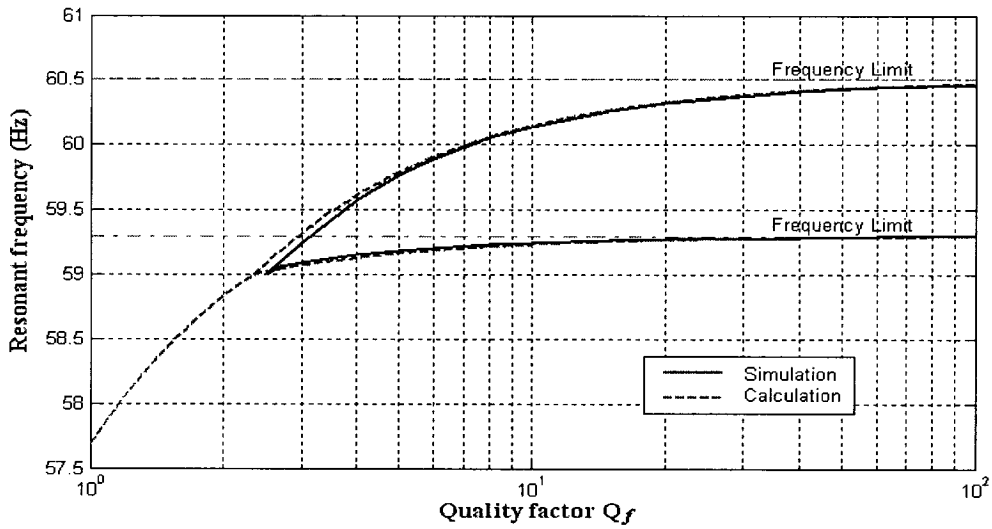

Fig. 3-22 Comparison of SFS NDZ of the simulation and calculation.

Table 4-Data of SFS NDZ of the simulation and calculation result

Q_f	1	1.1	1.5	2	2.2	2.5	2.7	3	4	5
f_{0max_sim}	-	-	-	-	-	59.00	59.10	59.25	59.59	59.77
f_{0min_sim}	-	-	-	-	-	59.00	59.06	59.09	59.15	59.18
f_{0max_cal}	57.69	57.89	58.45	58.83	58.94	59.08	59.19	59.32	59.62	59.79
f_{0min_cal}	57.69	57.89	58.45	58.83	58.94	59.02	59.04	59.07	59.13	59.16
Q_f	6	8	10	15	20	40	60	100		
f_{0max_sim}	59.89	60.05	60.14	60.26	60.32	60.41	60.44	60.46		
f_{0min_sim}	59.20	59.23	59.25	59.27	59.28	59.29	69.30	59.30		
f_{0max_cal}	59.91	60.06	60.14	60.26	60.32	60.41	60.44	60.46		
f_{0min_cal}	59.18	59.21	59.23	59.25	59.27	59.28	59.29	59.29		

3.4 CONCLUSION

The validation of the theoretical analysis and equations that describe the NDZ of three common active IDMs in the proposed Q_f vs. f_0 space was performed with simulation. The grid-connected PV system has been modeled and simulated by the use of

Matlab Simulink. The components of the model, such as blocks Hysteresis Control, Frequency and RMS, and Reference Current with IDMs, have been described in detail. The simulation of different IDMs, including AFD, SMS and SFS, with loads of different resonant frequency and quality factor has been run to verify the theoretical analysis. The simulation results of NDZ of these three IDMs have been mapped to compare with the theoretical results. The agreements between the theoretical results and simulation results are good in most of the loads. The error between the theoretical results and simulation results of AFD NDZ has been discussed, and the NDZ mapped by the use of Laplace transform shows good agreement with the simulation results.

CHAPTER 4
EXPERIMENTAL VERIFICATION

4.1 INTRODUCTION

This Chapter presents details of a small scale laboratory prototype that was implemented to validate the simulation results discussed in the previous chapter and to identify difficulties that can arise in a practical system. Section 4.2 describes the experimental set-up with details of the power converter and the control scheme used to implement the islanding detection methods. Section 4.3 presents the experimental results obtained for the three Islanding detection methods (IDM), AFD, SMS and SFS. Conclusions are stated in Section 4.4.

4.2 EXPERIMENTAL SETUP

Fig. 4-1 depicts the laboratory set-up used to obtain the experimental results. The single-phase full bridge inverter is implemented with an IGBT module (CM50MD-12H, POWEREX). The gating signals generated by the digital signal processor (DSP) system, to be described later, are amplified and isolated by a gate drive system composed of isolated DC-to-DC converter (M57140-01, POWEREX) and gate drive (M57962L, POWEREX).

At the ac side one sees a $5mH$ inductor used to connect the inverter to the PCC where one sees the *RLC* local load, the ac grid breaker and a single-phase $5kVA$ VARIAC (variable autotransformer) used to represent the ac grid. A Hall effect current sensor (LA55-P, LEM) is used to monitor the ac current of the inverter and provide a feedback signal so that the hysteresis control can regulate this current. An ac voltage sensor (LV100, LEM) is employed to monitor the PCC voltage. It provides synchronism for the reference

current of the inverter and allows the measurement of the frequency and magnitude of the voltage at the PCC.

At the dc side of the inverter there is a solar array simulator (E-43508, Agilent) operating in the constant voltage mode to emulate the dc-dc maximum power point tracking (MPPT) converter and the PV array. A $600\,\mu F$ dc bus capacitor is connected the output of the solar simulator. Usually a dc bus voltage regulating loop is included in a system like this to control the active power the inverter injects into the ac grid under transient conditions. However, since the worst case for islanding detection is when there is no variation of the power generated by the PV source and consumed by the local load, this feedback loop is omitted in this study. Thus the PV source is assumed to supply constant power and the inverter injects constant current. The maximum output voltage for the PV array simulator is 60 V. Thus we have chosen to fix the dc bus voltage of the inverter at 55 V and the ac grid voltage, via the VARIAC, at 30 V rms. It is worth mentioning that the dc bus voltage of the inverter has to be higher than the peak value of the ac grid voltage for full control of the power flow.

A digital signal processor (DSP) development kit (DS-1103, dSPACE) was employed to implement the control circuit of the inverter with the IDMs, including AFD, SMS and SFS.

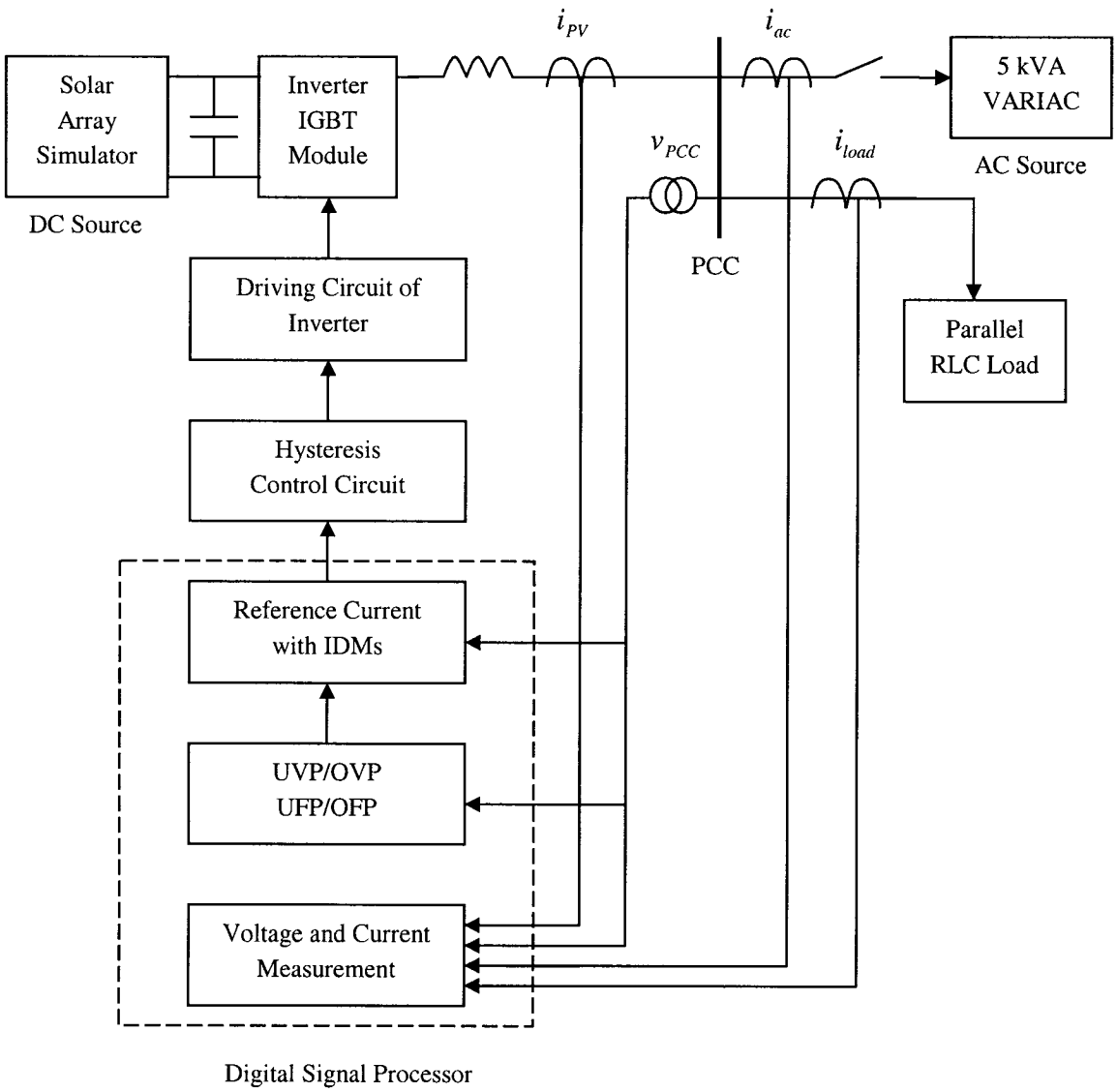

Fig. 4-1 Laboratory set-up used in the experiments.

4.2.1 dSPACE DSP system

The dSPACE system is commonly used for rapid prototyping of electrical control systems and is comprised of a DS1103 PPC controller board. It is equipped with a Motorola PowerPC 604e processor, whose computing power allows for the simulation of large-scale floating-point control algorithms in real-time. A full range of I/O devices including a TMS320F240 slave DSP is available on-board. Using the Real-Time Interface

to Simulink, automatic code generation from block diagrams is possible. I/O functions are specified graphically as part of the simulation model. Therefore, the migration from MATLAB Simulink to practical control of an external plant can be easily done by the inclusion of I/O blocks in the control circuits.

4.2.1.1 Hardware Architecture

The DS1103 PPC Controller Board is equipped with a Motorola PowerPC 604e processor for fast floating-point calculation at 333MHz. This high-performance superscalar microprocessor has three integer execution units, one floating-point arithmetic unit, and a separate load/store unit for fast memory access. The on-chip cache size is 32kByte for instruction and data. The processor's ability to execute instructions out-of-order leads to a performance improvement of about factor 2 for typical simulation models compared to strictly serial instruction flow.

A 2MByte local memory is used for program and data of the simulation model. The local memory is fully cached and cannot be accessed by the host PC in standard operation mode. For data buffering and exchange between PowerPC and the host, up to 128 MByte of non-cached global memory is available. The host interface of the board is used to perform board setups, program downloads, and runtime data transfer. It supports Plug & Play functionality for easy installation.

The board can be adapted to a wide range of closed-loop applications due to its large number of I/O devices. High-resolution A/D converters (16-bits and 12 bits) with a sampling time of 4us and 800 ns, respectively, are available, as well as D/A output channels with a resolution of 14-bit and a 5 us settling time. 32 digital I/O channels and a serial line interface complete the list of standard I/O units.

4.2.1.2 Real-Time Interface to Simulink

Using MATLAB and Simulink for modeling, analysis, design and offline simulation has become a de-facto standard for control system development. The Real-Time Interface enhances the Simulink block library with additional blocks, which provide the link between Simulink and the real-time hardware, as shown in Fig. 4-2. To graphically specify an I/O channel the corresponding block icon has to be picked up from the I/O block library and attached to the Simulink controller model. I/O parameters, such as voltage ranges or resolutions, can be set in appropriate dialog boxes. The Simulink model then is transferred into real-time code, using the Real-Time Workshop, state flow control, and the Real-Time Interface. Code generation includes the I/O channel specification and the multitasking setup, which are translated into appropriate function calls of the Real-Time Library. The library is a C function library providing a high-level programming interface to the hardware. The Real-Time Library also includes access functions for the slave DSP. These blocks cover the I/O functionality of the prototyping hardware.

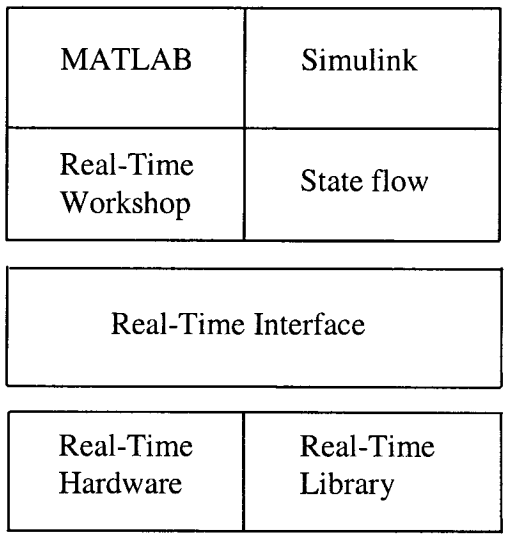

Fig. 4-2 The Real-Time Interface in the MATLAB/Simulink environment.

4.2.1.3 Simulink Block Library for DS1103

The block library for the DS1103 PowerPC Controller Board is subdivided into two major parts according to the two microprocessor units on the board. The library shown in Fig. 4.3 comprises all I/O units that are directly served by the PowerPC master processor. Block icons for the standard I/O channels such as A/D, D/A converters, and digital I/O are included as well as the more complex incremental encoder blocks.

The slave DSP library, shown in Fig. 4-4, offers frequently used functions of the TMS320F240, such as single-phase and three-phase PWM signal generation, frequency measurement, A/D conversion, and digital I/O. Because the real-time simulation is executed in the master PPC board, it is wished to employ the functions provided by the slave DSP as much as possible to save the computation time on the Master PPC board.

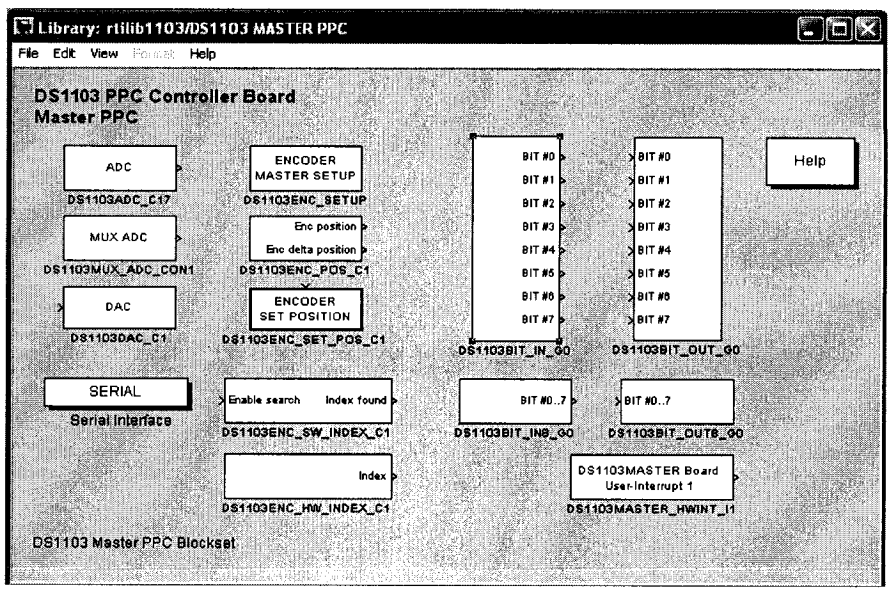

Fig. 4-3 Master Processor block library for Simulink.

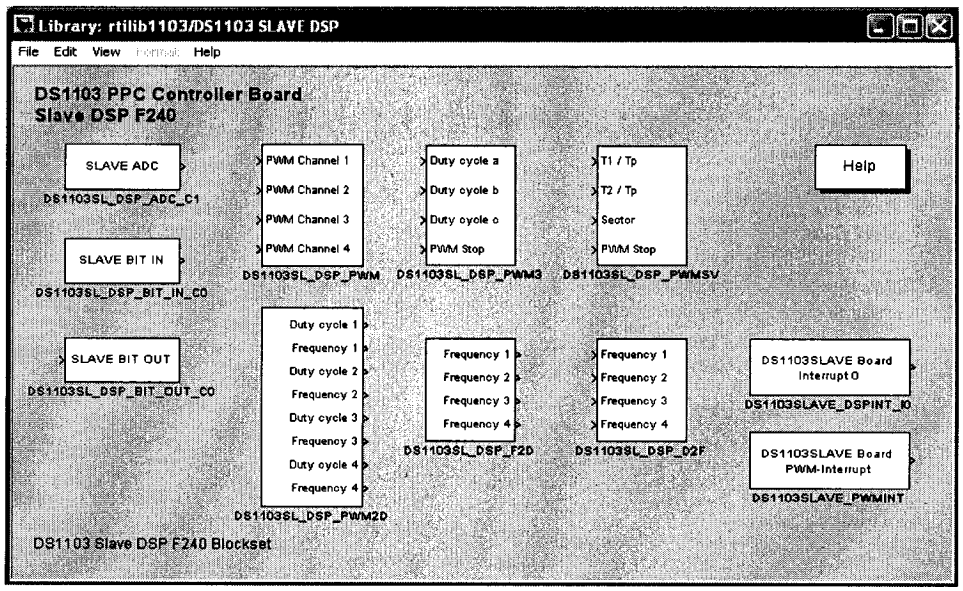

Fig. 4-4 Slave DSP block library for Simulilnk.

4.3 SELECTING LOCAL LOAD PARAMETERS

The approach used in this section for calculating the loads used in the experimental tests is based on the specification of the desired resonant frequency f_0 and quality factor Q_f. We initially choose a value for the inductor L and then calculate the value of the capacitor C that yields the desired resonant frequency since the values of capacitors available in the laboratory is more diverse than of inductors. It is worth mentioning that if the resonant frequency of the load f_0 is chosen as $60\ Hz$, the load consumes no reactive power at nominal grid frequency. Thus, if the inverter is controlled with unit power factor, the reactive power imbalance ΔQ is null, the frequency of the islanded system would be the rated grid frequency and the UFP/OFP devices would not trip. The only way for detecting islanding with the passive IDM would be through the UVP/OVP devices if the active power imbalance is significantly large.

The value of the resistor R is chosen so as to achieve a desired quality factor. For the control of the inverter, the RMS value of its current is selected so that the voltage that

appears across the isolated load is the same as when the grid is connected. As can be seen in Fig. 2-4 this relation is true only when the resonant frequency of the load is equal to the grid frequency. However, for loads with resonant frequency close to $60\,Hz$ the error in magnitude should be relatively small for small values of quality factor, as of practical interest. Notice that using the proposed approach for calculating the inverter current results in zeroing the active power imbalance ΔP. This would be the worst possible case for islanding detection since the steady-state values of the frequency and magnitude of the voltage of the islanded system would be exactly the rated values of the grid.

An example of the calculation procedure and parameter values considered for islanding tests is shown in Table 5. The inductor available in the laboratory has a maximum value of $32\,mH$ and intermediary taps with inductances equal to $8\,mH$ and $16\,mH$.

Table 5-Values of the system parameters considered for the experimental tests

V_g (V)	Q_f	f_0 (Hz)	L (mH)	$C=\frac{1}{L\omega_0^2}$ (μF)	$R=Q\sqrt{\frac{L}{C}}$ (Ω)	$I_{PV}=\frac{V_g}{R}$ (A)	$P_{PV}=V_g I_{PV}$ (W)
30	2.49	59.98	8	880	7.5	4	120
30	2.49	59.98	16	440	15	2	60
30	2.49	59.98	32	220	30	1	30

4.4 EXPERIMENTAL RESULTS AND ANALYSIS

The experiment tests have been implemented for three active IDMs, AFD, SMS and SFS. The experimental results will be analyzed separately in this section. For each active method, two cases are analyzed, the loads for which IDM works and fails. The AFD IDM performance test is implemented for the frequency drift $\delta f = 1\,Hz$ case, and the SMS

IDM performance test is implemented for the $\theta_m = 10°$, $f_m - f_g = 3Hz$ case, and the SFS IDM performance test is implemented for the $cf_0 = 0.05$, $k_{sfs} = 0.05$. The parameters are the same as those used in the simulation.

4.4.1 Load Adjustment

The actual value of most power components is not exactly the nominal value. The manufactures usually provide a tolerance range, such as ± 10%, for each component. Thus the actual value of the resonant frequency of a given *RLC* load should be obtained from preliminary tests. There are three steps in the preliminary test to adjust the load.

1) Without applying any active IDMs or UVP/OVP and UFP/OFP, open the utility disconnect switch, and let the system operate in islanding condition to achieve the load resonant frequency.

2) The islanding methods tested here depend on the frequency change to detect the islanding condition, and the voltage change is not the main concern of this experiment. Thus, the value of the variable resistance R based on Table 5 was adjusted to keep the islanding V_{PCC} within the voltage trip limit and as close as possible to the V_g.

3) Based on the available inductance in the laboratory, the capacitance value was changed to adjust the islanding system frequency to obtain the desired experimental load resonant frequency.

Thus, based on Table 5, the loads used for the experiments and will be mentioned in Section 4.4.2-4.4.4 are shown in Table 6. The value of the PV inverter current I_{PV} is also changed according to the value of the resistance to ensure the islanding PCC voltage V_{PCC} within the voltage trip limit and as close as possible to the V_g.

Table 6-Parameters of the local *RLC* loads considered for the experimental tests.

LOAD	$L\,(mH)$	$C\,(\mu F)$	$R\,(\Omega)$	Q_{fcal}	$f_{0cal}\,(Hz)$	$I_{PV}\,(A)$
1	16	470	15	2.57	58.04	2
2	16	480	15	3.00	57.43	2
3	16	460	24	4.07	58.67	1.25
4	16	450	15	2.52	59.31	2
5	16	465	24	4.10	58.35	1.25

4.4.2 AFD IDM Performance Test

The test for identifying the real-value of resonant frequency for Load 1 ($L = 16 mH$, $C = 470 \mu F$, $R = 15 \Omega$, $f_{0cal} = 58.03\ Hz$ and $Q_{fcal} = 2.57$) is carried out following the procedure described in Section 4.4.1, and the result is shown in Fig. 4-5. At $t = 2.29\ s$, the utility is disconnected and the steady-state frequency under islanding conditions is $f_{0exp} \approx 58.97\ Hz$. The error between calculated and experimental resonant frequency can be explained by the not precisely known value of the load.

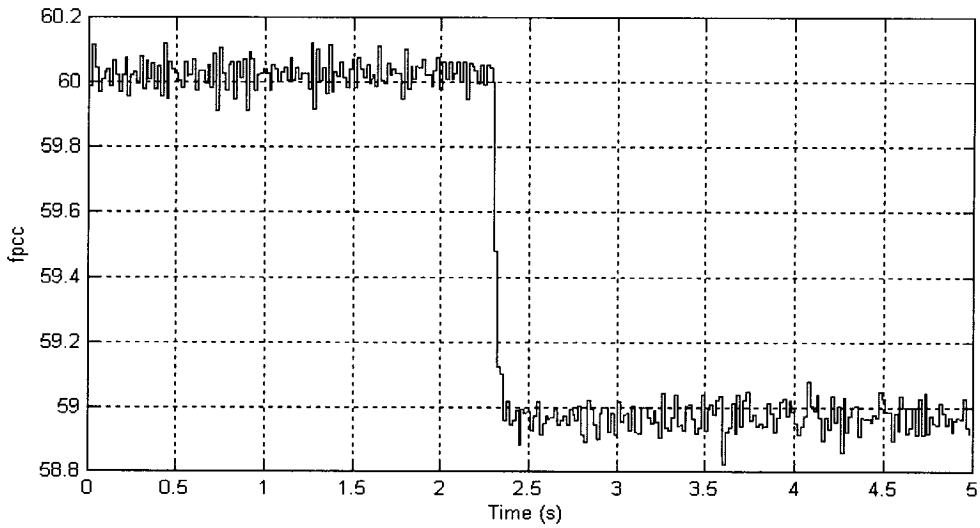

Fig. 4-5 Identification of the real value of the resonant frequency for Load 1.

The next experiment is carried out to verify the effect of AFD on the frequency of an islanded system. The desired active IDM method, in this case AFD with frequency drift $\delta f = 1\ Hz$, is selected in the reference current with IDMs block shown in Fig. 3-10. Then with the UVP/OVP and UFP/OFP devices still deactivated, the grid breaker is open and the steady state value of the frequency of the islanded system is measured.

Fig. 4-6 shows PCC frequency of the system with AFD for Load 1. The utility is disconnected at $t = 2.35\ s$, and the frequency of the islanded system is $f_{is\exp} \approx 59.6\,Hz$. According to the theoretical analysis presented in Section 2.5.2, the theoretical steady-state islanding frequency for the load with $Q_f = 2.57$ and $f_0 = 58.97\,Hz$ is $f_{iscal} = 59.56\,Hz$. Also, simulation of AFD for the load with the same resonant frequency and quality factor was run to compare with the experimental results. The simulated steady state frequency under islanding condition is $f_{issim} = 59.63\,Hz$. The calculated, simulated and experimental islanding frequencies are close, thus, the experiment verifies the calculation and simulation. Comparing Fig. 4-5 and 4-6, one can see that the effect of the AFD at speed-up mode was to increase the value of the frequency of the islanded system from its resonant frequency.

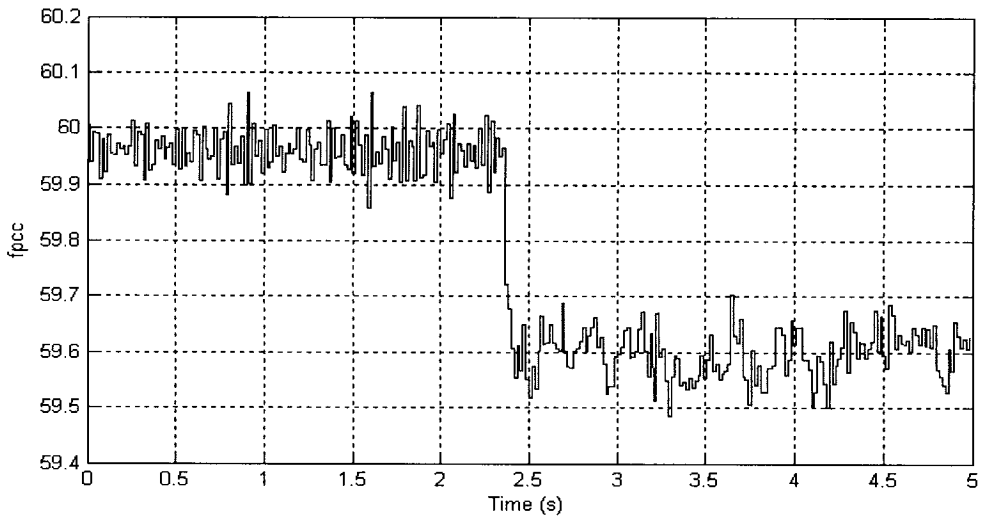

Fig. 4-6 PCC voltage frequency variation of the system with AFD for Load 1.

Fig. 4-7 shows one cycle of the inverter current i_{PV} along with its reference current i_{PVref}, and grid voltage v_{PCC} waveforms for Load 1. Here, one can see that the current frequency is higher than the voltage frequency, and there is a zero current segment at the end of each current cycle before a new voltage cycle starts, due to the implementation of AFD IDM.

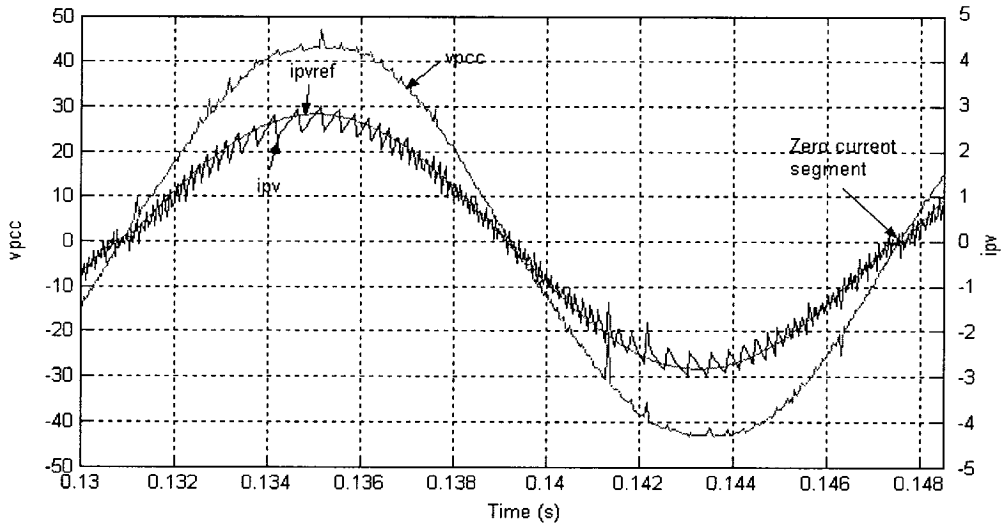

Fig. 4-7 Inverter current and PCC voltage waveforms of the system with AFD.

Finally, a test with all blocks enabled is carried out to verify the main waveforms of the system and the performance of the AFD IDM after the grid is disconnected. Fig. 4-8 shows the waveforms of the grid current i_{ac}, the PV inverter current i_{PV}, and the load current i_{load} and PCC voltage v_{PCC}. According to the load adjustment step 2, the current flowing in the grid prior to grid disconnection should be very small, mostly reactive. However what one sees there is a waveform composed essentially of low order harmonics. These are due to nonlinear loads connected to the same grid, such as oscilloscope and computers, which flow through the low impedance of the capacitor used to model the local load. This is confirmed by the distorted load current before the grid is disconnected, i.e. t = 2.35 s. By

inspection one sees that the magnitude of the load voltage remains virtually unchanged. As observed in the previous test, the frequency of the islanded system would decrease until the islanded steady-state frequency $f_{is\exp} \approx 59.6Hz$ reached. Since this value is within the thresholds of the UFP/OFP devices, the devices did not trip and undetectable islanding occurred. Thus, this experiment test verified that the load with resonant frequency $f_0 = 58.97\,Hz$ and quality factor $Q_f = 2.57$ is inside the non detection zone, as predicted in Fig. 3-16, NDZ of the theoretical and simulation results of AFD.

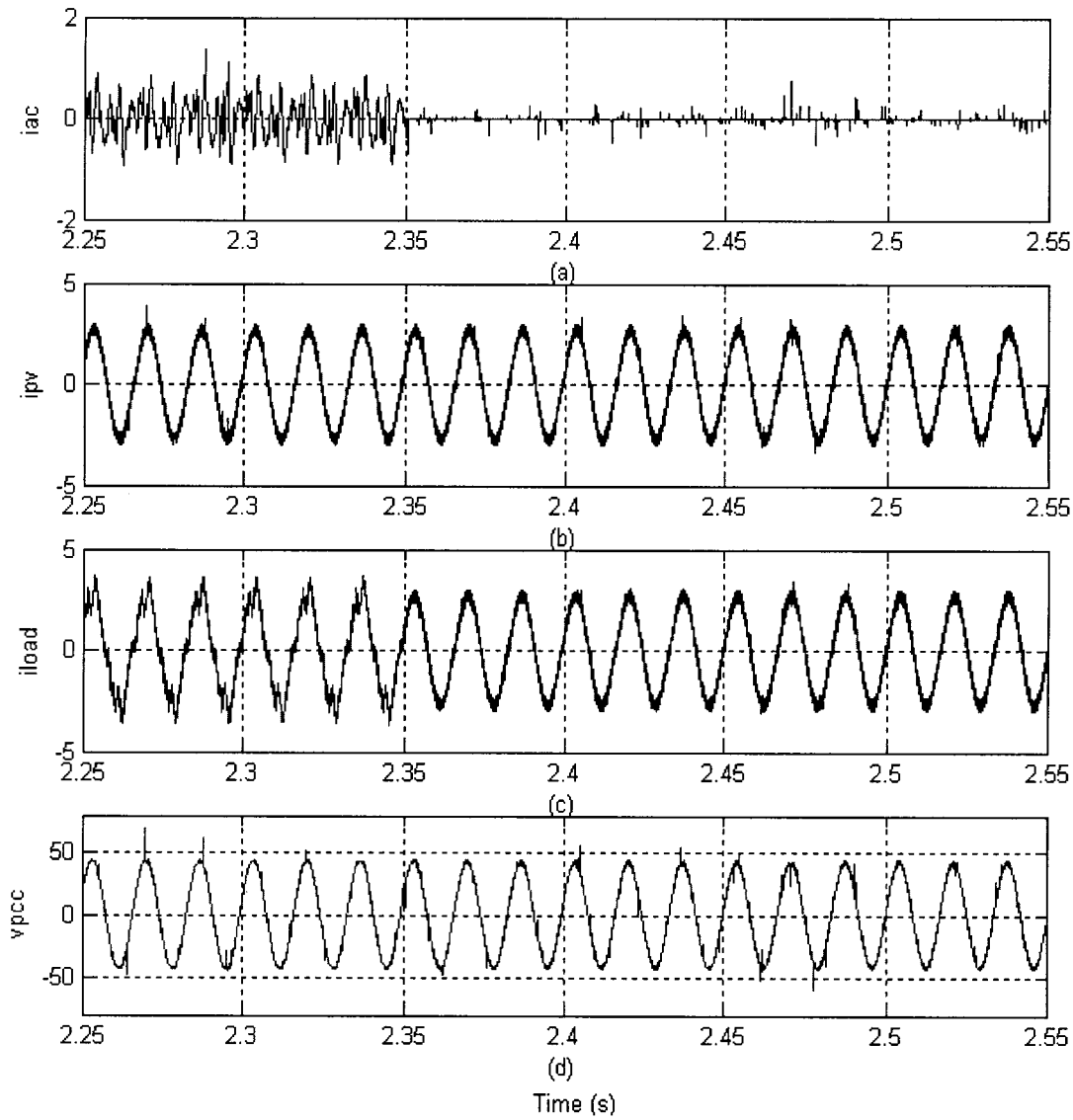

Fig. 4-8 Currents and voltage waveforms of the system with AFD before and after grid disconnected for Load 1.

The same approach was followed for Load 2 ($L = 16mH$, $C = 480\mu F$, $R = 15\Omega$, $f_{0cal} = 57.43\ Hz$ and $Q_{fcal} = 3.00$). The actual value of the resonant frequency of the load is obtained with the inverter operating with unit power factor (no active IDMs) and with the UFP/OFP and UVP/OVP devices deactivated. Fig. 4-9 shows PCC frequency of the system with AFD for Load 2. The utility is disconnected at $t = 2.51\ s$, and the real-value of the load resonant frequency is $f_{0\exp} \approx 58.34\ Hz$.

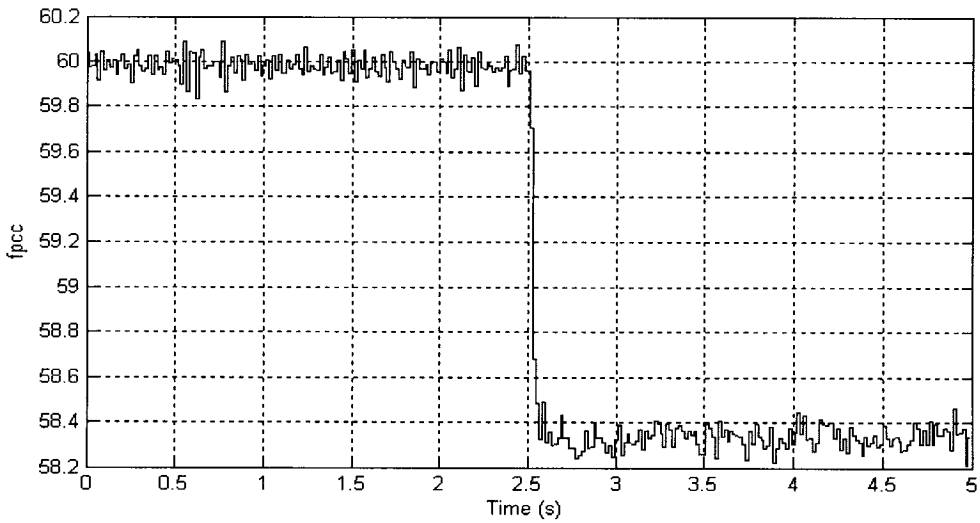

Fig. 4-9 Identification of the real value of the resonant frequency for Load 2.

Then AFD IDM was applied, and the PCC frequency is shown in Fig. 4-10. The utility is disconnected at $t = 2.16\ s$, and the frequency of the islanded system is $f_{is\exp} \approx 58.97\ Hz$. The theoretical steady-state islanding frequency for the load with $Q_f = 3$ and $f_0 = 58.34\ Hz$ is $f_{iscal} = 58.85\ Hz$. Also, the simulated steady state frequency under islanding condition is $f_{issim} = 59.91\ Hz$. The calculated, simulated and experimental islanding frequencies are close, thus, the experiment verifies the calculation and simulation.

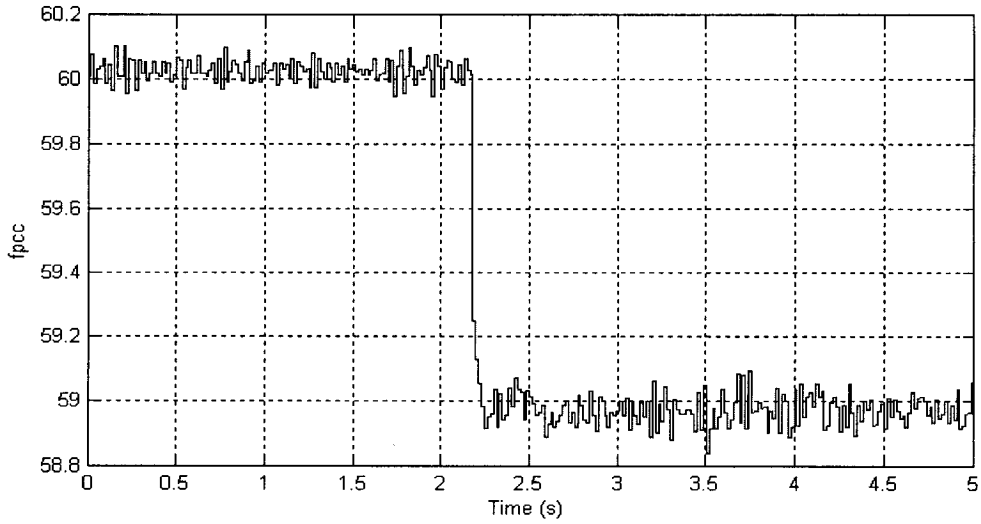

Fig. 4-10 PCC voltage frequency variation of the system with AFD but no UFP/OFP for Load 2.

Since this frequency lies outside the threshold of the UFP/OFP devices, the devices should trip and islanding would be detected and prevented, when the devices were activated. This can be seen in Fig. 4-11, which shows the four most relevant waveforms of the system, the grid current i_{ac}, PV inverter current i_{PV}, the load current i_{load}, and the PCC voltage v_{PCC}. There one sees that the utility breaker opens at $t = 2.41s$ and that the system operates for some time under islanding condition. The system frequency decreases and at $t = 2.52\,s$ the UFP/OFP devices shut down the inverter. Fig. 4-12 shows the variation of the PCC voltage frequency. From approximately 60 Hz, the grid frequency, f_{PCC} decreases towards $f_{is\exp} \approx 58.97Hz$, which is below the setting of the UFP device, and causes the shutdown of the inverter after 6 line cycles as required by the IEEE Std. 929-2000. The value of the frequency shown after the inverter is shut down is irrelevant and should be disregarded. Thus, this experiment test verified that the load with resonant frequency $f_0 = 58.34\,Hz$ and quality factor $Q_f = 3.00$ is outside the non detection zone, as predicted in Fig. 3-16, NDZ of the theoretical and simulation results of AFD.

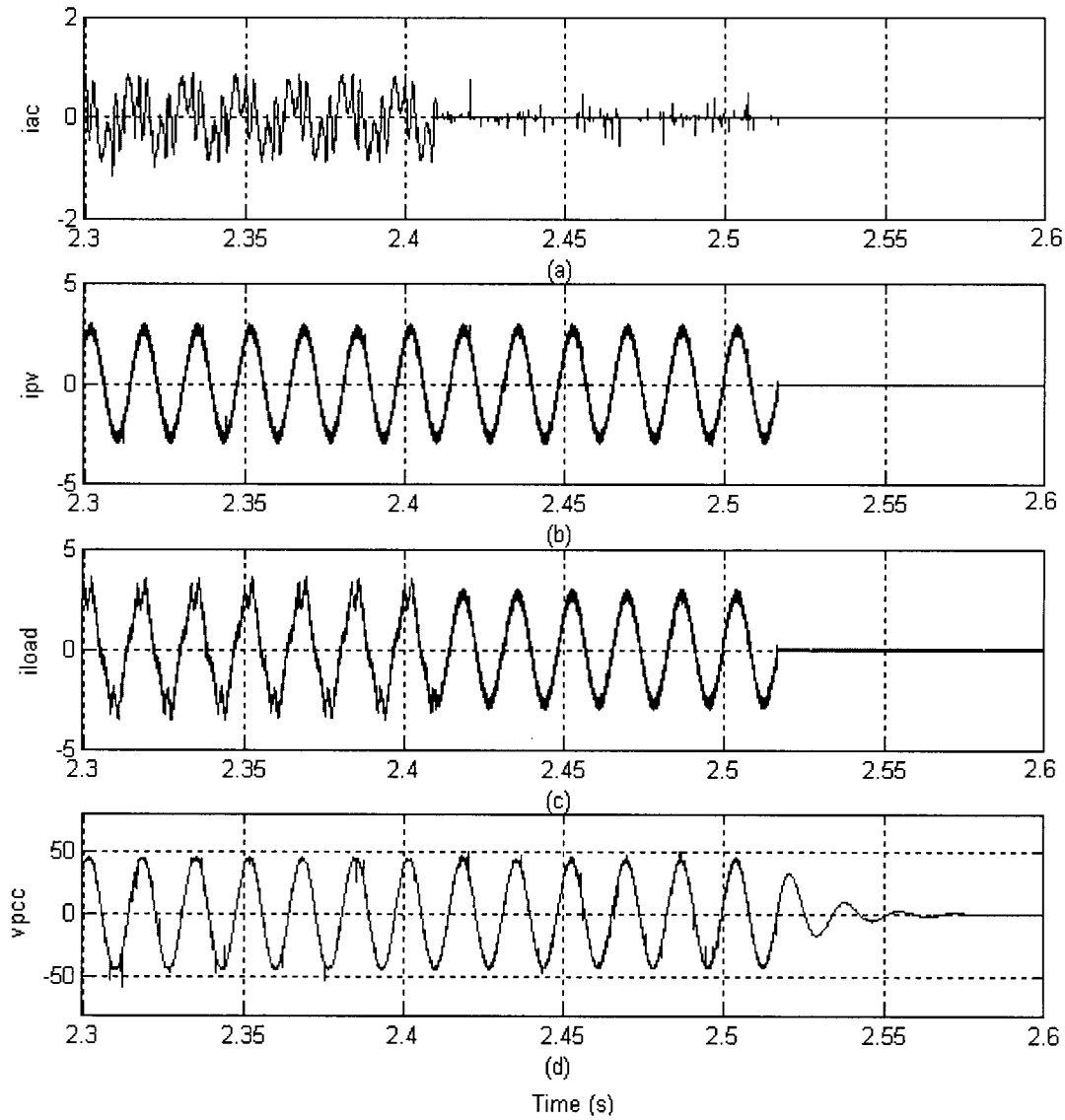

Fig. 4-11 Currents and voltage waveforms of the system with AFD before and after grid disconnected for Load 2.

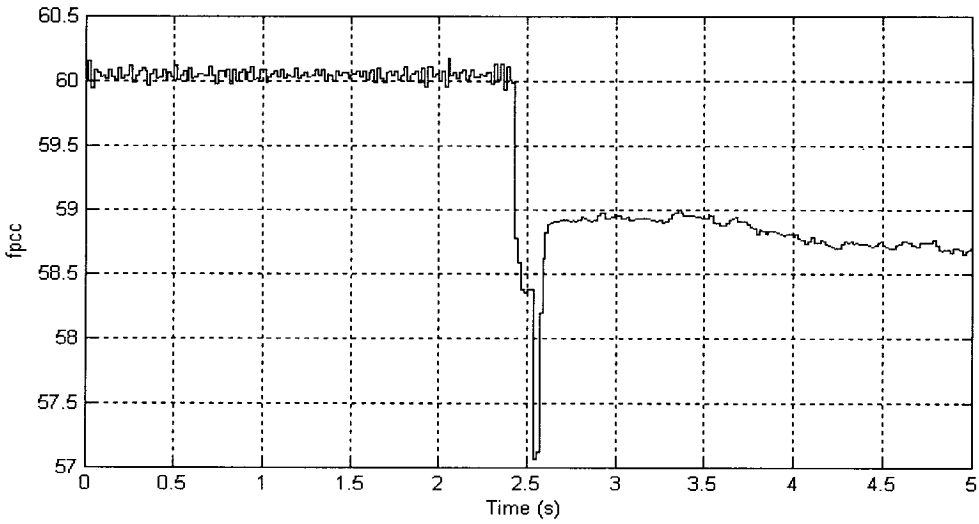

Fig. 4-12 PCC voltage frequency variation of the system with AFD and UFP/OFP for Load 2.

4.4.3 SMS IDM Performance Test

In order to verify that the NDZ in Q_f vs. f_0 space covers all values of resistance R, different resistance is considered in the first test with the SMS IDM. In order to keep the islanded PCC voltage with the voltage protection limit, the PV inverter current changed to $I_{PV} = 1.25A$ for load 3 ($L = 16mH$, $C = 460\mu F$, $R = 24\Omega$, $f_{0cal} = 58.67\ Hz$ and $Q_{fcal} = 4.07$). As for AFD, we first identify the real value of the load resonant frequency, then the frequency of the system when the inverter is controlled with the active IDM, and finally, with the UFP/OFP and UVP/OVP devices enabled, we verify if islanding can be successfully detected.

Fig. 4-13 shows the variation of the system frequency after the grid breaker opens at $t = 2.59\ s$ and the inverter is controlled with unity power factor, no active IDMs. One can see that the frequency of the islanded system changes to $f_{0\exp} \approx 59.85\ Hz$, that is the real value of the resonant frequency of the load.

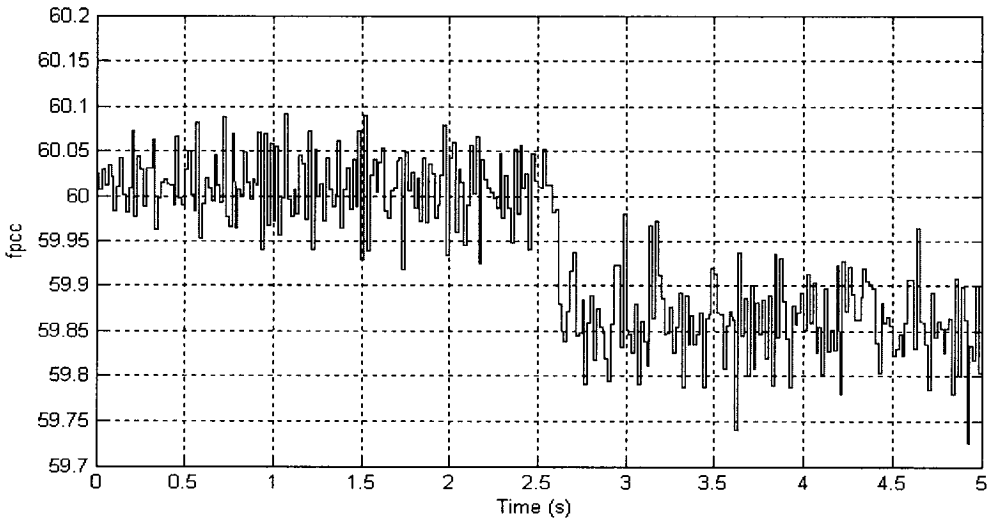

Fig. 4-13 Identification of the real value of the resonant frequency for Load 3.

With SMS IDM, a new test was implemented and the results are shown in Fig. 4-14. After the grid breaker opens at $t = 2.29\ s$, the frequency of the load voltage decreases to $f_{is\exp} \approx 59.57 Hz$. Since the resonant frequency of the load was lower than 60 Hz, the frequency of the islanded system decreases as a result of the SMS IDM. The relatively small variation in frequency is due to the high quality factor of the load. According to the theoretical analysis presented in Section 2.5.3, the theoretical steady-state islanding frequency for the load with $Q_f = 4.07$ and $f_0 = 59.85 Hz$ is $f_{iscal} = 59.57 Hz$. Also, the simulated steady state frequency under islanding condition is $f_{issim} = 59.43 Hz$. The calculated, simulated and experimental islanding frequencies are close, thus, the experiment verifies the calculation and simulation. Since this frequency is within the frequency trip set points, the UFP/OFP block would not trip and islanding condition should occur. Thus, this experiment test verified that the load with resonant frequency $f_0 = 59.85 Hz$ and quality factor $Q_f = 4.07$ is inside the NDZ of SMS as predicted in Fig. 3-19, NDZ of the theoretical and simulation results of SMS. The waveforms of the

system are not shown for this method because they are quite similar to those shown for the AFD IDM.

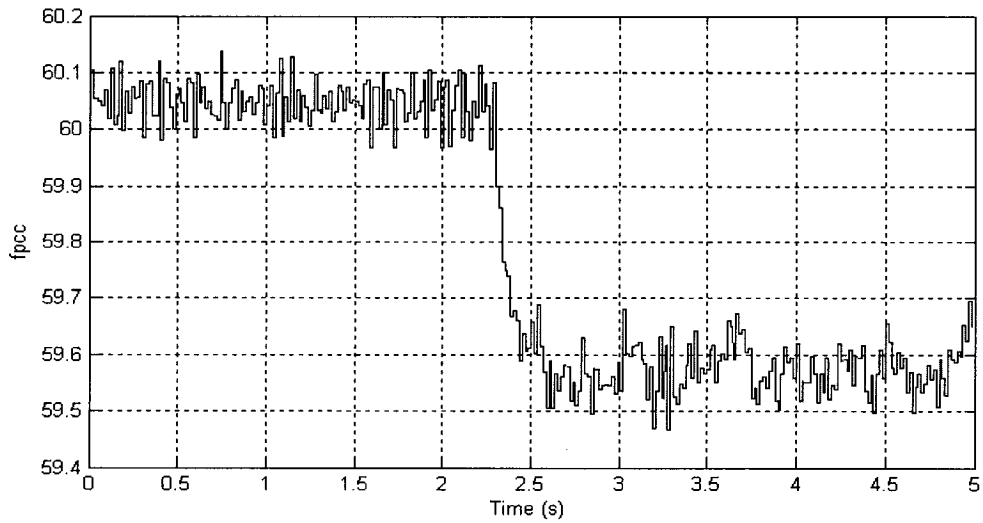

Fig. 4-14 PCC voltage frequency variation of a system with SMS for Load 3.

Load 4 ($L = 16mH$, $C = 450\mu F$, $R = 15\Omega$, $f_{0cal} = 59.31\,Hz$ and $Q_f = 2.52$) has been chosen for the second test with the SMS IDM. Fig. 4-15 shows the experiment that identifies the real resonant frequency of the load as $f_{0\exp} \approx 60.3Hz$. Fig. 4-16 shows the frequency of the load voltage. There one sees that the IDM was capable of drifting the frequency to $f_{is\exp} \approx 62.38Hz$. According to the theoretical analysis presented in Section 2.5.3, the theoretical steady-state islanding frequency for the load with $Q_f = 2.52$ and $f_0 = 60.3\,Hz$ is $f_{iscal} = 62.32\,Hz$. Also, the simulated steady state frequency under islanding condition is $f_{issim} = 62.24Hz$. The calculated, simulated and experimental islanding frequencies are close, thus, the experiment verifies the calculation and simulation. Notice that the unlike the previous case, the islanded frequency increased because the actual resonant frequency of the load was larger than 60 Hz. Besides, since the quality factor of this load is smaller, the variation in the islanded frequency caused by the SMS IDM is larger than in the previous case. As the islanding frequency exceeds the

frequency trip set points of the UFP/OFP block, this should trip if enabled. This can be seen in the last test shown in Fig. 4-17. The grid breaker opens at $t = 2.53s$, the frequency of the islanded system increases until the inverter is shut down at $t = 2.67\ s$. Thus, this experiment test verified that the load with resonant frequency $f_0 = 60.3Hz$ and quality factor $Q_f = 2.52$ is outside the NDZ of SMS, as predicted in Fig. 3-19.

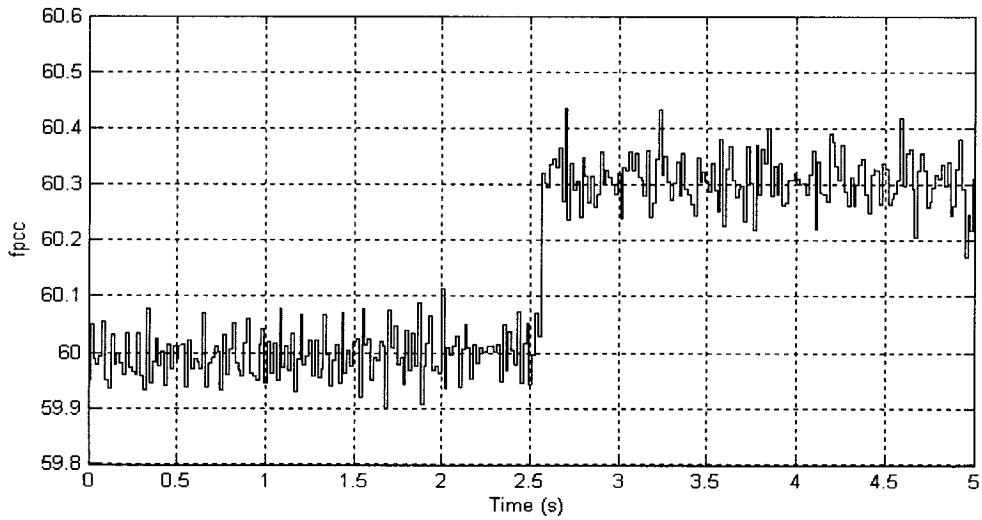

Fig. 4-15 Identification of the real value of the resonant frequency for Load 4.

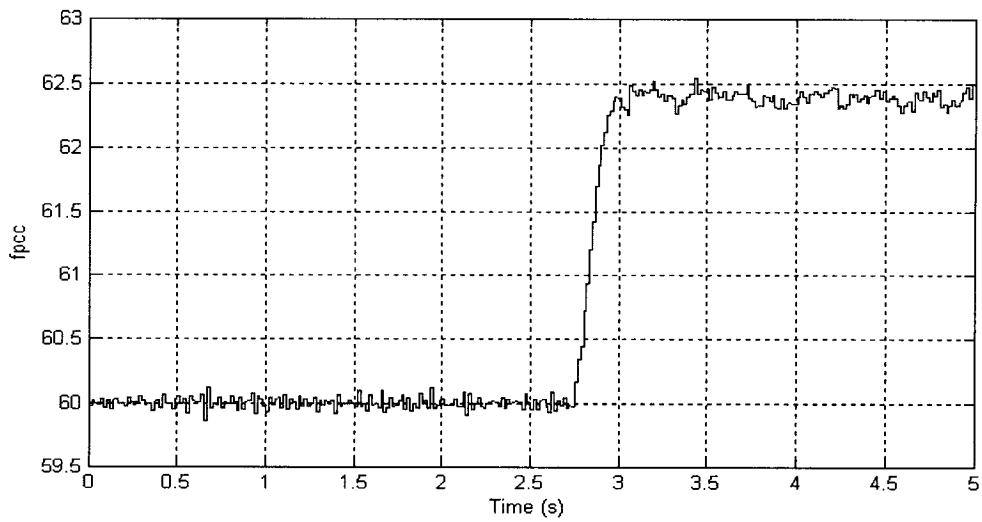

Fig. 4-16 PCC voltage frequency variation of the system with SMS but no UFP/OFP for Load 4.

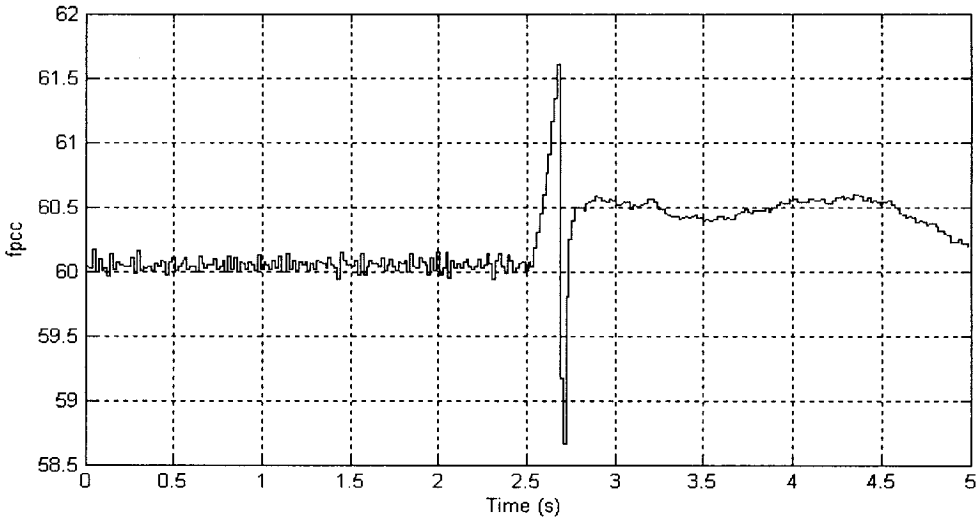

Fig. 4-17 PCC voltage frequency variation of the system with SMS and UFP/OFP for Load 4.

Fig. 4-18 shows one cycle of the inverter current i_{PV} along with its reference current i_{PVref}, and grid voltage v_{PCC} waveforms for load 4 under islanding condition. Here, one can see there is a phase shift between voltage and current due to the implementation of SMS IDM.

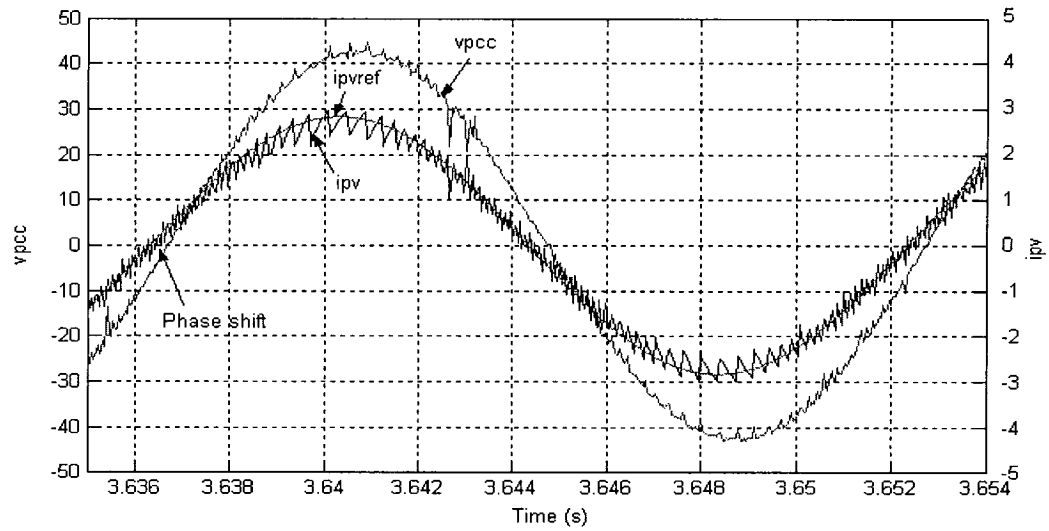

Fig. 4-18 Inverter current and PCC voltage waveforms of the system with SMS.

4.4.4 SFS IDM Performance Test

Load 5 ($L = 16mH$, $C = 465\mu F$, $R = 24\Omega$, $f_{0cal} = 58.35\ Hz$ and $Q_{fcal} = 4.10$) has been chosen for the first test with the SFS IDM. As for AFD and SMS, we first identify the real value of the resonant frequency of the load, then the frequency of the system when the inverter is controlled with the active IDM and finally, with the UFP/OFP and UVP/OVP devices enabled, we verify if islanding is successfully detected.

Fig. 4-19 shows the variation of the system frequency before and after the grid breaker opens, i.e. at $t = 2.41\ s$, and the inverter is controlled with unity power factor, no active IDMs. One can see that the frequency of the islanded system changes to $f_{0\exp} \approx 59.52\ Hz$, that is the real value of the resonant frequency of the load.

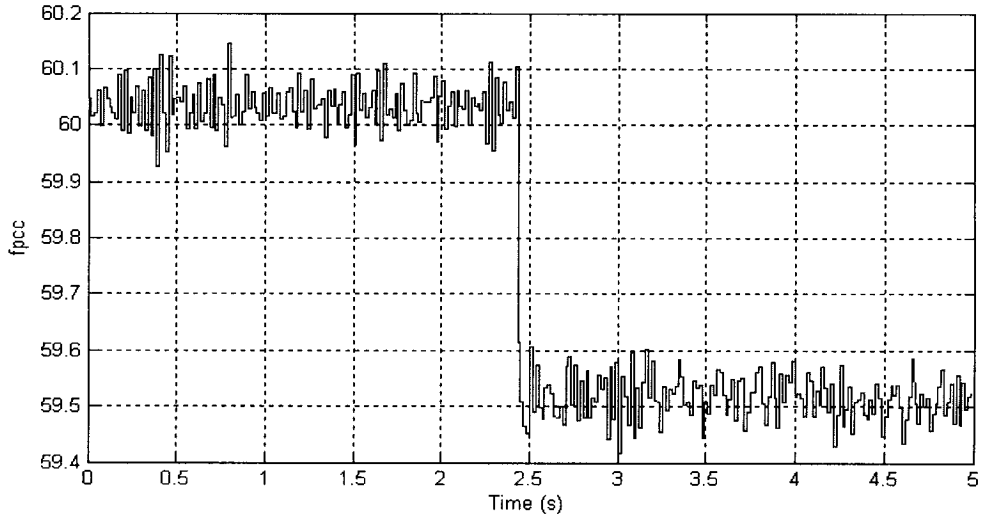

Fig. 4-19 Identification of the real value of the resonant frequency for Load 5.

With the inverter controlled with SFS IDM, a new test is run and the results are shown in Fig. 4-20. After the grid breaker opens at $t = 2.43\ s$, the frequency of the load voltage changes to $f_{is\exp} \approx 60.22Hz$. According to the theoretical analysis presented in Section 2.5.4, the theoretical steady-state islanding frequency for the load with $Q_f = 4.10$ and $f_0 = 59.52Hz$ is $f_{iscal} = 62.23Hz$. Also, the simulated steady state frequency under

islanding condition is $f_{issim} = 60.29Hz$. The calculated, simulated and experimental islanding frequencies are close, thus, the experiment verifies the calculation and simulation. Since this frequency is within the frequency trip set points, the UFP/OFP block would not trip and islanding condition should occur. Thus, the experiment verifies that load with $Q_f = 4.10$ and $f_0 = 59.52Hz$ is inside the NDZ of SFS as predicted by Fig. 3-22, NDZ of the theoretical and simulation results of SFS.

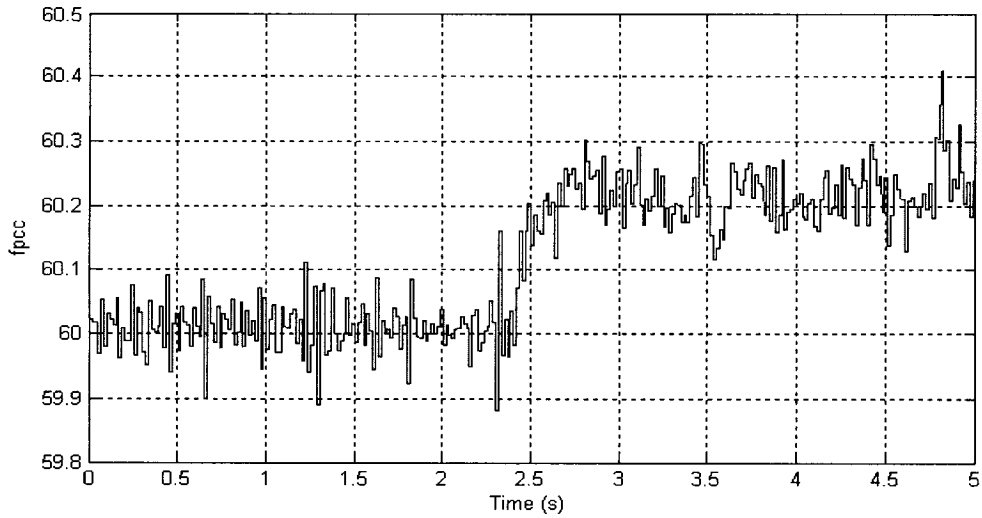

Fig. 4-20 PCC voltage frequency variation of a system with SFS for Load 5.

Fig. 4-21 shows one cycle of the inverter current i_{PV} along with its reference current i_{PVref}, and grid voltage v_{PCC} waveforms for Load 1. Here, one can see that there is a zero current segment at the end of current half cycle until a new voltage half cycle starts, due to the implementation of SFS IDM.

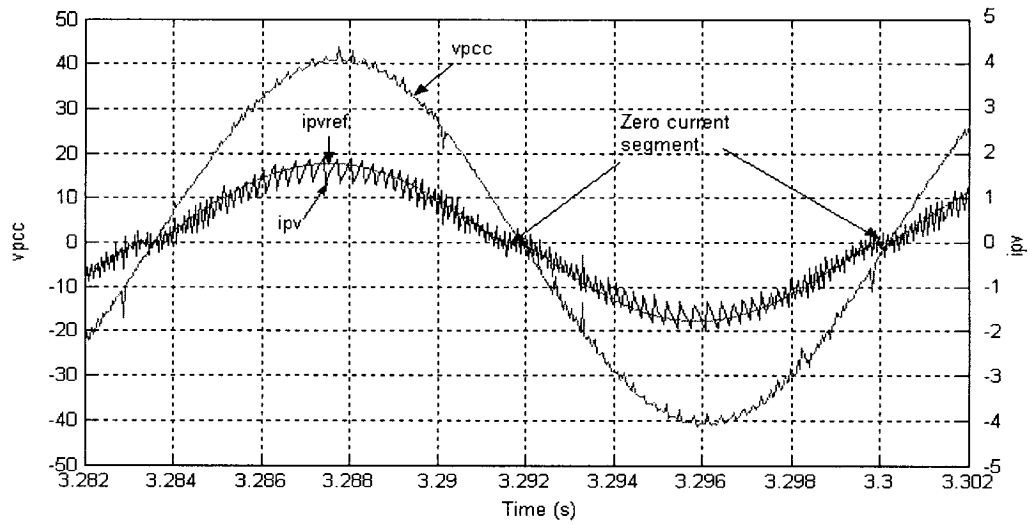

Fig. 4-21 Inverter current and PCC voltage waveforms of the system with SFS.

Load 1 ($L = 16mH$, $C = 470\mu F$, $R = 15\Omega$, $f_{0cal} = 58.03\ Hz$ and $Q_{fcal} = 2.57$) has been chosen again for the second test with the SFS IDM. The real value of the resonant frequency of this load has been identified before as $f_{0\exp} \approx 58.97Hz$. Fig. 4-22 shows the variation of the frequency of the load voltage when the inverter is controlled with SFS IDM. At $t = 2.50\ s$, the utility breaker opens and the system frequency under islanding conditions decreases to $f_{is\exp} \approx 58.40Hz$. According to the theoretical analysis presented in Section 2.5.3, the theoretical steady-state islanding frequency for the load with $Q_f = 2.57$ and $f_0 = 58.97\,Hz$ is $f_{iscal} = 58.3\,Hz$. Also, the simulated steady state frequency under islanding condition is $f_{issim} = 58.35Hz$. The calculated, simulated and experimental islanding frequencies are close, thus, the experiment verifies the calculation and simulation. As the islanding frequency exceeds the frequency trip set points of the UFP/OFP block, this should trip if enabled. This can be seen in the last test shown in Fig. 4.20. The grid breaker opens at $t = 2.42s$, the frequency of the islanded system decreases until the inverter is shut down at $t = 2.75\ s$. Thus, the experiment verifies that load with $Q_f = 2.57$ and $f_0 = 58.97\,Hz$ is outside the NDZ of SFS as predicted in predicted in

Fig. 3-22, NDZ of the theoretical and simulation results of SFS. Again, the value of the frequency shown after the inverter is shut down is irrelevant and should be disregarded.

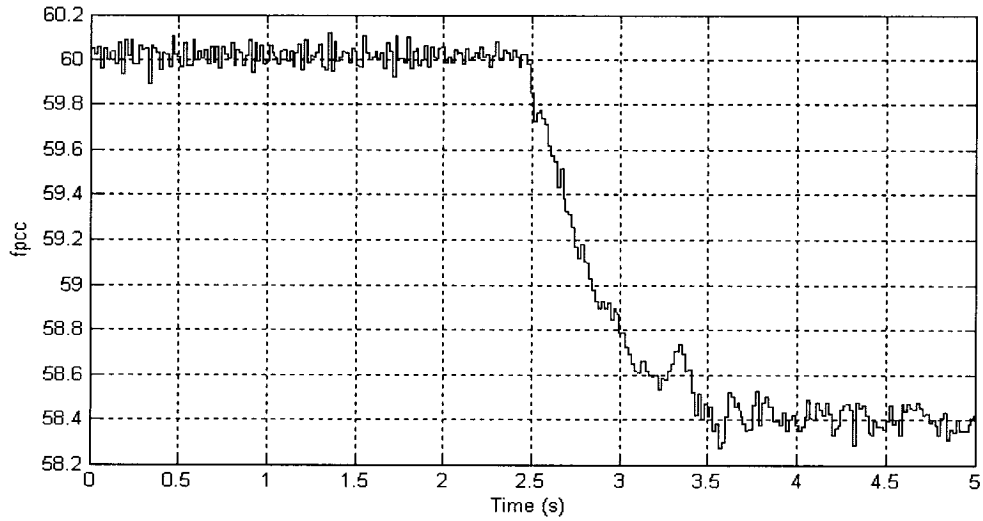

Fig. 4-22 PCC voltage frequency variation of the system with SFS but no UFP/OFP for Load 1.

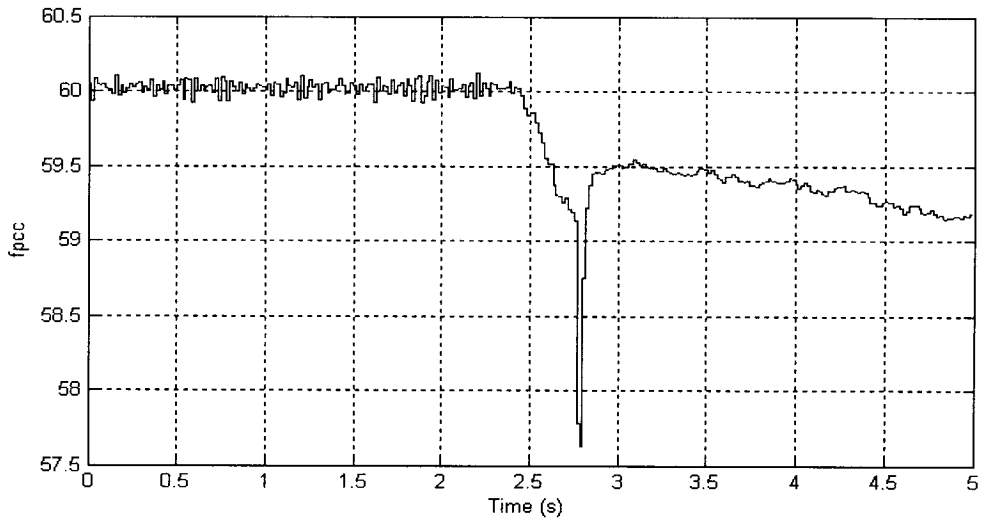

Fig. 4-23 PCC voltage frequency variation of the system with SFS and UFP/OFP for Load 1.

4.5 CONCLUSIONS

This Chapter has presented the experimental results to validate the theoretical analysis and simulation results presented in previous chapters. First, the hardware used to implement the set-up has been described in details. The control circuit of the inverter, with hysteresis current control and three different active IDMS were implemented in a DSP development kit from dSPACE. The availability of a piece of software that converts the MATLAB Simulink blocks in to DSP code made the practical implementation very easy.

From the experimental results, we noticed that the resonant frequency of a given *RLC* load was usually not that calculated from the nominal values of the components. In order to obtain an experimental value for the loads, we islanded the system with the inverter operating with unit power factor and the UFP/OFP and UVP/OVP devices disabled. We also noticed in the prototype that the grid current was not zero during grid connected operation despite an attempt to select a load that would yield zero active and reactive power imbalances. There was a distorted current composed mostly of low order harmonics that are believed to be created by some nonlinear loads connected to the ac grid and that would circulate through the capacitor used to represent the local load. However, it did not have any impact on the islanding detection tests.

Finally, we run two tests for each active IDM. One with a load that would result in islanding condition and the other with a load that would allow islanding prevention, according to the theoretical analysis presented in Chapter 2. The experimental results confirmed that the NDZs derived for the active IDMs in the proposed Q_f vs. f_0 load parameter space are indeed correct.

CHAPTER 5
CONCLUSION

5.1 SUMMARY

Because islanding condition would cause both operational and maintenance problems for grid-connected distributed power generation systems (DG), islanding operation should be prevented. In order to control islanding phenomenon, it must be detected. The most common techniques for islanding detection based on local parameters are the passive and the active methods that are reviewed in Chapter1. The performance assessment and the comparison of these islanding detection methods (IDMs) require a performance index. The most common performance index is referred to as non detection zone (NDZ). It defines a region where islanding will occur with specific system parameters. In this Thesis, passive method has been analyzed in a power imbalance, ΔP vs. ΔQ space.

In chapter 2, the equations that described the true NDZ of constant current controlled and constant power controlled unity power factor inverters were derived. However, NDZ in power imbalance, ΔP vs. ΔQ space, is not adequate to evaluate the performance of active IDMs since it does not allow the representation of the control parameters of the IDMs. A C_{norm} vs. L load parameter space can do that but it is not convenient since the NDZ would change with the value of the load resistance R and a new NDZ would have to be plotted for each condition that needs to be investigated. Thus, in Chapter 2, a new load parameter space with the quality factor and the resonant frequency of the local load (Q_f vs. f_0) is proposed to overcome the disadvantage of the

previous two spaces. Equations that described the NDZs of three common active IDMs, namely active frequency drift (AFD), slip-mode phase shift (SMS) and Sandia frequency shift (SFS) were derived. From the plots of the NDZ Fig. 2-7 for the AFD IDM, one can see that there will always be a NDZ for this method for all quality factors. The benefits of this method are relatively small. It shifts the NDZ of loads with a low quality factor to a region that represents capacitive loads at the line frequency. Since these loads are not very common, islanding is unlikely happen. The plots of the NDZs of SMS and SFS, Fig.2-8 and Fig. 2-9 clearly show that they can guarantee islanding detection as long as the load presents a quality factor lower than the designed value.

The simulation and experimental results demonstrated the validation of the proposed Q_f vs. f_0 space for three common active IDMs. The grid-connected PV system has been modeled and simulated by the use of Matlab Simulink, as shown in Chapter 4. Blocks UFP/OFP & UVP/OVP, hysteresis controller, reference current generator for AFD, SMS and SFS have been implemented. The correlation between theoretical results and simulation results, as shown in Fig. 3-19 and 3-22, is very good. On the other hand, there was a significant error for the AFD method for loads with low quality factor, shown in Fig. 3-13. We believe that this error is due to the asymmetric voltage waveform caused by the distorted PV inverter output current. Nonetheless, an alternative approach for deriving the NDZ of AFD using Laplace transform has been proposed and shown to have very good agreement with the simulation results in Fig. 3-16.

Finally, a laboratory prototype was built to validate the simulation results. The detailed of the experiment set-up and the experiment procedure has been discussed in Chapter 5. The experimental result shows great agreement with the simulation results.

5.2 CONTRIBUTIONS

The major contributions of this thesis are:

(1) Analyzed the effectiveness of passive islanding detection methods in the ΔP vs. ΔQ space. Derived equations that represent the non-detection zones (NDZ) of unity power factor current controlled inverters with constant current and constant power. Identified that the NDZ is smaller for the first case.

(2) Proposed a new load parameter space (Q_f vs. f_0) for representing non detection zones of active frequency drifting islanding detection methods. Unlike the C_{norm} vs. L space, the proposed space allows the easy assessment of the IDMs for different values of load resistance with a single curve. Besides, it clearly shows how the size and shape of the NDZ varies when the control parameters of the IDMs are varied. Also, the error of the theoretical and simulated results of the AFD IDM NDZ has been analyzed and an alternative approach, mapping the NDZ by Laplace transform, has been presented to solve the problem.

(3) A laboratory prototype was built and experimental results verified the theoretical analysis and computer simulation.

5.3 SUGGESTIONS FOR FUTURE WORK

(1) Verify the effectiveness of active IDMs of the systems with multiple inverters and see if they have detrimental interaction.

(2) Investigate islanding detection methods that are not inverter-residented.

(3) Incorporate active anti-islanding techniques with maximum power point tracking algorithm and other features such as active filtering and reactive power compensation to implement an advanced PV inverter.

REFERENCES

[1] Kern, G.A., "SunSine300, utility interactive AC module anti-islanding test results," Photovoltaic Specialists Conference, 1997, Conference Record of the Twenty-Sixth IEEE, 29 Sept.-3 Oct. 1997

[2] IEEE Std. 929-2000, "IEEE Recommended Practice for Utility Interface of Photovoltaic (PV) systems".

[3] Wall, S.R., "Performance of inverter interfaced distributed generation," Transmission and Distribution Conference and Exposition, 2001 IEEE/PES, Volume: 2, 28 Oct.-2 Nov. 2001.

[4] Jun Yin; Liuchen Chang; Diduch, C., "Recent developments in islanding detection for distributed power generation," Power Engineering, 2004. LESCOPE-04. 2004 Large Engineering systems Conference on, 28-30 July 2004

[5] W. Bower and M. Ropp, "Evaluation of islanding detection methods for photovoltaic utility-interactive power systems," Task V, Report IEA-PVPS T5-09: 2002, March 2002.

[6] Ropp, M.E.; Begovic, M.; Rohatgi, A., "Analysis and performance assessment of the active frequency drift method of islanding prevention," Energy Conversion, IEEE Transactions on, Volume: 14, Issue: 3, Sept. 1999

[7] Smith, G.A.; Onions, P.A.; Infield, D.G., "Predicting islanding operation of grid connected PV inverters," Electric Power Applications, IEE Proceedings- , Volume: 147, Issue: 1, Jan. 2000

[8] M. Ropp, M. Begovic, A. Rohatgi, G.A. Kern, R.H. Bonn and Gonzalez, "Determining the relative effectiveness of islanding detection methods using phase criteria and

nondetection zones," *IEEE Transactions on Energy Conversion*, vol. 15, Issue: 3, Sept. 2000.

[9] John, V.; Zhihong Ye; Kolwalkar, A.; "Investigation of anti-islanding protection of power converter based distributed generators using frequency domain analysis," Power Electronics, IEEE Transactions on, Volume: 19, Issue: 5 , Sept. 2004

[10] Guo-Kiang Hung; Chih-Chang Chang; Chern-Lin Chen, "Automatic phase-shift method for islanding detection of grid-connected photovoltaic inverters," Energy Conversion, IEEE Transactions on, Volume: 18, Issue: 1, March 2003

[11] Fu-Sheng Pai; Shyh-Jier Huang, "A detection algorithm for islanding-prevention of dispersed consumer-owned storage and generating units," Power Engineering Society Winter Meeting, 2002. IEEE, Volume: 1, 27-31 Jan. 2002

[12] Hudson, R.M.; Thorne, T.; Mekanik, F.; Behnke, M.R.; Gonzalez, S.; Ginn, J., "Implementation and testing of anti-islanding algorithms for IEEE 929-2000 compliance of single phase photovoltaic inverters," Photovoltaic Specialists Conference, 2002. Conference Record of the Twenty-Ninth IEEE, 19-24 May 2002

[13] Kotsopoulos, A.; Duarte, J.L.; Hendrix, M.A.M.; Heskes, P.J.M., "Islanding behaviour of grid-connected PV inverters operating under different control schemes," Power Electronics Specialists Conference, 2002. pesc 02. 2002 IEEE 33rd Annual, Volume: 3, 23-27 June 2002

[14] Z. Ye, A. Kolwalkar, Y. Zhang, P. Du and R. Walling, "Evaluation of anti-islanding schemes based on nondetection zone concept," *Proceedings of the 34th IEEE Power Electronics Specialist (PESC 2003)*, vol. 4, 15-19 June 2003, Pages: 1735 – 1741.

[15] S. Buso, L. Malesani, P. Mattavelli, "Comparison of Current Control Techniques for Active Filter Applications", IEEE Transaction on Industrial Electronics, Vol. 45, No.5, October 1998., pp.722-729

[16] M.P. Kazmierkowski, L. Malesani, "Current control techniques for three-phase voltage-source PWM converters: a survey", Industrial Electronics, IEEE Transactions on Industrial Electronics, Vol. 45, No. 5, Oct.1998., pp. 691 -703

[17] Jeraputra, C.; Enjeti, P.N.; "Development of a robust anti-islanding algorithm for utility interconnection of distributed fuel cell powered generation", Power Electronics, IEEE Transactions on, Volume: 19, Issue: 5, Sept. 2004, Pages: 1163 – 1170

[18] Youngseok Jung; Junghun Sol; Gwonjong Yu; Jaeho Choj; "Modelling and analysis of active islanding detection methods for photovoltaic power conditioning systems", Electrical and Computer Engineering, 2004. Canadian Conference on , Volume: 2 , 2-5 May 2004, Pages:979 - 982 Vol.2

[19] Tsukamoto, O.; Okayasu, T.; Yamagishi, K.; "Study on islanding of dispersed photovoltaic power system connected to a utility power grid", Solar Energy Vol. 70, No. 6, pp. 505-511, 2001

[20] Shyh-Jier Huang; Fu-Sheng Pai; "An active islanding-detection method for power conditioning subsystem of utility interactive photovoltaic system", Power Engineering Society Summer Meeting, 2000. IEEE, Volume: 3, 16-20 July 2000, Pages: 1750 - 1755 vol. 3

[21] Shyh-Jier Huang; Fu-Sheng Pai; "A new approach to islanding detection of dispersed generators with self-commutated static power converters", Power Delivery, IEEE Transactions on, Volume: 15, Issue: 2, April 2000, Pages: 500 – 507

[22] Ishida, T.; Hagihara, R.; Yugo, M.; Makino, Y.; Maekawa, M.; Takeoka, A.; Suzuki, R.; Nakano, S.; "Anti-islanding protection using a twin-peak band-pass filter in interconnected PV systems, and substantiating evaluations", Photovoltaic Energy Conversion, 1994., Conference Record of the Twenty Fourth ; IEEE Photovoltaic Specialists Conference - 1994, 1994 IEEE First World Conference on , Volume: 1 , 5-9 Dec. 1994, Pages:1077 - 1080 vol.1

[23] Doumbia, M.L.; Agbossou, K.; Bose, T.K.; "Islanding protection evaluation of inverter-based grid-connected hybrid renewable energy system", Electrical and Computer Engineering, 2004. Canadian Conference on, Volume: 2 , 2-5 May 2004, Pages:1081 - 1084 Vol.2

[24] Sung-Il Jang; Kwang-Ho Kim; "An islanding detection method for distributed generations using voltage unbalance and total harmonic distortion of current", Power Delivery, IEEE Transactions on , Volume: 19 , Issue: 2 , April 2004, Pages:745 – 752

[25] Sung-Il Jang; Kwang-Ho Kim; "Development of a logical rule-based islanding detection method for distributed resources", Power Engineering Society Winter Meeting, 2002. IEEE, Volume: 2, 27-31 Jan. 2002, Pages: 800 - 806 vol.2

[26] Tunlasakun, K.; Kirtikara, K.; Monyakul, V.; Thepa, S.; "A microcontroller based islanding detection for grid connected inverter", Circuits and Systems, 2004. MWSCAS'04. The 2004 47th Midwest Symposium on, Volume: 3, July 25-28, 2004, Pages: III_267 - III_269

[27] Liang, T.J.; Chen, J.F.; Mi, T.C.; Kuo, Y.C.; Cheng, C.A.; "Study and implementation of DSP-based photovoltaic energy conversion system", Power Electronics and Drive

Systems, 2001. Proceedings, 2001 4th IEEE International Conference on , Volume: 2 , 22-25 Oct. 2001, Pages:807 - 810 vol.2

[28] Mizuno, T.; Noda, Y.; Koizumi, H.; Nagasaka, K.; Kurokawa, K.; Kobayashi, H.; "The experimental results of an islanding detection method for Japanese AC modules", Photovoltaic Energy Conversion, 2003. Proceedings of 3rd World Conference on, Volume: 2, 12-16 May 2003, Pages: 2058 - 2061 Vol.2

[29] Imece, A.F.; Jones, R.A.; Sims, T.R.; Gross, C.A.; "An approach for modeling self-commutated static power converters for photovoltaic islanding studies", Energy Conversion, IEEE Transactions on , Volume: 4 , Issue: 3 , Sept. 1989, Pages:397 – 401

[30] Sigifredo Gonzalez, Russell Bonn, Jerry Ginn, Sandia National Laboratories, NM 87185-0753; "Removing barriers to utility interconnected photovoltaic inverters", 28th IEEE Photovoltaic Specialist Conference, Anchorage, AK, Sept 15-22, 2000.

[31] Martinez, A.I.; Calleja, H.; "A simple, high-quality output PV system aimed at peak demand reduction", Power Electronics Congress, 2000. CIEP 2000. VII IEEE International, 15-19 Oct. 2000, Pages: 301 – 306.

[32] Hudson, R.M.; Behnke, M.R.; West, R.; Gonzalez, S.; Ginn, J.; "Design considerations for three-phase grid connected photovoltaic inverters", Photovoltaic Specialists Conference, 2002. Conference Record of the Twenty-Ninth IEEE, 19-24 May 2002, Pages: 1396 – 1401

[33] Takigawa, K.; Kobayashi, H.; "A development of compact and reliable protective control unit for grid connected small residential PV systems", Photovoltaic Energy Conversion, 1994., Conference Record of the Twenty Fourth ; IEEE Photovoltaic

Specialists Conference - 1994, 1994 IEEE First World Conference on , Volume: 1 , 5-9 Dec. 1994, Pages:1081 - 1084 vol.1

[34] Sulaiman, T.A.; "Using the real-time island detection and network colouring application in electrical systems", Human Interfaces in Control Rooms, Cockpits and Command Centres, 2001. People in Control. The Second International Conference on (IEE Conf. Publ. No. 481), 19-21 June 2001, Pages: 234 - 239

[35] Ropp, M.E.; Aaker, K.; Haigh, J.; Sabbah, N.; "Using power line carrier communications to prevent islanding [of PV power systems]", Photovoltaic Specialists Conference, 2000. Conference Record of the Twenty-Eighth IEEE, 15-22 Sept. 2000 Pages: 1675 – 1678

[36] Woyte, A.; Belmans, R.; Nijs, J.; "Islanding of grid-connected AC module inverters", Photovoltaic Specialists Conference, 2000. Conference Record of the Twenty-Eighth IEEE, 15-22 Sept. 2000, Pages: 1683 – 1686

[37] Woyte, A.; Belmans, R.; Njis, J.; "Testing the islanding protection function of photovoltaic inverters", Power Engineering Society General Meeting, 2003, IEEE , Volume: 4 , 13-17 July 2003

APPENDIX

CALCULATION FOR THE PCC VOLTAGE UNDER ISLANDING CONDITION

The distorted current waveform is

$$i(t)=\begin{cases}\sin(2\pi f_i)t & 0\le t\le \dfrac{1}{f_i}\\ 0 & \dfrac{1}{f_i}\le t\le \dfrac{1}{f_v}\end{cases},\qquad i(t+T)=i(t), \tag{A-1}$$

where $f_i = f_v + \delta f, T=\dfrac{1}{f_v}, T_i=\dfrac{1}{f_i}$.

Current waveform also can be express as

$$\begin{aligned} i_1(t) &= \sin 2\pi f_i t - \sin 2\pi f_i (t-T_i)\cdot u(t-T_i)\\ i(t) &= i_1(t)+i_1(t-T)\cdot u(t-T)+i_1(t-2T)\cdot u(t-2T)+\cdots \end{aligned}. \tag{A-2}$$

Apply Laplace transform

$$\begin{aligned} I_1(s) &= \frac{\omega_i}{s^2+{\omega_i}^2}-e^{-T_i s}\cdot\frac{\omega_i}{s^2+{\omega_i}^2}=\left(1-e^{-T_i s}\right)\cdot\frac{\omega_i}{s^2+{\omega_i}^2}\\ I(s) &= I_1(s)+I_1(s)\cdot e^{-Ts}+I_1(s)\cdot e^{-2Ts}+\cdots = I_1(s)\cdot\sum_{n=0}^{\infty}e^{-nTs} \end{aligned}, \tag{A-3}$$

where $T_i=\dfrac{1}{f_i}$.

According to the series

$$\sum_{n=0}^{\infty}e^{-nTs}=\frac{1}{1-e^{-Ts}}\ . \tag{A-4}$$

So, one can get

$$I(s)=\frac{1}{1-e^{-Ts}}I_1(s)=\frac{1-e^{-T_i s}}{1-e^{-Ts}}\cdot\frac{\omega_i}{s^2+{\omega_i}^2}. \tag{A-5}$$

The parallel *RLC* load in frequency domain is

$$Z(s)=\frac{1}{sC+\frac{1}{R}+\frac{1}{sL}}=\frac{R\omega_0}{Q_f}\cdot\frac{s}{\left(s+\frac{\omega_0}{2Q_f}\right)^2+\left(\omega_0\sqrt{1-\frac{1}{4{Q_f}^2}}\right)^2}. \quad \text{(A-6)}$$

Thus, the voltage of the parallel *RLC* load is

$$V(s)=I(s)\cdot Z(s)=\frac{1-e^{-T_i s}}{1-e^{-Ts}}\cdot\frac{\omega_i}{s^2+{\omega_i}^2}\cdot\frac{R\omega_0}{Q_f}\cdot\frac{s}{\left(s+\frac{\omega_0}{2Q_f}\right)^2+\left(\omega_0\sqrt{1-\frac{1}{4{Q_f}^2}}\right)^2}. \quad \text{(A-7)}$$

Simplify the above equation by

1. $$\frac{1-e^{-T_i s}}{1-e^{-Ts}}=1-e^{-T_i s}+e^{-Ts}-e^{-(T_i+T)s}+e^{-2Ts}-e^{-(T_i+2T)s}+\cdots=\sum_{n=0}^{\infty}\left[e^{-nTs}-e^{-(nT+T_i)s}\right]. \quad \text{(A-8)}$$

2. Simplify the part

$$F(s)=\frac{s}{\left(s^2+{\omega_i}^2\right)\cdot\left[\left(s+\frac{\omega_0}{2Q_f}\right)^2+\left(\omega_0\sqrt{1-\frac{1}{4{Q_f}^2}}\right)^2\right]}. \quad \text{(A-9)}$$

Let

$$a=\omega_0\sqrt{1-\frac{1}{4{Q_f}^2}},\ b=\omega_i,\ c=\frac{\omega_0}{2Q_f}. \quad \text{(A-10)}$$

Then,

$$\begin{aligned}F(s)&=\frac{s}{\left[(s+c)^2+a^2\right]\cdot\left(s^2+b^2\right)}\\&=\frac{Es+F}{s^2+b^2}-\frac{A\cdot(s+c)+B}{(s+c)^2+a^2}\\&=\frac{(A-E)s^3+(2Ec+F-Ac-B)s^2+\left(Ec^2+Ea^2+2Fc-Ab^2\right)s+\left(Fa^2+Fc^2-Ab^2c-Bb^2\right)}{\left[(s+c)^2+a^2\right]\cdot\left(s^2+b^2\right)}\end{aligned} \quad \text{(A-11)}$$

One have

$$\begin{cases} A-E=0 \\ 2Ec+F-Ac-B=0 \\ Ec^2+Ea^2+2Fc-Ab^2=1 \\ Fa^2+Fc^2-Ab^2c-Bb^2=0 \end{cases} . \tag{A-12}$$

Solve it, one can get

$$\begin{cases} A=E=\dfrac{a^2+c^2-b^2}{\left(a^2+c^2-b^2\right)^2+4b^2c^2}=\dfrac{{\omega_0}^2-{\omega_i}^2}{\left({\omega_0}^2-{\omega_i}^2\right)^2+\dfrac{{\omega_0}^2{\omega_i}^2}{{Q_f}^2}} \\ B=\dfrac{\left(a^2+c^2+b^2\right)\cdot c}{\left(a^2+c^2-b^2\right)^2+4b^2c^2}=\dfrac{\left({\omega_0}^2+{\omega_i}^2\right)\cdot\dfrac{\omega_0}{2Q_f}}{\left({\omega_0}^2-{\omega_i}^2\right)^2+\dfrac{{\omega_0}^2{\omega_i}^2}{{Q_f}^2}} \\ F=\dfrac{2b^2c}{\left(a^2+c^2-b^2\right)^2+4b^2c^2}=\dfrac{{\omega_i}^2\cdot\dfrac{\omega_0}{Q_f}}{\left({\omega_0}^2-{\omega_i}^2\right)^2+\dfrac{{\omega_0}^2{\omega_i}^2}{{Q_f}^2}} \end{cases} . \tag{A-13}$$

Hence,

$$\begin{aligned} V(s)&=\frac{R\omega_0\omega_i}{Q_f}\cdot\sum_{n=0}^{\infty}\left[e^{-nTs}-e^{-(nT+T_i)s}\right]\cdot\left[\frac{Es+F}{s^2+b^2}-\frac{A\cdot(s+c)+B}{(s+c)^2+a^2}\right] \\ &=\frac{R\omega_0\omega_i}{Q_f}\cdot\sum_{n=0}^{\infty}\left[e^{-nTs}-e^{-(nT+T_i)s}\right]\cdot\left[\sqrt{E^2+\left(\frac{F}{b}\right)^2}\cdot\frac{(\sin\alpha)\cdot s+b\cos\alpha}{s^2+b^2}-\sqrt{A^2+\left(\frac{B}{a}\right)^2}\,\frac{(\sin\beta)\cdot(s+c)+a\cos\beta}{(s+c)^2+a^2}\right] \\ &=k_1\sum_{n=0}^{\infty}\left[e^{-nTs}-e^{-(nT+T_i)s}\right]\cdot\frac{(\sin\alpha)\cdot s+b\cos\alpha}{s^2+b^2}-k_2\sum_{n=0}^{\infty}\left[e^{-nTs}-e^{-(nT+T_i)s}\right]\cdot\frac{(\sin\beta)\cdot(s+c)+a\cos\beta}{(s+c)^2+a^2} \end{aligned} \tag{A-14}$$

where

$$\alpha = \tan^{-1}\left(\frac{E}{F/b}\right) = \tan^{-1}\left[Q_f \cdot \left(\frac{\omega_0}{\omega_i} - \frac{\omega_i}{\omega_0}\right)\right] = \phi_{load}(\omega_i)$$

$$\beta = \tan^{-1}\left(\frac{A}{B/a}\right) = \tan^{-1}\left[\sqrt{4Q_f{}^2 - 1} \cdot \frac{\omega_0{}^2 - \omega_i{}^2}{\omega_0{}^2 + \omega_i{}^2}\right]$$

$$k_1 = \frac{R\omega_0\omega_i}{Q_f} \cdot \sqrt{E^2 + \left(\frac{F}{b}\right)^2} = \frac{R}{\sqrt{1 + Q_f{}^2 \cdot \left(\frac{\omega_0}{\omega_i} - \frac{\omega_i}{\omega_0}\right)^2}} = \left|Z_{load}(\omega_i)\right| \quad . \quad \text{(A-14)}$$

$$k_2 = \frac{R\omega_0\omega_i}{Q_f} \cdot \sqrt{A^2 + \left(\frac{B}{a}\right)^2} = R \cdot \frac{\sqrt{Q_f{}^2 \cdot \left(\frac{\omega_0}{\omega_i} - \frac{\omega_i}{\omega_0}\right)^2 + \frac{Q_f{}^2}{4Q_f{}^2 - 1} \cdot \left(\frac{\omega_0}{\omega_i} + \frac{\omega_i}{\omega_0}\right)^2}}{1 + Q_f{}^2 \cdot \left(\frac{\omega_0}{\omega_i} - \frac{\omega_i}{\omega_0}\right)^2}$$

Apply inverse Laplace transform

$$v(t) = k_1 \sum_{n=0}^{\infty} \{\sin[b(t-nT)+\alpha] \cdot u(t-nT) - \sin[b(t-nT-T_i)+\alpha] \cdot u(t-nT-T_i)\}$$
$$- k_2 \sum_{n=0}^{\infty} \{e^{-(t-nT)\cdot c} \sin[a(t-nT)+\beta] \cdot u(t-nT) - e^{-(t-nT-T_i)\cdot c} \sin[a(t-nT-T_i)+\beta] \cdot u(t-nT-T_i)\}$$

(A-15)